ISSN: 0379 - 4318

JOURNAL OF MECHANICAL ENGINEERING

Transaction of The Mechanical Engineering Division
The Institution of Engineers, Bangladesh

Volume: ME 49, No. 2, June 2019

AERODYNAMIC BEHAVIOR OF LOW REYNOLDS NUMBER AIRFOIL UNDER FLUCTUATING FREE STREAM CONDITION

A K M Zahidur Rahman, Sourov Kumar Mondal, A.B.M. Toufique Hasan*
Department of Mechanical Engineering, Bangladesh University of Engineering and Technology (BUET), Dhaka-1000, Bangladesh
*Corresponding e-mail: toufiquehasan@me.buet.ac.bd

Abstract: *A numerical computation is carried out to investigate the effect of fluctuating free stream condition on the flow and resultant aerodynamic characteristics of low Reynolds number airfoil Eppler 61. The amplitude of fluctuation is kept 10% of steady inflow velocity magnitude while the fluctuation frequency has been varied from 83.3 Hz to 333.2 Hz. The results obtained from present unsteady computation have been compared and validated with the available experimental data for steady inflow condition. In case of fluctuating inflow condition, the aerodynamic behavior has been changed compared to steady uniform inflow condition. The time history of lift and drag characteristics showed a significant fluctuation with spikes in force magnitudes. Moreover, the intensity of spikes increases considerably with the increment of inflow fluctuation frequency which is expected to result severe vertical and longitudinal vibrations of airfoil.*

Keywords*: low Reynolds number flow, airfoil, lift and drag, numerical computation*

1. INTRODUCTION

Development of micro air vehicles (MAVs) is of current interest for special purpose limited- duration military and civil missions that include surveillance, detection, communications, and so on [1-3]. MAVs are aircrafts which have typical length dimension of 15-cm and the operating speed around 10 m/s [3]. These geometry and flow combinations of MAV result a flight regime with low Reynolds number in the order of 10^4 [1-3]. At this flow condition, the boundary layer is very weak and much sensitive to adverse pressure gradient. In MAVs, laminar separation bubbles formed (when the boundary layer separates), transitions and reattaches along the airfoil surface and generate unsteady flow field [4]. Over the years, thin airfoils are designed and proposed for possible application in MAVs; for example Eppler 61, Eppler 423, Ishii airfoil, SD7003 etc. [4-6].

MAVs are designed to carry out specific tasks for which it should cover wide range of operational area including mountains, desert, jungle/trees, urban etc. MAV has to encounter gusty wind (fluctuating free stream condition) while operating in above mentioned areas. Moreover, even a calm wind can also create a gusty wind field in an urban environment. Thus, MAVs need to perform their missions in adverse weather conditions; for example- precipitation, wind gusts, wind shear etc. Accordingly, Lian and Shyy [7] numerically studied the effect of gust on transition process and airfoil performance by using SD7003 airfoil. It is found found that the transition point moves toward the leading edge when flow accelerate and moves toward the trailing edge when the flow decelerates. Moreover, transition occurs earlier during accelerating stage, as the instantaneous Reynolds number increases. Further, it is reported that aerodynamic coefficients display the hysteresis phenomena i.e. when the flow accelerates, the lift coefficient does not immediately reach its corresponding steady-state value. A large variation is also found in lift-to-drag ratio during one cycle compared to steady free stream condition. Prater and Lian [8] studied the flight characteristics of stationary and flapping wings in low Reynolds number flows under gusty environment. A sinusoidal velocity component is used as gust model. It is observed that in comparison to a stationary wing, the flapping wing can significantly alleviate the lift variation generated due to wind gust. Moreover, under same gust conditions, the flapping wing generates higher lift than the stationary wing. Granlund et al. [9] carried out wind tunnel experiment on NACA0009 airfoil with periodic sinusoidal longitudinal gust of oscillating flow at *Re* = 57,000. Results showed that the lift and drag are independent on dimensionless frequency up to the incidence angle of θ =10°. For θ > 10°, both lift and drag exhibit a strong dependency on dimensionless frequency. With the increment of incidence angle to 10º; fluctuating lift coefficient amplitude and phase appears in a deviation from the classical theory and static stall also pass through. Also the flow became fully separated at 20° angle of incidence and dimensionless frequency of 0.7; the measured lift fluctuation amplitudes were almost three times larger than those predicted by classical theory. Yang et al. [10] investigated the unsteady lift of a stationary NACA0015 airfoil with a sinusoidal stream wise wind gust. It is found that the fluctuation in the lift force reduces at the higher dimensionless frequency which attributed significant reduction in the fluctuating pressure difference between the upper side and the lower side over the front half of the airfoil.

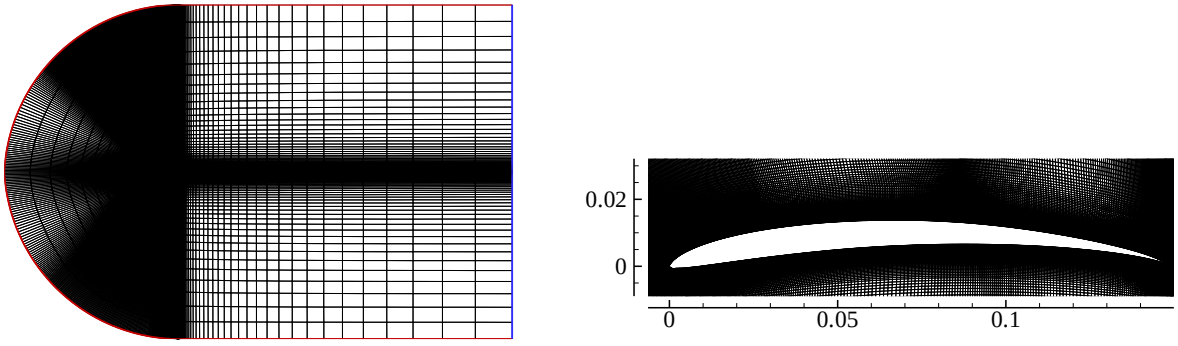

(a) (b)

Figure 1: (a) Computational domain with grids; (b) Closed-up view of grids around Eppler 61 Airfoil

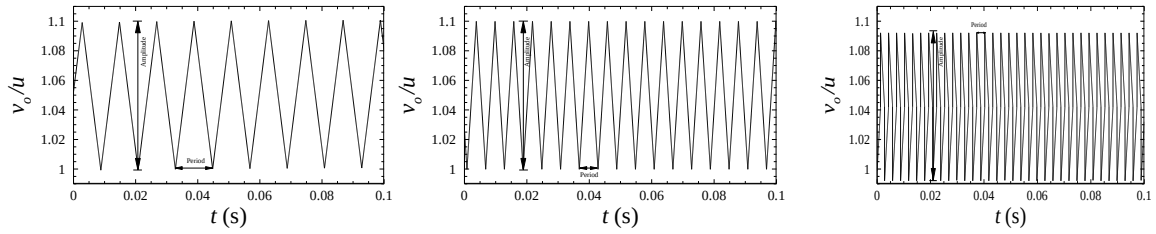

(a) f_{ex} = 83.3 Hz (b) f_{ex} = 166.6 Hz (c) f_{ex} = 333.2 Hz

Figure 2: Profiles of fluctuating free stream

The impact of a wind gust on the cycle averaged lift force and the lift variation over a gust cycle are examined by other researchers [11-13]. Recently, Barnes and Visbal [14] computationally studied the interactions between a NACA0012 airfoil and a vortical gust at transitional Reynolds number of 2×10^5.

The interaction of fluctuating free stream with the flow field around an airfoil is very complex. However, the effects of gust amplitude and frequency on the aerodynamic characteristics of low Reynolds number airfoil are not clearly understood until now. The present study investigates the aerodynamic characteristics of Eppler 61 airfoil under fluctuating inflow conditions at low Reynolds number flow. The frequency of fluctuating will be varied for better understanding of the gust effect on unsteady aerodynamics of Eppler 61 airfoil.

2. NUMERICAL MODELLING

The flow in this study is considered to be unsteady, viscous, incompressible, and laminar. Governing equations for the present computations are the conservation of mass, and conservation of momentum. The governing equations are discretized spatially using a Finite volume method of second order scheme. For the time derivatives, an implicit multistage time stepping scheme, which is advanced from time t to time $t+\Delta t$ with a second order Euler backward scheme for physical time and implicit pseudo-time marching scheme for inner iteration, is used. A time step size of 10^{-5} was sufficient for this type of unsteady computation.

The computational domain together with the grids is shown in Fig. 1(a). The chord length c of Eppler 61 low Reynolds number airfoil is considered to be 150 mm. The upstream and downstream boundaries are located at 20c and 100c, from the leading edge of the airfoil. On the other hand, the top and bottom boundaries are 25c apart from the airfoil surfaces. This spacing was considered to be sufficient to apply free-stream conditions on the outer boundaries. The adiabatic no-slip conditions are applied to airfoil surfaces. The Reynolds number based on the airfoil chord length, $Re = 4.6\times10^4$.

A structured clustered grid system using quadrilateral cells was employed in the computations. The total number of grids is 165,000 which give a grid independent solution. For viscous flow calculation, extra fine spaced grids were constructed over the airfoil surfaces as shown in Fig. 1(b). A solution convergence was obtained when the residuals for each of the conserved variables were reduced below the order of magnitude 5.

3. FLUCTUATING FREE STREAM INFLOW

To mimic the gust condition, present study considers a fluctuating inflow conditions with triangular profile. The inflow first increases from 4.5 m/s ($Re = 4.6\times10^4$) to 4.95 m/s ($Re = 5.06\times10^4$) linearly and then decreases to 4.5 m/s ($Re = 4.6\times10^4$) as shown in Fig. 2. The times for increasing state and

decreasing state are considered to be same. However, three different external frequency has been considered; namely- 83.3 Hz, 166.6 Hz, and 333.2 Hz, respectively which are half, equal and twice the base frequency of oscillation in case of steady inflow condition at 0° angle of attack (will be discussed later).

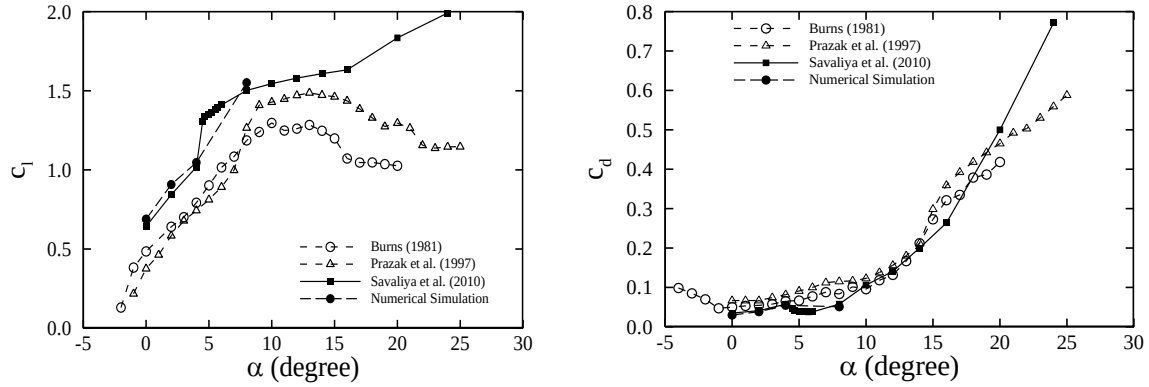

(a) (b)

Figure 3: Time-averaged aerodynamic coefficients at different angles of attack

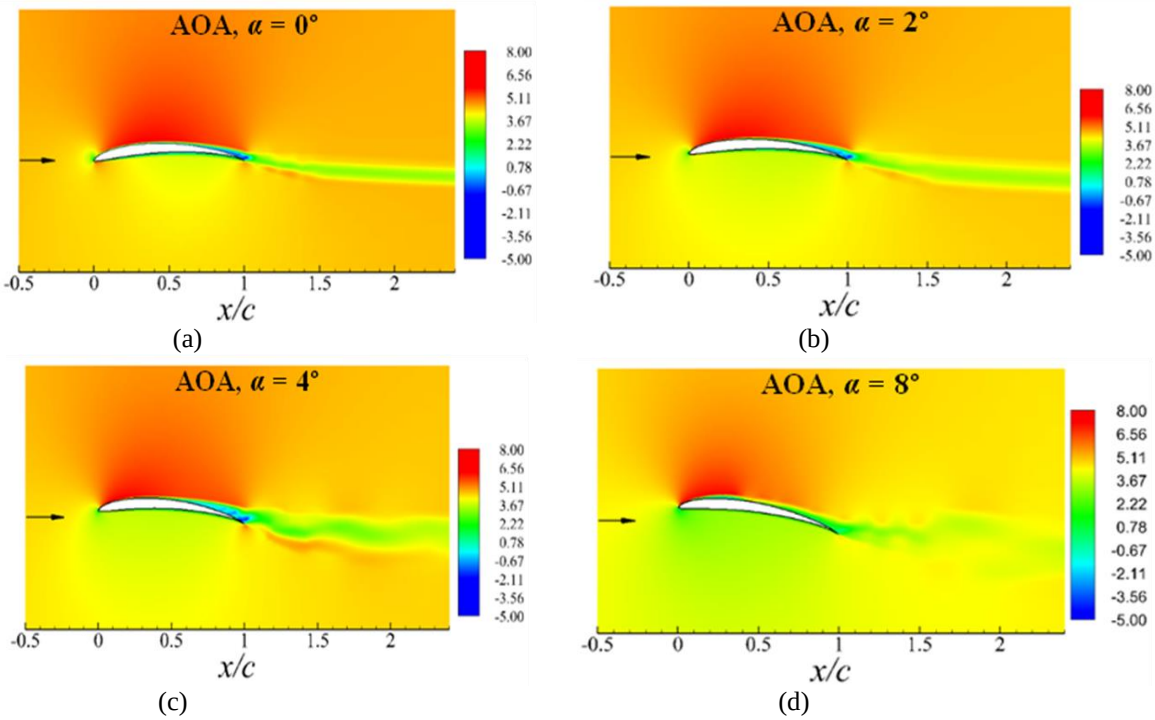

(a) (b)

(c) (d)

Figure 4: Time-averaged *x*-velocity contour at steady inflow condition

4. COMPUTATIONAL VALIDATION

Before going to the detail discussion of the present problem, the computational results have been validated with the available experimental and numerical data. Fig. 3(a) and 3(b) shows the lift coefficient and drag coefficient, respectively. It is found that the general trend of change of lift and drag coefficients are in good agreement with the experimental results. However, 5% to 7% variation is observed in present numerical results. There are several factors that may cause the deviation. One possible reason is the viscous effect due to the side walls that are likely to be encountered in a 3D real flow phenomenon, but it was not considered in this two-dimensional study.

5. RESULTS AND DISCUSSION

The flow field around Eppler 61 airfoil is inherently unsteady even at steady inflow condition of 4.5 m/s (Re = 4.6×10^4). The time-averaged *x*-velocity contours are shown in Fig. 4. At angle of attack, α = 0° (Fig. 4(a)), the velocity around the upper surface is higher than that of lower surface. In this case, the flow is rarely separated from the upper surface. The vortex street downstream of the airfoil trailing edge is uniform and diffused in the far

downstream flow field. At α = 2° (Fig. 4(b)), the flow is almost similar to that of the α = 0°. However, the width of the vortex is increased and slightly separated from the mid chord of the airfoil upper surface which results a well defined vortex shedding downstream of the flow field. However, the flow stats to separated from the airfoil leading edge for α = 8° (Fig. 4(d)). Now, the vortex is seen to propagate from the airfoil upper surface. As a result, asymmetric vortex pattern is found.

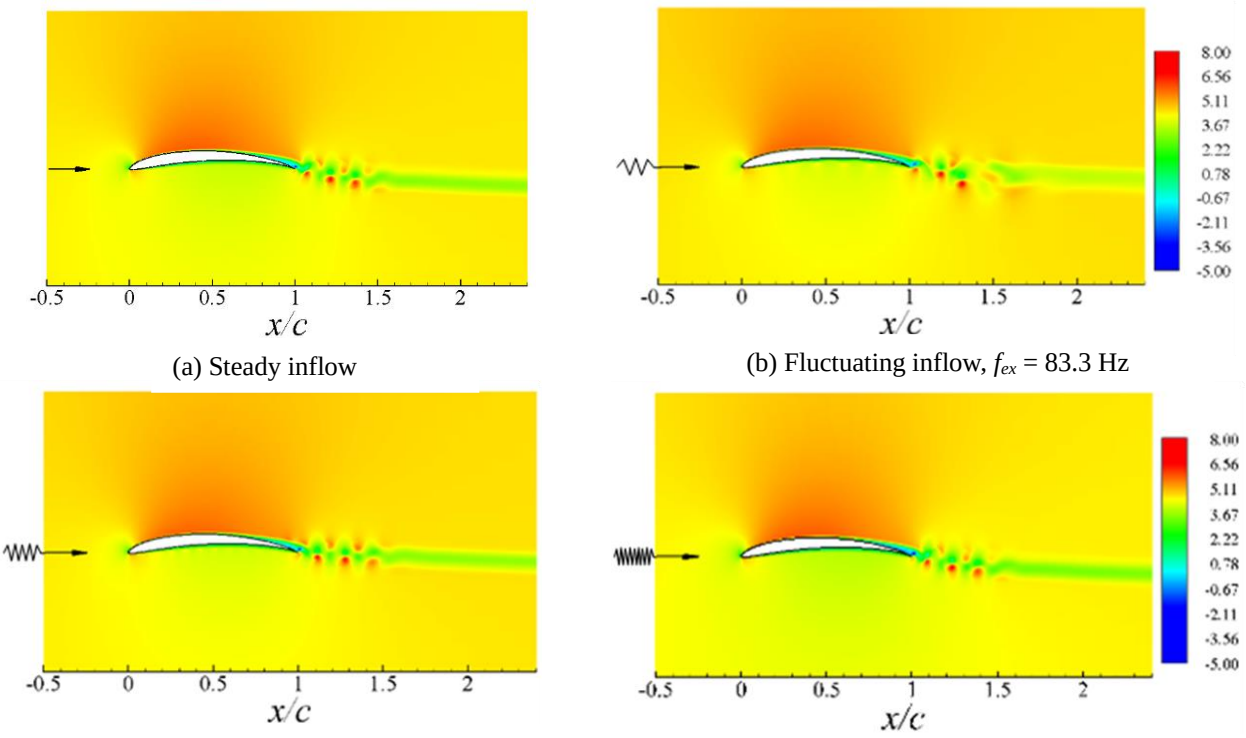

(a) Steady inflow

(b) Fluctuating inflow, f_{ex} = 83.3 Hz

(c) Fluctuating inflow, f_{ex} = 166.6 Hz

(d) Fluctuating inflow, f_{ex} = 333.2 Hz

Figure 5: Instantaneous *x*-velocity contour (α = 0°)

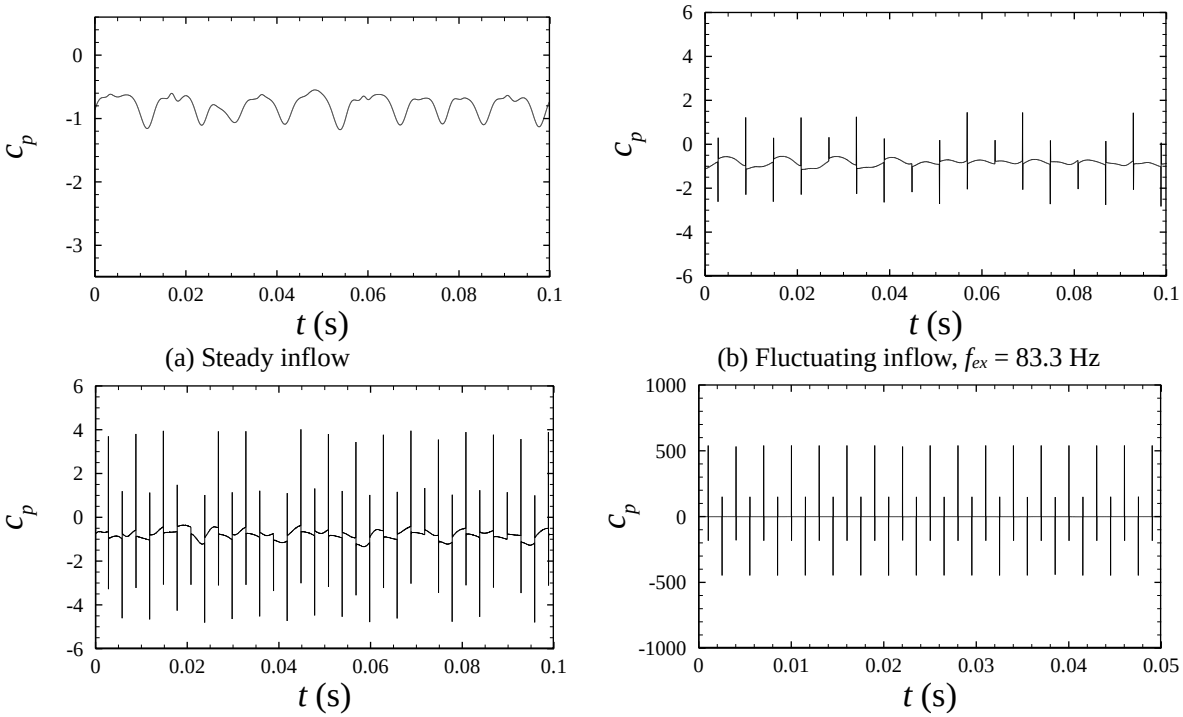

(a) Steady inflow

(b) Fluctuating inflow, f_{ex} = 83.3 Hz

(c) Fluctuating inflow, f_{ex} = 166.6 Hz

(d) Fluctuating inflow, f_{ex} = 333.2 Hz

Figure 6: Pressure-time history at x/c = 0.98 (α = 0°)

Fig. 5 shows the instantaneous *x*-velocity contour at t/T = 7/8 for different inflow conditions for zero angle of attack. At this condition, the flow downstream of the trailing edge is affected by the fluctuating inflow condition. The width of vortex shed is slightly increases with increase of fluctuation frequency, f_{ex} in comparison of steady inflow condition. However, the flow pattern is remained undisturbed around the airfoil upper surface.

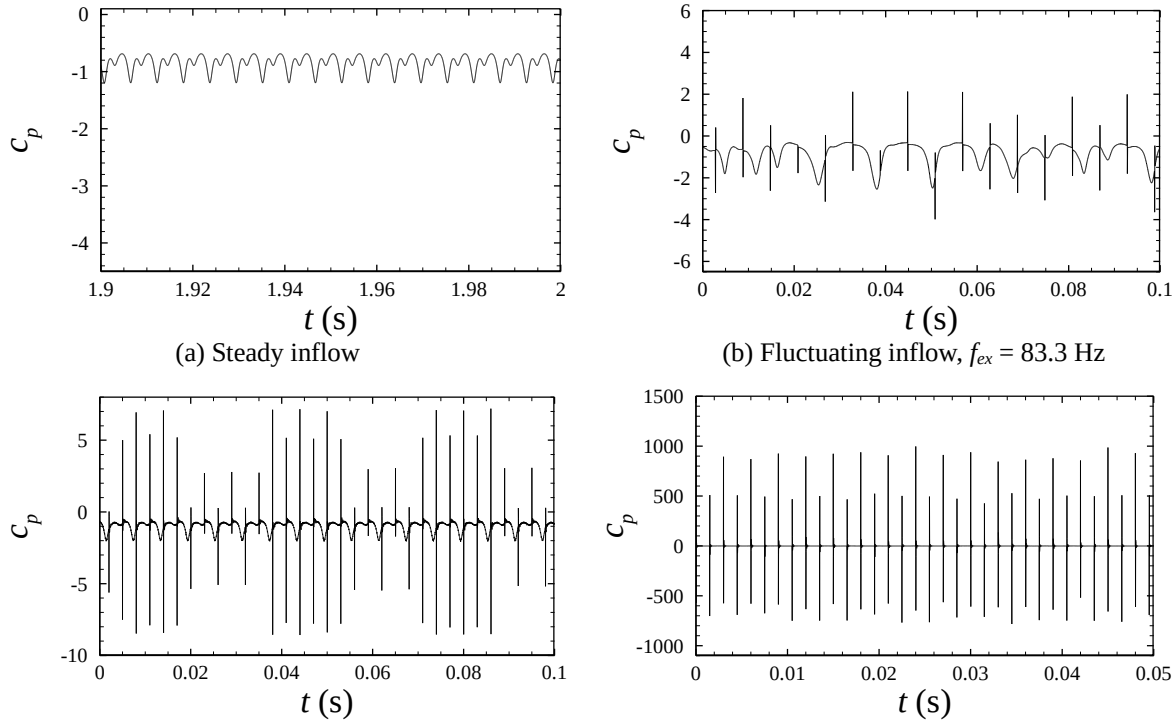

(a) Steady inflow (b) Fluctuating inflow, f_{ex} = 83.3 Hz

(c) Fluctuating inflow, f_{ex} = 166.6 Hz (d) Fluctuating inflow, f_{ex} = 333.2 Hz

Figure 7: Wake pressure-time history at x/c = 1.10 (α = 0°)

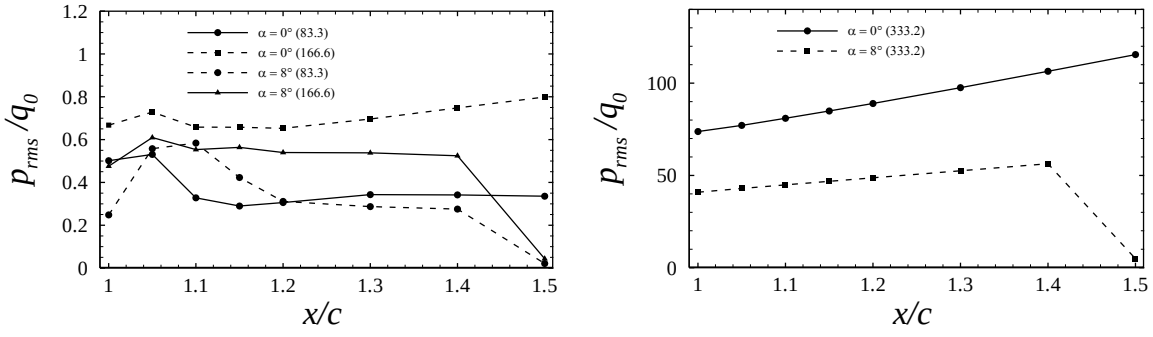

(a) (b)

Figure 8: Wake pressure-time history at x/c = 1.10 (α = 0°)

Time histories of static pressure at x/c = 0.98 (airfoil upper surface) are presented in Fig. 6. At steady uniform inflow condition, the pressure is fluctuated almost in sinusoidal pattern (Fig. 6(a)). The averaged value of c_p is around − 0.9. With the fluctuating inflow condition, the pattern of c_p fluctuation is changed. There are sharp spikes in the c_p distribution over the time at all the fluctuation conditions. The averaged values of c_p have been changed with imposed flow oscillation at upstream. Thus, the pressure field is affected around the airfoil surface when the upstream flow is unsteady.

Fig. 7 shows the wake pressure history at different inflow conditions. The wake behavior corresponds to the change as found in Fig. 6. With the increment of external frequency, f_{ex} the magnitude of spike is increased.

The flow field aerodynamic instability at wake region can be expressed by the distribution of root means square (RMS) value of pressure and the results are shown in Fig. 8. The value of p_{rms} at angle of attack, α = 0° is always more than that of α = 8°. Moreover, the value of p_{rms} is higher at 166.6 Hz than that of 83.3 Hz (Fig. 8(a)). On the other hand, the value of p_{rms} at f_{ex} = 333.2 Hz is much higher than

that of other two frequencies of 166.6 Hz and 83.3 Hz (Fig. 8(b)).

The aerodynamic characteristics of Eppler 61 are now presented in terms of lift and drag characteristics. As discussed earlier, the flow field is inherently unsteady which results a lift and drag fluctuations at steady inflow condition as shown in Fig. 9(a). FFT analysis shows that the frequency is 166.6 Hz which is taken as base frequency.

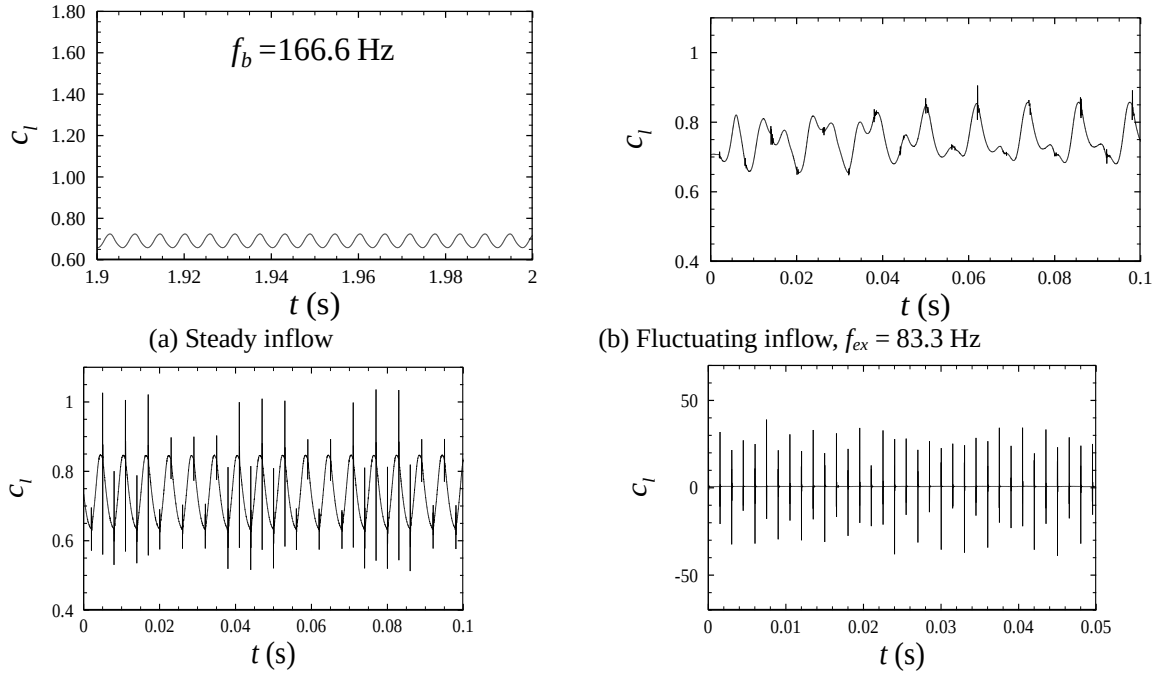

(a) Steady inflow (b) Fluctuating inflow, f_{ex} = 83.3 Hz

(c) Fluctuating inflow, f_{ex} = 166.6 Hz (d) Fluctuating inflow, f_{ex} = 333.2 Hz

Figure 9: Wake pressure-time history at x/c = 1.10 (α = 0°)

Table 1: Time-averaged lift and drag coefficients at different flow conditions

Angle of Attack	Flow Condition	C_l			C_d		
0°	Steady inflow	0.6890			0.0298		
	With gust	$0.5f_b$	f_b	$2f_b$	$0.5f_b$	f_b	$2f_b$
		0.7478	0.7357	0.7544	0.0344	0.0336	0.0338
8°	Steady inflow	1.5511			0.0509		
	With gust	$0.5f_b$	f_b	$2f_b$	$0.5f_b$	f_b	$2f_b$
		1.6065	1.6721	1.6705	0.0462	0.0447	0.0652

Fluctuating inflow condition (gust) results different pattern of lift fluctuations as found in Figs. 9(a), 9(b) and 9(c). At imposed external frequency of 166.6 Hz (which is equal to base frequency), there are spikes in lift evolution. The spikes are became very significant at frequency of 333.2 Hz which is twice the base frequency. Drag behavior is similar to lift characteristics and are not shown here for brevity.

Finally, the time-averaged lift and drag magnitudes are presented in Table 1 for α = 0° and 8°. It is found that the lift is increased with fluctuating free stream condition. 10% rise in lift is observed for α = 0° while 7% increment is found for α = 8°. However, the rise in lift comes with the expenses of drag rise. Depending on the magnitude of fluctuation, drag rises by 13% α = 0° while it is 28% in case of α = 8°. Thus, at high angle of attack, the aerodynamic characteristics are significantly deteriorate with fluctuating free stream condition.

6. CONCLUSIONS

A two-dimensional unsteady numerical computation has been performed to investigate the aerodynamic characteristics of low Reynolds number airfoil Eppler 61 at Re = 4.6×10^4 under fluctuating free stream condition. The fluctuation amplitude is kept 10% while the frequency of fluctuation is varied from 83.3 Hz to 333.2 Hz. The airfoil is kept at 0°

and 8° angle of attack. The results obtained from present research have been validated with the available experimental results in case of steady inflow condition. A good agreement in aerodynamic coefficient was found.

The results obtained from the present numerical computations can be summarized as follows:

- Airfoil aerodynamic characteristics have been changed with the presence of fluctuating free stream condition.
- In fluctuating condition, the value of C_l is increased than that of 'no fluctuation' condition at all angles of attack studies in the present study.
- The magnitude of C_d is found to be increased than that of 'no fluctuation' condition except for two frequencies of 83.3 Hz and 166.6 Hz at 8° angle of attack.
- The increment of C_d with angle of attack is observed to be increased in fluctuating condition.
- The fluctuating lift and drag characteristics are found to be non-uniform and irregular at higher frequencies.

7. REFERENCES

[1] Gad-el-Hak, M., 2001, Micro-Air-Vehicles: Can They be Controlled Better?, *Journal of Aircraft*, 38, pp. 419-429.

[2] Grasmeyer, J. M. and Keennon, M. T., 2001, Development of the Black Widow Micro Air Vehicle, AIAA Paper No. 2001-0127.

[3] Ifju, P.G, Jenkins, A.D., Ettingers, S., Lian, Y. and Shyy, W., 2002, Flexible-Wing-Based Micro Air Vehicles, AIAA Paper 2002-0705.

[4] Anyoji, M., Nonomura, T., Aono, H., Oyama, A., Fujii, K., Nagai, H. and Asai, K., 2014, Computational and Experimental Analysis of a High-Performance Airfoil Under Low-Reynolds-Number Flow Condition, *Journal of Aircraft*, 51(6), pp. 1864-1872.

[5] Elimelech, Y., Arieli, R. and Iosilevskii, G., 2007, Flow over NACA-0009 and Eppler-61 Airfoils at Reynolds Numbers 5000 to 60,000, *AIAA Journal*, 45(10), pp. 2414-2421.

[6] Muller, T.J. and Burns, T.F., 1982, Experimental Studies of the Eppler 61 Airfoil at Low Reynolds Numbers, AIAA Paper No 82-0345.

[7] Lian Y. and Shyy W., 2007, Laminar-Turbulent Transition of a Low Reynolds Number Rigid or Flexible Airfoil, *AIAA Journal*, 45(7), pp. 1501-1513.

[8] Prater, R. and Lian, Y., 2012, Aerodynamic Response of Stationary and Flapping wings in Oscillatory Low Reynolds Number Flows, AIAA Paper No. 2012-0418.

[9] Granlund, K., Monnier, B., and Williams, D., 2014, Airfoil longitudinal gust response in separated vs. attached flows, *Physics of Fluids*, 26 (2), pp. 027103.

[10] Yang, Y., Li, M., Ma, C. and Li, S., 2017, Experimental investigation on the unsteady lift of an airfoil in a sinusoidal stream wise gust, *Physics of Fluids*, 29, pp. 051703.

[11] Jones, M. and Yamaleev, N. K., 2016, Effect of lateral, downward, and frontal gusts on flapping wing performance, *Journal of Computers and Fluids* 140, pp. 175-190..

[12] Biler, H., Badrya, C. and Anya R. Jones, A. R., 2018, Experimental and computational investigation of transverse gust encounters, AIAA paper No. 2018-0571.

[13] Savaliya, S. B., Kumar, S. P., and Mittal, S., 2010, Laminar Separation Bubble on an Eppler 61 Airfoil, *International Journal for Numerical Methods in Fluids*, 64 (6), pp. 627–652.

[14] Barnes, C. J. and Visbal, M. R., 2018, Clockwise Vortical-Gust/Airfoil Interactions at a Transitional Reynolds Number, *AIAA Journal*, 56(10), pp. 3863-3874.

NUMERICAL OBSERVATION OF HEAT TRANSFER AND PRESSURE BEHAVIOUR IN AN AUTOMOBILE RADIATOR

Sobahan Mia*, Shahadat Hossen
Department of Mechanical Engineering, Khulna University of Engineering & Technology, Khulna
*Corresponding Author email: smia@me.kuet.ac.bd

Abstract: *A radiator is a device which transfers heat from a hot medium of fluid to a cold medium of air through a separator. Many researches had done to make the radiator simpler and more efficient. In this paper there is a CFD analysis of a radiator tube with fin. ANSYS FLUENT 16.0 was used for this analysis. Computational Fluid Dynamics (CFD) is used to analyze the flow characteristics in radiator tube. Here ANSYS Meshing is used to generate the grid for analysis. ANSYS Fluent is used for the CFD analysis purpose. Comparison of pressure drop and temperature difference between inlet and outlet are presented for various mass flow rate. In this analysis various temperature, velocity contour is compared for different Reynold numbers where volume fraction of nano particle is fixed and for different volume fraction of nano particle where Reynold number is fixed. The results show that Reynold number and volume fraction exert great effect on the pressure drop, temperature different from inlet to outlet and distribution of pressure and temperature along the tube. The result also shows that temperature difference from inlet to outlet is increase with higher Reynold number and volume fraction.*

Keywords: *Convection, Radiator tube, Nanofluid, Volume fraction.*

1. INTRODUCTION

A radiator is a type of heat exchanger. Radiator are used to exchange heat from the hot coolant to air that flows around the tube and fin blown through air by the fan. The radiators are mainly used aluminum radiators. Some radiators are used brazing thin aluminum fins that are flattened with aluminum tubes. When engine is in operation automotive engine cooling system takes care of excess heat produced. It maintains engine surface temperature at safe zone for engine optimum efficiency. Main parts of an automotive engine cooling systems are the water pump, the radiator, thermostat and cooling fan pressure cap. Main component of the engine cooling system is Radiator. Through the many tubes of radiator mounted in a parallel arrangement coolant flows from inlet to the outlet. The heat conduct from the fins to the tubes and transfer to the air flowing around the radiator. The heat transferred from fluid to tube depends on the difference in temperature between the tube and the fluid passes tube. The fluid which is contact with the tube and cools down quickly, less heat will be transferred. Radiators mainly consist by two tanks on each side [1].

Nanofluids are defined as the new developed thermal fluids with the enhanced thermophysical properties and which can improve the heat transfer performance of the various applications. When introduce nanoparticles with the high thermal conductivity in the car radiator coolant can enhance the thermal conductivity of coolant and which improves the performance of the cooling system. Alumina (Al_2O_3), silica (SO_2) and copper oxide (CuO) nanoparticles mixture with base fluid water and use in 3-dimentional car radiator simulations to study fluid flow patterns and heat transfer performance. Heat transfer performance for water mixture based nanofluids at different nanoparticle concentrations has been studied. Overall heat transfer performance is found to be improved using nanofluids with high effective thermal conductivity. Results display significant increase in heat transfer performance of coolant in car radiator with an increase in the particle loading [2]. The objectives of this study are –to investigate the fluid flow and heat transfer characteristics of nanofluid flow in a radiator tube for different volume fraction, to investigate the fluid flow and heat transfer characteristics of nanofluid flow in a radiator tube for different Reynolds number (Re), to observe pressure drop through radiator tube.

2. METHODOLOGY

The study has done by CFD analysis of a radiator tube with fin using ANSYS Fluent. The form of continuity equation or the conservation of mass equation, the momentum equation in tensor

notation for a Newtonian fluid has been considered.

The law of conservation of energy states that the total energy of an isolated system remains constant.

$$h = h_m + h_T + h_c + \varphi \quad \ldots\ldots\ldots (1)$$

where,

$h_m = \frac{1}{2}\rho U_i U_i$: Kinetic energy

$h_T = \sum_n m_n \int_{T_{ref}}^{T} C_{p,n}\, dT$: Thermal energy

$h_c = \sum_n m_n h_n$: Chemical energy

$\varphi = g_i x_i$: Potential energy

Calculated the effective properties of the nanofluid density (ρ_{nf}) and special heat capacity (c_p, nf) of CuO-water nanofluid proposed by Mahendra Godley, Bhanu Pratap Singh Tomar, Ajay Tripathi [3] as follows:

$$\rho_{nf} = (1-\emptyset)\rho_{bf} + \emptyset\rho_p \quad \ldots\ldots\ldots (2)$$

$$C_{p,nf} = \frac{(1-\emptyset)\rho_{bf}C_{p,bf} + \emptyset\rho_p C_{p,p}}{\rho_{nf}} \quad \ldots\ldots\ldots (3)$$

Where, $\emptyset$ is nanoparticle volume concentration and P_p ρ_{bf} and $C_{p,p}$ and $C_{p,p}$, $C_{p,bf}$ are the densities and the specific heats of the nanoparticles and base fluid, respectively.

Also, thermal conductivity (K_{nf}) and viscosity(μ_{nf}) for nanofluid have been estimated based on two semi-empirical equations presented by Mahendra Godley, Bhanu Pratap Singh Tomar, Ajay Tripathi [3] as following equations

$$K_{nf} = \frac{K_p + (n-1)K_{bf} - \varphi(n-1)(K_{bf} - K_p)}{K_p + (n-1)K_{bf} - \varphi(n-1)(K_{bf} - K_p)} \times K_{bf}$$

$$\mu_{nf} = \mu_{bf}\frac{1}{(1-\varphi)^2}$$

For the simulation carry out need to made some following assumptions:

(i) The coolant flow rate is Constant and fluid temperatures are also constant at both the inlet and outlet, i.e. the steady state condition.

(ii) Heat loss by coolant was only transferred to the cooling air, thus no other heat transfer mode such as radiation was considered.

(iii) Coolant flow are in a fully developed condition in the tube.

(iv) All dimensions were uniform throughout the radiator and the heat transfer of surface area was consistent and distributed uniformly.

(v) The thermal conductivity of the material are considered to be constant.

(vi) There are no heat sources and sinks in the radiator.

Numerical simulations were performed in a laminar flow. Hybrid nanofluids based on water with volume concentrations of 1%, 2%, 3%, 4%, 5% for CuO nanoparticles size 20 nm.

Table 1: Thermo-physical properties of base fluid and Nano-particles [4]

Property	water	Cu	Al_2O_3	CuO
$\rho(kg/m^3)$	997.1	8933	3970	6500
$c_p(J/KgK)$	4179	385	765	535.6
$k(W/mK)$	0.613	400	40	20
$\alpha \times 10^7(m^2/s)$	1.47	1163.1	57.45	131.7
$\beta(K^{-1})$	0.00021	0.000051	0.000051	0.000024

3. CFD ANALYSIS

Geometrical modelling

The dimensions of the geometry are followed below in the table 2.0.

Table 2: Specifications of Honda Civic Radiator

No.	Part Dimension	Unit value
1	Pipe Diameter Inlet/Outlet	26 mm
2	Radiator core height	320 mm
3	Radiator core length	350 mm
4	Diameter of cooling pipe	2 mm
5	Thickness of fin	0.8 mm
6	Width of fin	20 mm
7	Number of fin in a single column	180
8	Number of fin columns	34
9	Total number of fins	6120
10	Total number of cooling pipes	33
11	Distance between two pipes	7.5 mm
12	Distance between two fins	1.9 mm

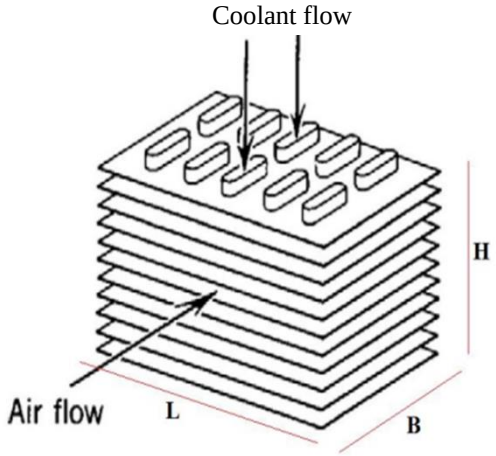

Figure 1: Typical configuration of an automobile radiator

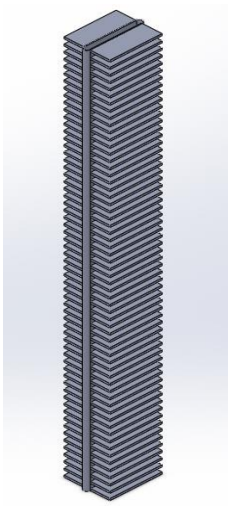

Figure 2: Element considered for analysis

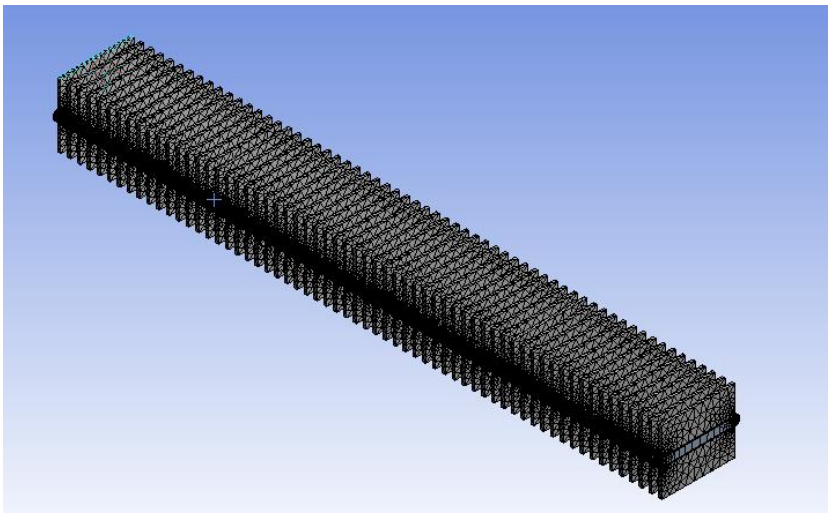

Figure 3: Meshing of Radiator tube with fins

4. MESHING AND BOUNDARY CONDITION

For the Radiator tube with fins, a mesh had been generated with 1326185 nodes and 3373661 elements. This mesh was generated up with face sizing, edge sizing and body sizing. Meshing of the radiator tube with fin is shown in Fig. 3.
In this simulation, the boundary conditions are:
- Inlet: mass flow rate and temperature, T=368 K;
- Outlet: pressure outlet P=0;
- Wall: heat transfer coefficient h=258.85W/m^{2}K and ambient temperature T=303.6 K, non-slip condition.

5. RESULT & DISCUSSION

Mesh dependency for the CFD analysis was done by changing the mesh setup. The mass flow rate are 0.0015 Kg/s

Table 3: result of mesh independence test

Mesh	Number of Nodes	Outlet temperature deviation (%)
Mesh1	977997	-------
Mesh2	1030896	1.34
Mesh3	1326185	0.216
Mesh4	1422088	0.001534

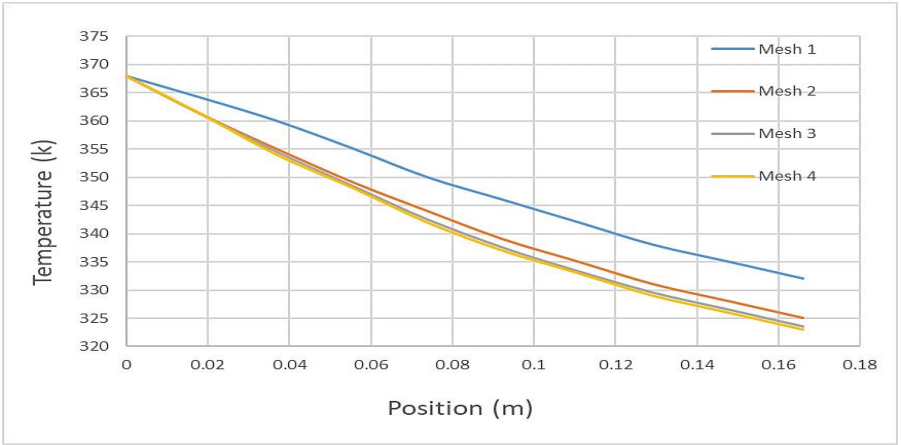

Figure 4: Temperature vs. Position for different mesh

The obtained results from the simulation has been compared with K. B. Sharif at el. [5]. Comparison is shown in table 4. Fig. 5 shows the temperature profile along the tube length. Temperature decreases as passing through the tubes of the radiator. While Fig. 6 shows the pressure profile along the tube length, pressure drop as passing through the tubes of the radiator.

Table 4: Temperature deviation while comparing paper [5] and numerical analysis

T_{in} (°K)	T_{atm} (°K)	h $(W/m^2\,K)$	T_{out} (Paper) (°K)	T_{out} (Numerical analysis) (°K)	Deviation (%)
368	303.6	258.85	320.6	321.57	0.3
368	307.6	275.99	322.6	323.37	0.23
368	310.2	288.41	324.05	325.14	0.34
368	311.6	295.57	324.66	325.46	0.25

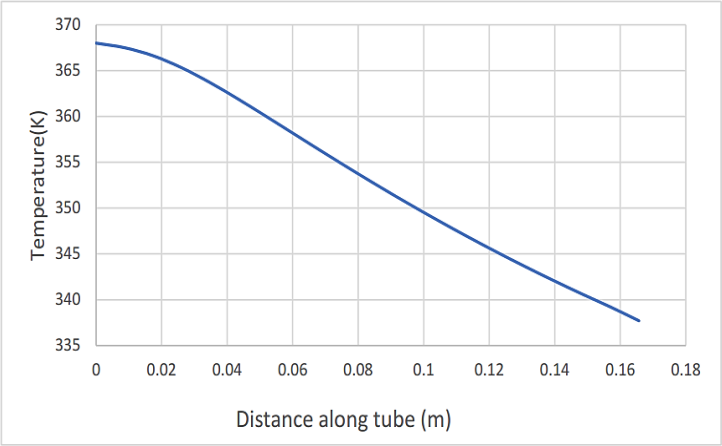

Figure 5: Temperature profile of water side along the tube length.

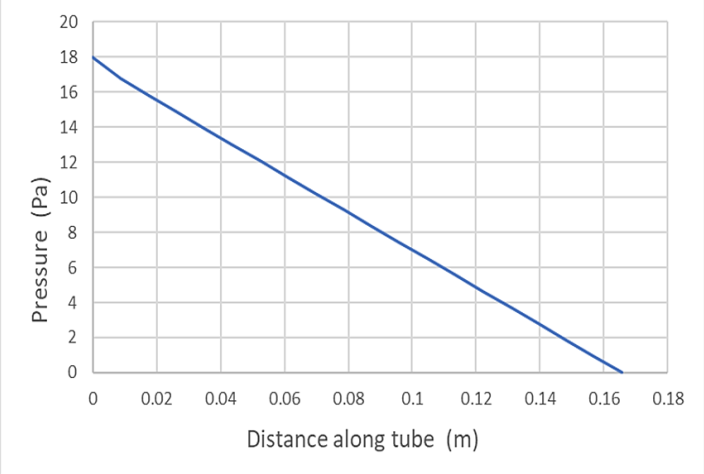

Figure 6: Pressure profile of water side along the tube length

Contour of static temperature

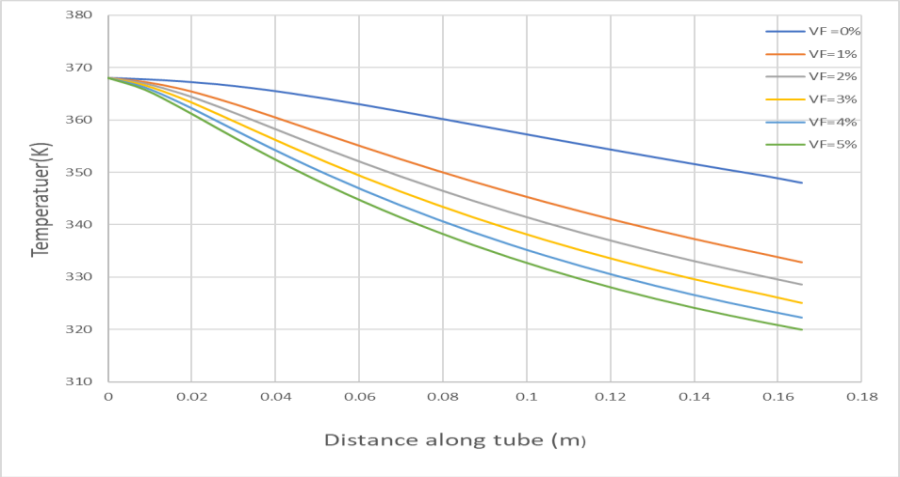

Figure 7: Variation of Temperature along the tube for nanofluid (Water with CuO particles) with volume fraction at fixed Reynold number (Re=200).

Fig. 7 shows temperature distribution along tube for a fixed Reynolds number and various volume fraction. Form the graph we can shows the deviation of temperature due to change volume fraction for a fixed Reynolds number. It has been found that temperature decreases with increases of volume fraction. Temperature contours for a fixed Reynolds number and various volume fraction at outlet and midplane is shown in Fig. 8. From the contour it has been found that temperature decreases with increases of volume fraction.

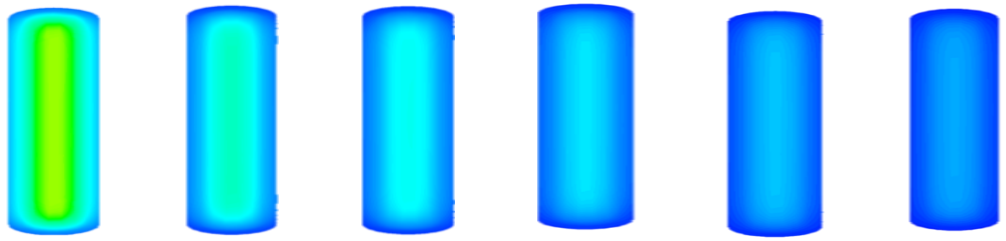

a)*vf*=0 (outlet) b)*vf*=0.01 (outlet) c)*vf*=0.02 (outlet) d)*vf*=0.03 (outlet) e)*vf*=0.04 (outlet) f)*vf*=0.05 (outlet)

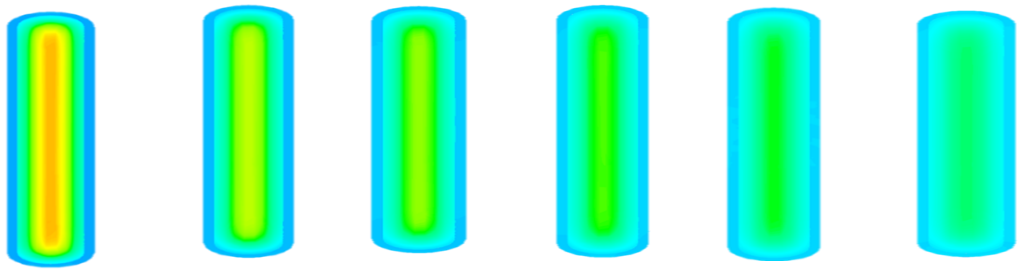

a)*Vf*=0% (midplane) b)*vf*=1% (midplane) c)*vf*=2% (midplane) d)*vf*=3% (midplane) e)*vf*=4% (midplane) d)*vf*-5% (midplane)

Figure 8: Contours of Static temperature at at the midplane and the outlet for nanofluid (Water with CuO particles) with different volume fraction (φ = 0 - 5%) (Ra=200)

Contour of static temperature

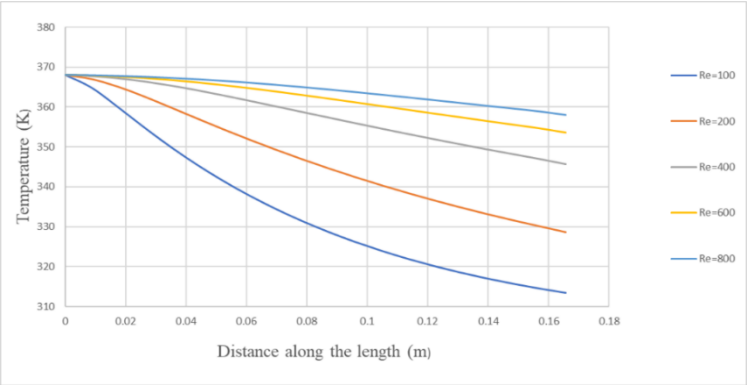

Figure 9: Variation of Temperature along the tube for nonofluid (Water with CuO particles)with different Reynold number at fixed volume fraction (vf =2%)

The Fig. 9 shows the temperature distribution for a fixed particle size and volume fraction and for different Reynold number. At low Reynold number has low temperature region and then high Reynold number high temperature region. Whereas Fig. 9 shows the temperature contour for a fixed particle size and volume fraction and for different Reynold number at outlet and mid plane.

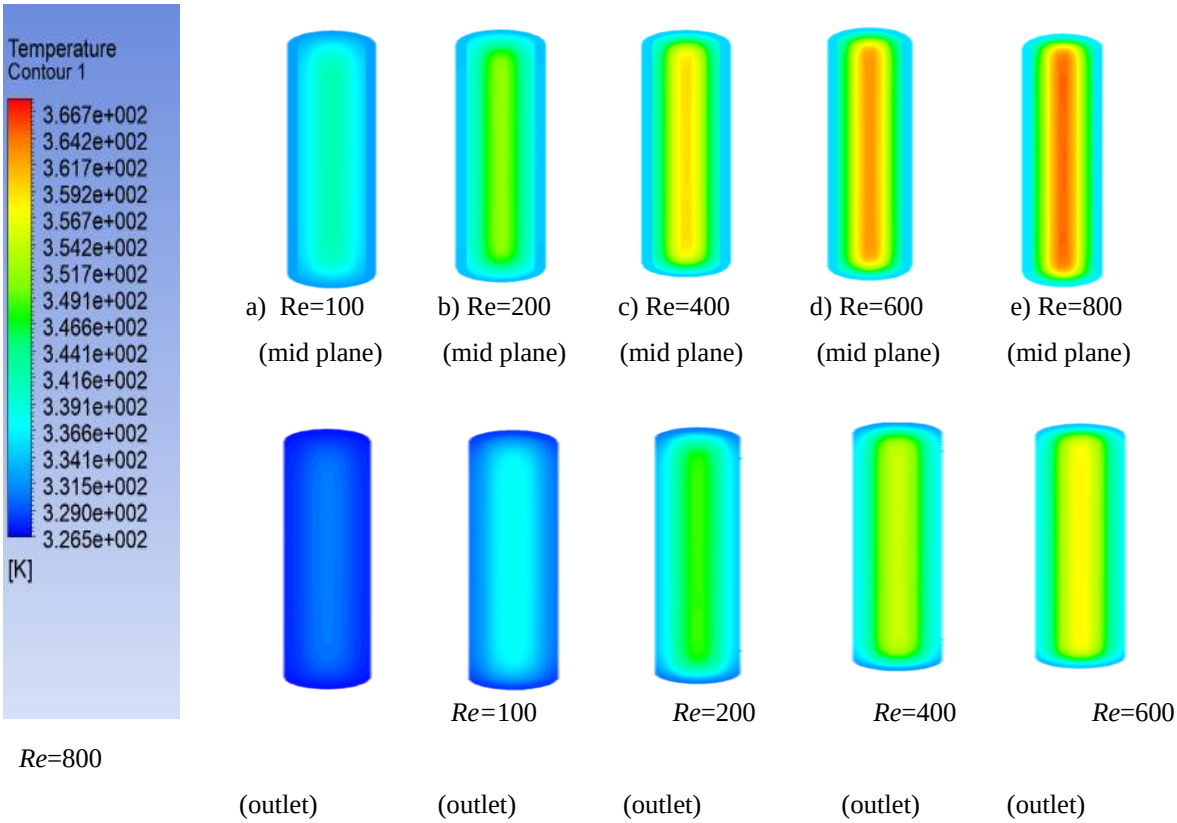

Figure 10: Temperature contour at the midplane and the outlet for nanofluid (Water with CuO particles) with Reynold number.

6. CONCLUSION

For a car radiator tube with fin the flow characteristics and heat transfer were analyzed through the numerical computation using ANSYS FLUENT 16.0. In this analysis, the investigation is performed to show the enhancement in heat transfer due to use of nano fluid instead of using pure fluids. The

investigation is done for various volume fraction of nano particle and various Reynold number nano fluid. The result clearly shows that –

i. The amount of heat transfer is increased with increased volume fraction of nano particles, as a result outlet temperature decrease with increased volume fraction.
ii. The amount of heat transfer is increased with increase Reynold number for fixed particle size and volume fraction. Low outlet temperature at low Reynold number and High outlet temperature at high Reynold number.

7. REFERENCES

[1] Rinu Sathyan "Analysis of Automobile Radiator Using Computational Fluid Dynamics" International Journal of Latest Technology in Engineering, Management & Applied Science (IJLTEMAS) Volume V, Issue VI, June 2016, ISSN 2278-2540

[2] Rajashekhar Pendyala, Jia Ling Chong, Suhaib Umer Ilyas, "CFD Analysis of Heat Transfer Performance in a Car Radiator with Nanofluids as Coolants." The Italian Association of Chemical Engineering (AIDIC) SBN 978-88-95608-36-5; ISSN 2283-9216 VOL. 45, 2015

[3] Mahendra Godley, Bhanu Pratap Singh Tomar, Ajay Tripathi "Investigation of Automobile Radiator Using Nanofluid-CuO/Water Mixture as Coolant" International Journal of Advanced Research in Science, Engineering and Technology Vol. 2, Issue 12, December 2015 ISSN: 2350-0328

[4] Elif Büyük ÖĞÜT, Metin AKYOL And Müslüm ARICI "Natural Convection Of Nanofluids In An Inclined Square Cavity With Side Wavy Walls" J. Of Thermal Science And Technology Isı Bilimi Ve Tekniği Dergisi, 37, 2, 139-150, 2017 ISSN 1300-3615

[5] Kabir Bashir Shariff, Bala Abdullahi, Saidu Bello Abubakar, Modelling and Simulation of Car Radiator: Effects of Fins under the Atmospheric Condition of Kano, Nigeria, Journal of Advanced Research in Fluid Mechanics and Thermal Sciences 48, Issue 1 (2018) 1-16.

THERMAL TRANSPORTATION FROM NANOPARTICLES DEPOSITED SOLID SURFACE

AKM M Morshed[1], Muhammad Rubayat Bin Shahadat[2], Md. Ferdous Alam[3]

[1] Department of Mechanical Engineering, Bangladesh University of Engineering and Technology, Dhaka, 1000 Bangladesh

[2] Department of Mechanical Engineering, Hajee Mohammad Danesh Science and Technology University, Dinajpur, 5200, Bangladesh

[3] Department of Mechanical Engineering, Shahjalal University of Science and Technology, Sylhet, 3114, Bangladesh

Corresponding E-mail: rubayat37.me@hstu.ac.bd

Abstract: *Non-equilibrium Molecular dynamics simulation shortly NEMD simulation was utilized with a view to understanding the thermal characteristics from nanoparticles decorated solid surface. Employed simulation domain was composed of: flat base surface made of copper, nanoparticles made of platinum, liquid argon molecules and vapor particles also formed of argon. In this recent study, the solid wall has been considered with molecular level flatness and also with nanoscale roughness. Liquid argon represented as few layers was placed on the flat wall and nanodoted solid surface. Number of nanoparticles was varied but the thickness of the liquid argon layer was kept constant throughout the total study. In the simulation domain, outside the solid wall as well as the liquid layers there was argon vapor. The simulation was commenced from t=0 ns that means initial condition and then it was allowed to come to equilibrium. After the establishment of the equilibriation of the three-phase system, the wall temperature was suddenly raised to a higher value; thus heat flow was established from the solid copper surface to argon liquid layers and liquid layers tend to evaporate. From the simulation results it was observed that because of the presence of nanoparticles on the solid wall, there is an enhance in the heat transfer from solid copper surface to liquid argon layers and thus evaporation rate becomes higher compared to flat copper surface and this enhancement can be intensified with the increase of number of the nanoparticles. However, different scenarios were obtained from the rough surface. When nanoparticles get trapped between the gaps of the corresponding nano level surface roughness, it decreases the rate of phonon transportation from the solid surface to liquid layers. .*

Keywords*: Non-equilibrium Molecular dynamics simulation, nanoparticles decorated solid surface, evaporation, surface roughness, phonon transportation,*

1. INTRODUCTION

Heat transfer from the solid wall to adjacent liquid layers strongly depends on surface textures and interface characteristics. Placing nanoparticles on a solid wall alters surface topology and thus alters inter-surface thermal transport characteristics. Nanoparticles deposited surface already has been studied for a diversity of applications i.e. solar cell [1], biological applications[2], optical transmission [3], electronic memory structures [4], sensors [5], medical imaging [6], corrosion resistance [7], heat transfer enrichment [8], etc. Surface decoration with nanoparticles for the increase of heat transfer was first noted during the pool boiling of nanofluid [9]; nanoparticles were deposited on the solid wall and formed a nonporous layer of nanoparticles, resulting an enhancement of boiling heat transfer. Recently, performance of boiling heat transfer on a solid surface is being studied by the deposition of nanoparticles [10-12]. Compared to plain polished surface, the nano porous coated surface containing numerous nucleation sites consistently augment boiling heat transfer coefficient [13]. Although nanoparticles deposited surface has been observed to increase heat transfer performance, but conflicting results are also reported in the literature; Heat transfer performance was observed by some researcher to be enhanced by 10 to 40%, whereas several researchers have reported to decrease by 20 to 40% and some researchers also have reported no change in heat transfer performance due to the introduction of nanoparticles on solid wall [14-15]. Fundamental understanding of importance of deposition of nanoparticles on rigid surface is necessary to explain the reported discrepancy and to figure out a more efficient method to modify surface for enhanced thermal transport across the surface.

Previously MD simulation was employed by many researchers to investigate thermal transport with associate phenomena between solid as well as liquid [12, 16-18]. Thermal transport between solid as well as liquid is reported to be largely dependent on various factors like solid-liquid interaction strength, temperature [19], surface wettability [20], molecular structures [21] and interfacial geometry [19]. Nanostructures placed on the interface is observed to increase the interfacial thermal conductance, hence increase thermal transportation. The deposition of nanoparticles on solid wall also increases thermal energy transfer from the solid wall to the nearby liquid by increasing contact surface and surface wettability while reducing interfacial thermal resistance by rectifying phonon frequency [17]. Although nanostructured surface and nanoparticles deposited surface have similar effects on the modification of surface morphology, but they are not same; the structures are merely a part of the solid, whereas the nanoparticles are attached very weakly with the solid wall by Van der Waals force.

Every surface has surface roughness at a nanoscale level (nanostructures, cavity, etc.) which is generated naturally during the machining or manufacturing process. This molecular level roughened surface can be treated as flat surface from the macroscopic point of persuasion. Placement of nanoparticles on a macroscopically flat surface usually means placement of nanoparticles on a nanostructured surface. Depending on the relative size of the nanostructures and the geometric characteristics of the nanostructures present on the solid wall three different categories of interface can be developed: (i) nanoparticles rests at the bottom of the flat surface; (ii) nanoparticles trapped between the clearances of the nanostructures; (iii) nanoparticles rest on top of the nanostructures.

In the present study, NEMD simulations was conducted with simplified molecular model to investigate thermal transportation behaviour from a nanoparticle deposited flat surface and nanostructured surface. Then the results were compared with that of molecular level flat surface and nanostructured surface. Effect of size and particles interaction strength was also pointed out as an important parameter in this study. The result of this study is intended to enhance our understanding about the thermal transportation behaviour from the nanoparticles deposited practical surface and could be an answer to the conflicting results of nanoparticles deposited enriched heat transfer surface and thus effective surface modification technique could be outlined.

2. SIMULATION METHODOLOGY

Classical Molecular Dynamics (MD) simulation was employed in this study which is fairly a straightforward process. The details of MD systems are as follows.

The molecular system consisted of four regions: solid copper wall, platinum nanoparticles, liquid argon, and argon vapor in a cuboid of dimension 10.5 × 56 × 10.5 nm^3. For imitating nanoscale roughness copper nanostructures (1.25 × 1 × 10.5 nm^3) were placed on top of the molecular level flat copper surfaces. A few layers of the liquid argon were placed on top of the solid surface. Spherical nanoparticles of platinum corresponding to a density of 21450 kg/m^3 are placed over the solid wall and rest of the simulation box is filled with argon corresponding to a density of 16110×10-^{3} kg/m^3. Fig. 1 presents details of the simulation domain, wall configuration and nanoparticles size and position used in this study.

The well-known Lenard-Jones (12-6) potential [22] has been used to mediate the interactions between the atoms.

$$\emptyset\,(\boldsymbol{r}) = \boldsymbol{4\varepsilon}\,[\,\left(\frac{\sigma}{r}\right)^{\mathbf{12}} - \left(\frac{\sigma}{r}\right)^{\mathbf{6}}\,] \qquad (1)$$

Although it has been found that the Embedded Atom Method (EAM) potential is more appropriate for Pt-Pt interaction nevertheless LJ potential yields good results for qualitative conclusion. To increase the computational efficiency, all the potentials were truncated at 3.4σ Ar-Ar.

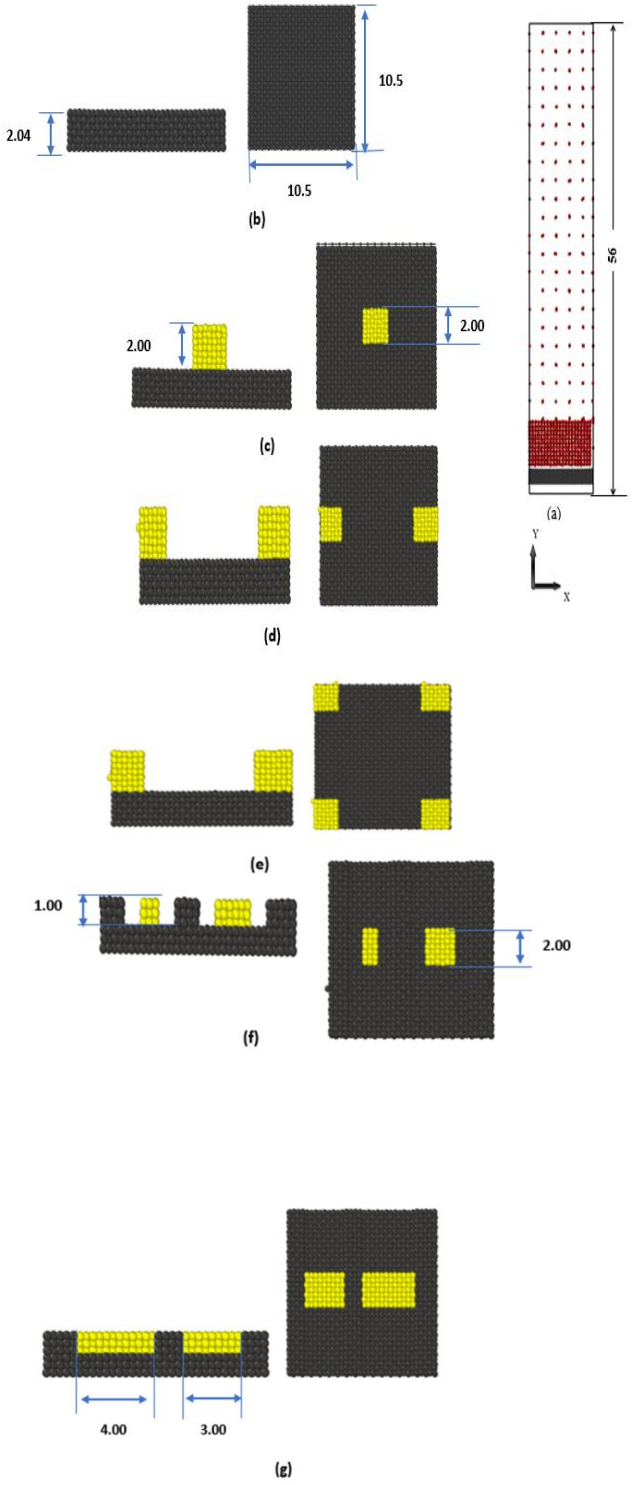

Figure 1: Simulation domain, wall and nanoparticle configuration on molecular level flat surface and with surface roughness (a: configuration of the simulation domain; b: configuration of the flat surface; c: configuration of the flat surface with single nanoparticle (surface_1); d: configuration of the flat surface with two nanoparticles (surface_2); e: configuration of the flat surface with four nanoparticles

(surface_3); f: configuration of the nanoparticles trapped in roughness with clearance (surface_4); g: configuration of the nanoparticles trapped in roughness with no clearance (surface_5)

The length and energy parameters of the interaction potential were obtained from the references [18, 23-24].

Table 1: Governing Parameters

Parameters	Value	Unit
$\sigma_{Ar\text{-}Ar}$	0.3405	nm
$\varepsilon_{Ar\text{-}Ar}$	1.67×10^{-21}	J
$\sigma_{Cu\text{-}Cu}$	0.2242	nm
$\varepsilon_{Cu\text{-}Cu}$	45×10^{-21}	J
$\sigma_{Pt\text{-}Pt}$	0.2475	nm
$\varepsilon_{Pt\text{-}Pt}$	83.46×10^{-21}	J
$\sigma_{Ar\text{-}Pt}$	0.294	nm
$\varepsilon_{Ar\text{-}Pt}$	5.89×10^{-21}	J
$\sigma_{Ar\text{-}Cu}$	0.2872	nm
$\varepsilon_{Ar\text{-}Cu}$	10.42×10^{-21}	J
$\sigma_{Cu\text{-}Pt}$	0.2376	nm
$\varepsilon_{Cu\text{-}Pt}$	37.24×10^{-21}	J

Velocity-varlet algorithm has been used to integrate the equations of motions and a time step 5 fs has been used for the simulations. Periodic boundary conditions were imposed laterally (x and z direction) while the bottom layer of the wall was kept fixed in order to avoid any migration of the sample [25]. Besides, a Langevin thermostat was applied to the next three layers, adiabatic imaginary boundary condition was applied to the top of the simulation domain. Adiabatic [26-33] and open boundary condition [34] both were used previously in explosive boiling simulation and no noticeable difference was observed in their results for that boundary condition. Adiabatic boundary condition helps us keep the number of atoms constant through the simulation and thus same simulation condition can be used for the present condition. The simulation was started from the initial configuration of the domain, the Langevin thermostat was switched on at 90 K and the simulation continued for 2 ns. Then the simulation domain was allowed to equilibrate for another 4ns switching off the thermostat.

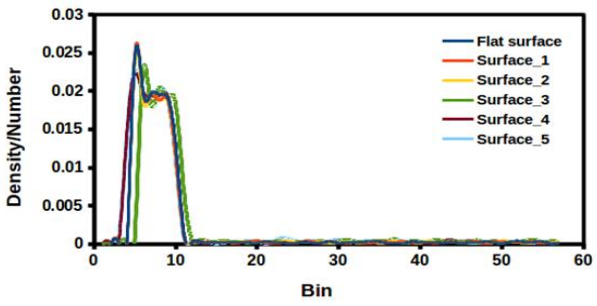

(a)

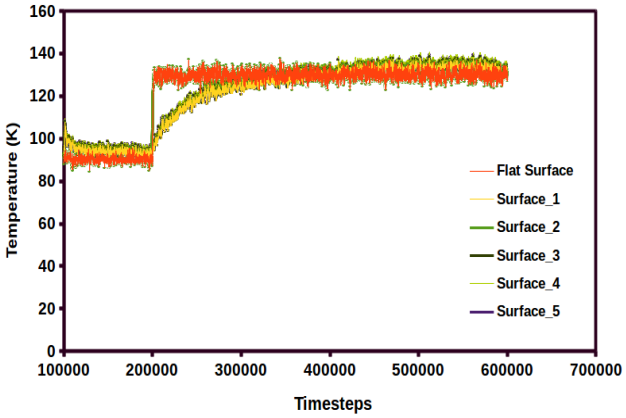

(b)

Figure 2: (a) Density profile of argon (b) Temperature profile of argon

During the equilibration period temperature, pressure, and density of the argon atoms were monitored to check whether it was in the equilibrium state or not. In case of a flat surface, the density profile of argon atoms at the end of the equilibration period is presented in Fig. 2. (a). Compared to the phase diagram of the Lenard–Jones system [34-35], they are obviously in an equilibrium liquid-vapor system. At the tail end of the equilibrium period, to initiate phase transition, the Langevin thermostat was set to jump to 130 K to start the evaporation. The topmost wall which is comprised of top three layers of copper wall retorted very fast and it goes to equilibrium with the intended temperature within 10 ps; the simulation was run for 6 ns. Fig. 2. (b) shows the corresponding temperature profile of argon. All the simulations were performed in Linux platform using LAMMPS [36] and visualization was done using OVITO [37].

3. RESULTS AND DISCUSSION

3.1 Thermal transport from nano structured surface

Nanostructures present on a solid wall alters surface texture and morphology and thus thermal transport behaviour of the surface is also altered. Thermal transportation behaviour of the nanostructured surface was compared with that of a flat surface based on evaporation rate. When the solid wall was subjected to heating (130 K which is just above the boiling point of the adjacent liquid) heat flows from the solid surface to the liquid and it starts to evaporate. In Fig. 3 evaporation rate of the nanostructured surface is compared to the flat surface. For this simulation, the evaporation rate was calculated by counting the rate of change of the liquid molecules (liquid argon) in the vapor regime. The evaporation rate increases with time for both the surfaces, but evaporation rate decreases earlier for the nanostructured surface compared to the flat surface, which implies that liquid molecules have been evaporated earlier for the nanostructured surface. Due to presence of the nanostructures, surface wettability, solid-liquid contact area increases, and interfacial thermal resistance

decreases which increase the thermal transportation from the solid surface to the liquid surface resulting in higher evaporation rate. Similar results have been also reported previously.

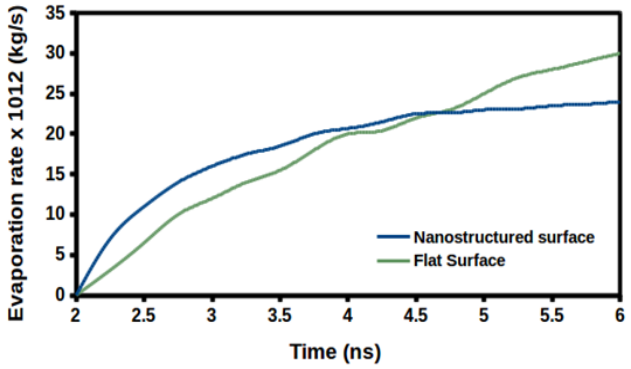

Figure 3: Evaporation rate from the nanostructured surface compared to the flat surface

3.2 Thermal transport from the nanoparticles deposited solid surface

Fig. 4 compares the evaporation rate for nanoparticle deposited solid surfaces. In present case, the surface remains flat while the number of particles deposited on the solid surfaces has been varied. With the increase of the number of nanoparticles, the rise of evaporation rate increases, while the maximum rate of evaporation decreases. For nano structured surfaces the particles go to vapor phase earlier compared to flat surface. Hence initially the rate of evaporation is larger in flat surface. For surface_3 there is more nano particles compared to surface_2, surface_1 and flat surface. Hence initially the rate is larger in surface_3. But as time goes on, evaporation rate increases at a slower rate as liquid molecules have already evaporated.

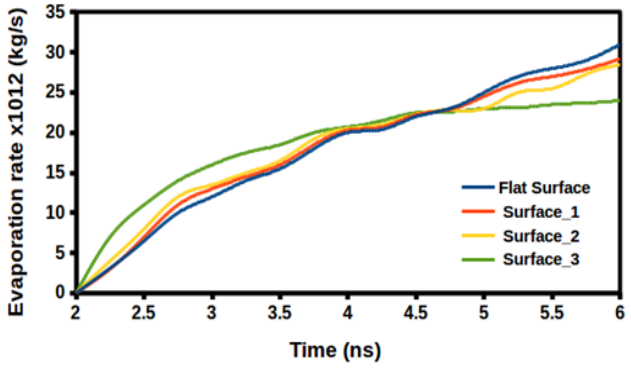

Figure 4: Evaporation rate from the nanoparticle deposited solid surfaces

3.3 Thermal transport from the nanoparticles deposited nanostructured surface

Fig. 5 compares the evaporation rate for nanoparticle deposited rough surfaces. Unlike the nanoscale flat surfaces, for the case of rough solid surfaces, the rise of evaporation remains nearly same in all the cases, while it follows the similar conclusion to the previous case that the maximum evaporation rate decreases with the increase of the number of particles. But surface_4 is slightly better than surface_5 because for surface_4 nano particles are trapped in the surface having clearance with the roughness. In this case the effective surface area is higher than surface_5 where the nano particles are trapped in roughness but having no clearance.

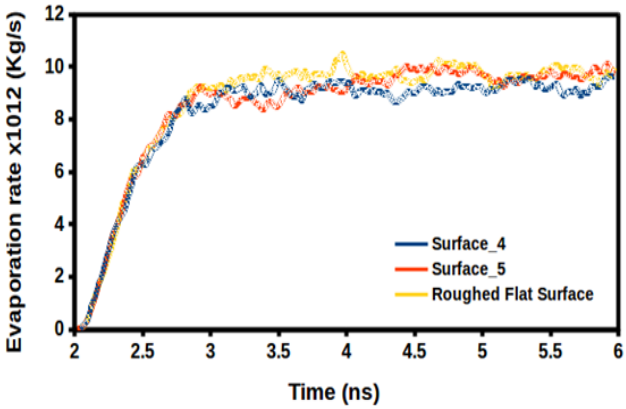

Figure 5: Evaporation rate from the nanoparticle deposited rough surface

In Fig. 6, surface_3 the density profile for surface_3 is initially shifted to higher bins. That means more liquid particles are evaporated than the other surfaces. At initial condition the density of particles is nearly zero in higher bins. At 2ns, there is an increase of density of particles in the higher bins compared to initial condition due to continuous evaporation. As time goes on the density in higher bins increases because of evaporation of liquid to vapor.

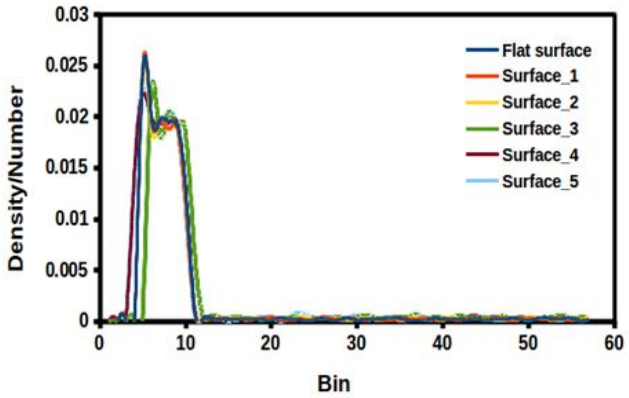

(a)

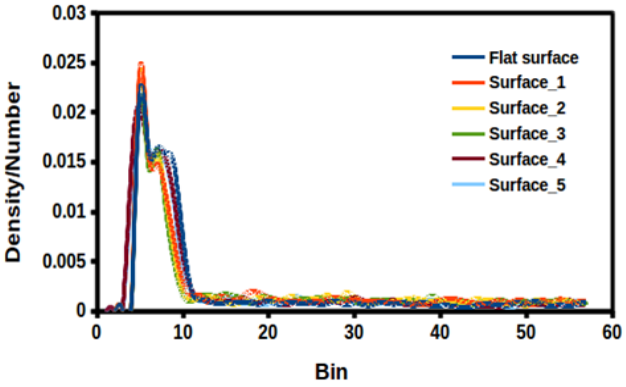

(b)

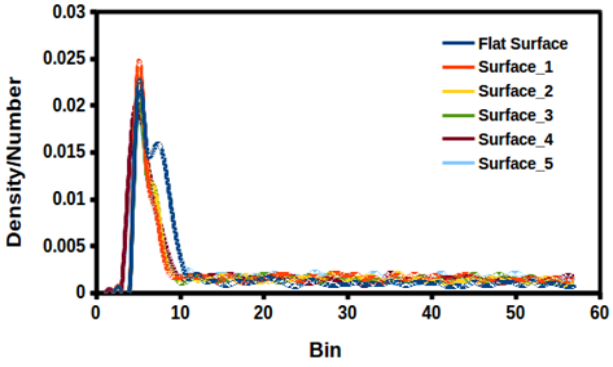

(c)

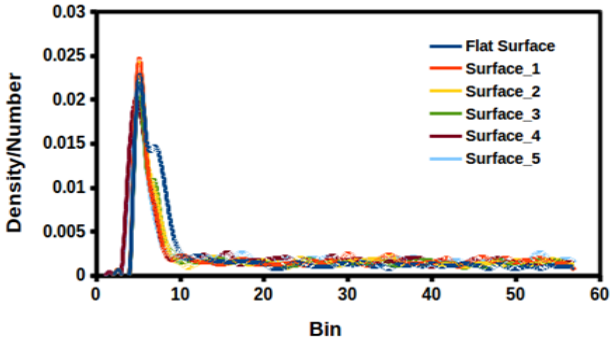

(d)

Figure 6: Density profiles at (a) initial condition, (b) 2 ns, (c) 4.5 ns and (d) 6 ns

These evaporation phenomena can also be explained by RDF or radial distribution function, g(r). RDF basically means the probability of finding out a particle at a certain distance from a reference particle. Here the cut off distance has been considered as 11.934 nm. The data files are imported from OVITO. From Fig. 7 (a) and (d), it can be shown that for flat surface and surface_5 the rdf has nearly similar value. Within very low cut off distance the value of rdf is high as at very low distance for these two surfaces the evaporation rate is low. For surface_4, it is slightly better than surface_5 and for surface_4, the value of rdf is low at low cut off distance compared to surface_5 and the value of rdf is high at higher cut off distance compared to surface_5 due to slight high evaporation rate.

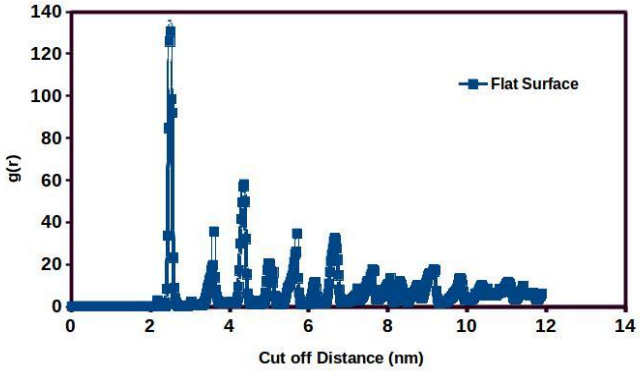

(a)

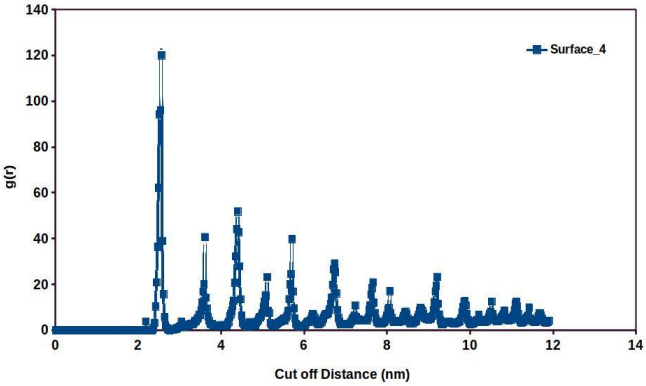

(b)

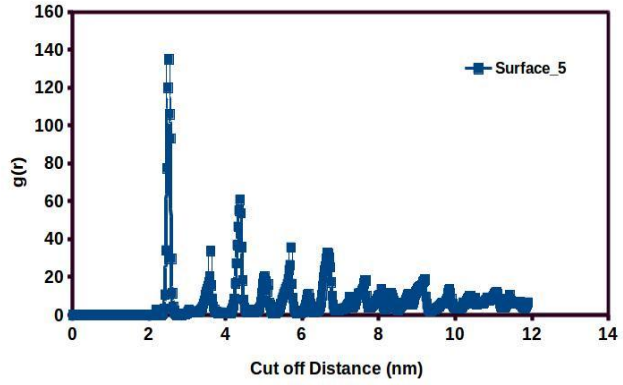

(c)

Figure 7: Radial distribution function of argon for (a) flat surface (b) Surface_4 and (c) Surface_5

Fig. 8 shows the snapshots of simulation domains during evaporation

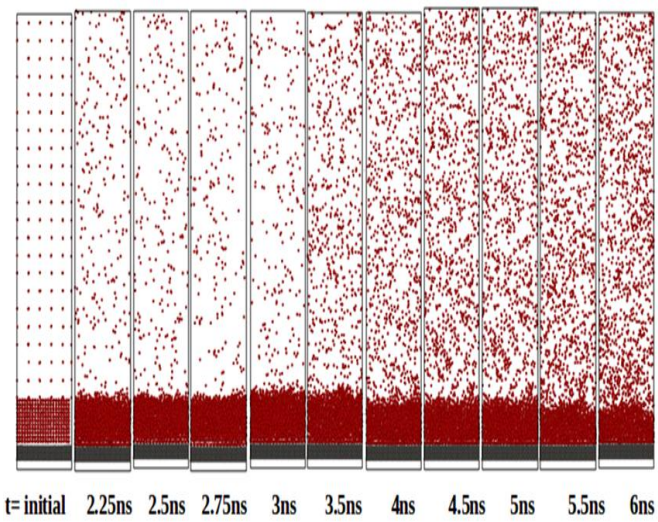

(a)

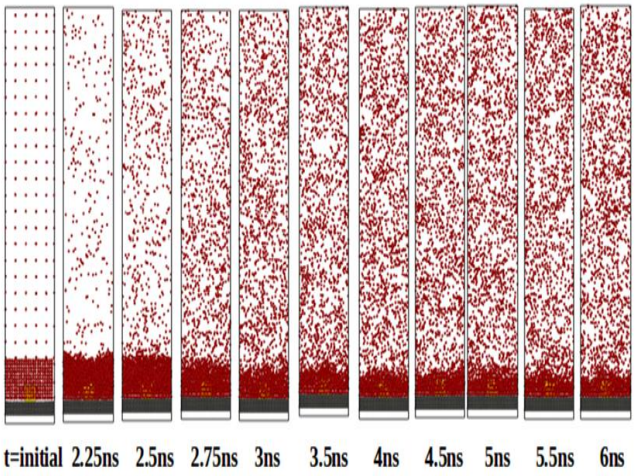

(b)

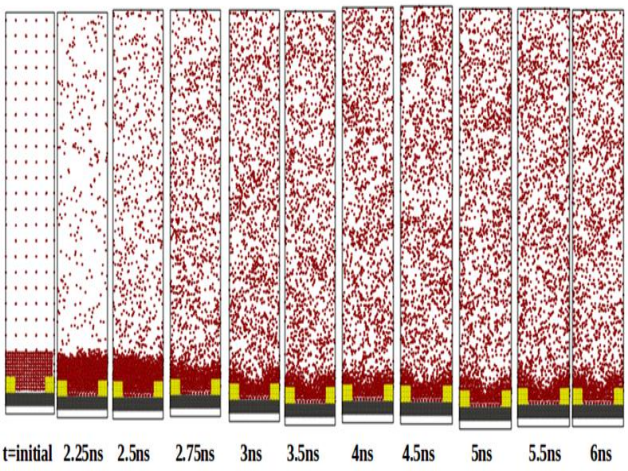

(c)

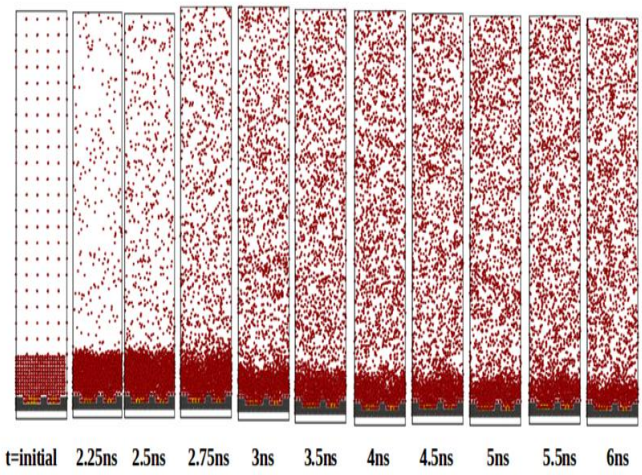

(d)

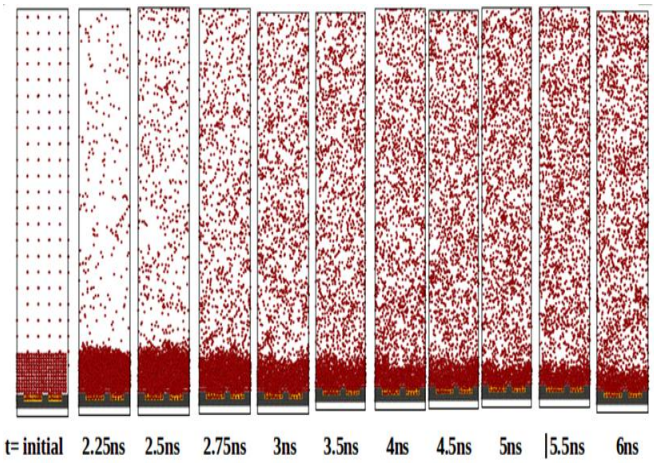

(e)

Figure 8: The snapshots of simulation domains during evaporation for (a) flat surface (b) surface_1 (c) surface_3 (d) surface_4 (e) surface_5

4. CONCLUSION

Non-equilibrium Molecular Dynamics (NEMD) simulations was employed to investigate the thermal transportation behaviour of a nanoparticle deposited molecular level flat surface and nanostructured surface in this section. The following conclusions can be made with this study:

a) With the presence of the nanostructures, surface wettability, solid-liquid contact area increases and interfacial thermal resistance decreases, which increase the thermal transportation from the solid surface to the liquid surface resulting in higher rate of evaporation.

b) With the increase of the number of nanoparticles, the rise of evaporation rate increases, while the maximum rate of evaporation decreases.

c) For a nanostructured rough surface there is no significant change in the rise of evaporation rate whether the nano particles are fully trapped in the roughness or not.

5. NOMENCLATURE

φ(r)	Interatomic potential between two atoms	(KJ)
ε	Intensity of force/ well depth	(KJ/mol)
σ	Length factor	(Angstrom)
r	Distance between the particles	(Angstrom)

6. REFERENCES

[1] Kwong, C.Y., 2004, "Poly (3-hexylthiophene):TiO2 nanocomposites for solar cell applications." Nanotechnology, Vol. 15(9): p. 1156.

[2] Sperling, R.A., 2008, "Biological applications of gold nanoparticles." Chemical Society Reviews, Vol. 37(9): pp. 1896-1908.

[3] Xu, X., M. Stevens, and M.B. Cortie, 2004, "In Situ Precipitation of Gold Nanoparticles onto Glass for Potential Architectural Applications." Chemistry of Materials, Vol. 16(11): pp. 2259-2266.

[4] Paul, S., 2003, "Langmuir−Blodgett Film Deposition of Metallic Nanoparticles and Their Application to Electronic Memory Structures." Nano Letters, Vol. 3(4): pp. 533-536.

[5] Leite, E.R., 2004, "A New Method to Control Particle Size and Particle Size Distribution of SnO2 Nanoparticles for Gas Sensor Applications." Advanced Materials, Vol. 12(13): pp. 965-968.

[6] Fang, C. and M. Zhang, 2009, "Multifunctional magnetic nanoparticles for medical imaging applications." Journal of Materials Chemistry, Vol. 19(35): pp. 6258-6266.

[7] Borisova, D., H. Möhwald, and D.G. Shchukin, 2011, "Mesoporous Silica Nanoparticles for Active Corrosion Protection." ACS Nano, Vol. 5(3): pp. 1939-1946.

[8] You, S., J. Kim, and K. Kim, 2003, "Effect of nanoparticles on critical heat flux of water in pool boiling heat transfer." Applied Physics Letters, Vol. 83(16): pp. 3374-3376.

[9] Alam, Md. Ferdous, Shahadat, Muhammad Rubayat Bin, Morshed, AKM M, Paul and Titan C., 2018, "A molecular dynamics study of boiling on a nano dot decorated solid surface", 3rd Thermal and Fluids Engineering Conference (TFEC), Fort Lauderdale, USA, ASTFE Digital Library, pp. 1599-1608.

[10] Morshed, A.K.M.M., T.C. Paul, and J.A. Khan, 2013, "Effect of Al2O3 nanoparticle deposition on flow boiling performance of water in a microchannel." Experimental Thermal and Fluid Science, Vol. 47(0): pp. 6-13.

[11] Morshed, A.K.M.M., T.C. Paul, and J. Khan, 2013, "Effect of Cu–Al2O3 nanocomposite coating on flow boiling performance of a microchannel." Applied Thermal Engineering, Vol. 51(1–2): pp. 1135-1143.

[12] Morshed, A.M., A. Rezwan, and J.A. Khan, 2014, "Two-phase Convective Flow in Microchannel with Nanoporous Coating." Procedia Engineering, Vol. 90, pp. 588-598.

[13] Chang, J. and S. You, 1997, "Boiling heat transfer phenomena from microporous and porous surfaces in saturated FC-72." International Journal of Heat and Mass Transfer, Vol. 40(18), pp. 4437-4447.

[14] Stutz, B., 2011, "Influence of nanoparticle surface coating on pool boiling." Experimental Thermal and Fluid Science, Vol. 35(7), pp. 1239-1249.

[15] Taylor, R.A. and P.E. Phelan, 2009, "Pool boiling of nanofluids: comprehensive review of existing data and limited new data." International Journal of Heat and Mass Transfer, Vol. 52(23), pp. 5339-5347.

[16] Morshed, A.K.M.M., T. Paul, and J. Khan, 2011, "Effect of nanostructures on evaporation and explosive boiling of thin liquid films: a molecular dynamics study." Applied Physics A, Vol. 105(2), pp. 445-451.

[17] Nagayama, G., M. Kawagoe, and T. Tsuruta. 2007, "Molecular dynamics simulations of interfacial heat and mass transfer at nanostructured surface." First International Conference on Integration and Commercialization of Micro and Nanosystems, American Society of Mechanical Engineers.

[18] Nagayama, G., 2010, "On the evaporation rate of ultra-thin liquid film at the nanostructured surface: A molecular dynamics study." International Journal of Thermal Sciences, Vol. 49(1), pp. 59-66.

[19] Morshed, A., T.C. Paul, and J.A. Khan, 2013, "Atomistic simulation of temperature dependent thermal transport across nanoconfined liquid." Physica E: Low-dimensional Systems and Nanostructures, Vol. 47, pp. 246-251.

[20] Nagayama, G., S. Shi-iki, and T. Tsuruta, 2007, "Effects of naostructures on surface wettability: a molecular dynamics study." Transactions of the Japan Society of Mechanical Engineers B, Vol. 73(728), pp. 1084–1091.

[21] Morshed, A.M., A.A. Rezwan, and J.A. Khan, 2014, "Two-phase Convective Flow in Microchannel with Nanoporous Coating." Procedia Engineering, Vol. 90(0), pp. 588-598.

[22] Lennard-Jones, J.E. and A.F. Devonshire, 1937, "Critical Phenomena in Gases. I." Proceedings of the Royal Society of London. Series A - Mathematical and Physical Sciences, Vol. 163(912), pp. 53-70.

[23] Sarkar, S. and R.P. Selvam, 2007, "Molecular dynamics simulation of effective thermal conductivity and study of enhanced thermal transport mechanism in nanofluids. Journal of Applied Physics, Vol. 102(7), pp. 074302.

[24] Bo Shi, V.K.D., 2009, "Molecular dynamics simulation of the contact angle of liquids on solid surfaces." The Journal of Chemical Physics, Vol. 130.

[25] Dou, Y., et al., 2001, "Explosive Boiling of Water Films Adjacent to Heated Surfaces: A Microscopic Description." The Journal of Physical Chemistry A, Vol. 105(12), pp. 2748-2755.

[26] A.K.M.M. Morshed, T.C.P., Jamil A. Khan, 2011, "Effect of nanostructures on evaporation and explosive boiling of thin liquid films: a molecular dynamics study." Appl Phys A, Vol. 105, pp. 445–451.

[27] Morshed, A.K.M.M., 2012, "Thermal Transport Across Nano Engineered Solid-Liquid Interfaces." Theses and Dissertations, University of South Carolina.

[28] Morshed, A.K.M.M. and J.A. Khan, 2010, "Numerical Analysis of Single Phase Multi Layered Micro-Channel Heat Sink With Inter-Connects Between Vertical Channels." ASME Conference Proceedings, Vol. 2010(49415), pp. 133-140.

[29] Morshed, A.K.M.M., Yang, Fanghao, Ali, M. Yakut, Khan, Jamil A., Li, Chen, 2012, "Enhanced flow boiling in a microchannel with integration of nanowires." Applied Thermal Engineering, Vol. 32(0), pp. 68-75.

[30] Hopkins, P.E., 2013, "Thermal Transport across Solid Interfaces with Nanoscale Imperfections: Effects of Roughness, Disorder, Dislocations, and Bonding on Thermal Boundary Conductance." ISRN Mechanical Engineering, Vol. 2013, pp. 1-19.

[31] Liu, Q.-X., P.-X. Jiang, and H. Xiang, 2010, "Molecular dynamics simulation of thermal conductivity of an argon liquid layer confined in nanospace." Molecular Simulation, Vol. 36(13), pp. 1080-1085.

[32] Liu, Y., 2005, "Fluid structure and transport properties of water inside carbon nanotubes." Journal of Chemical Physics, Vol. 123. pp. 234701.

[33] Li, Q. and C. Liu, 2012, " Molecular dynamics simulation of heat transfer with effects of fluid–lattice interactions." International Journal of Heat and Mass Transfer, Vol. 55(25-26), pp. 8088-8092.

[34] Gu, X. and H.M. Urbassek, 2005, "Atomic dynamics of explosive boiling of liquid-argon films." Applied Physics B: Lasers and Optics, Vol. 81(5), pp. 675-679.

[35] Kofke, D.A., 1993, "Direct evaluation of phase coexistence by molecular simulation via integration along the saturation line." Journal of Chemical Physics, Vol. 98 (5).

[36] Plimpton, S.J., 1995, "Fast Parallel Algorithms for Short-Range Molecular Dynamics." J. Comp Phys, Vol. 117, pp. 1-19.

[37] Stukowski, A., 2010, "Visualization and analysis of atomistic simulation data with OVITO–the Open Visualization Tool." Modelling and Simulation in Materials Science and Engineering, Vol. 18(1), pp. 015012

FABRICATION AND CHARACTERIZATION OF JUTE/GLASS FIBER REINFORCED EPOXY HYBRID COMPOSITES

Khurshida Sharmin[1], Jahangir Alam[1], Mohammad Washim Dewan[1*]

[1]Department of Mechanical Engineering

Dhaka University of Engineering and Technology, Gazipur, Bangladesh

Corresponding E-mail: washim0179@duet.ac.bd

Abstract: *The improved properties (i.e., low cost, low density, eco-friendly) of natural fibers have made them as a promising reinforcement in hybrid composites without sacrificing mechanical properties. In this study jute and e-glass fiber reinforced hybrid composites are fabricated utilizing hand lay-up followed by compression molding. Room temperature cured two part epoxy resin is used as a matrix. Approximate 6-7 mm thick composite panels are fabricated utilizing 17 layers of woven glass and jute fibers - only jute, only glass, glass and jute alternatively and 4 glass - 9 jute – 4 glass layering sequences. The fabricated composite panels are analyzed through fiber volume calculation, tensile test and water absorption; and the effect of chemical treatment on the woven jute fiber is also investigated. The hybridization of jute and glass fiber results in better tensile and water absorption properties than only jute fiber reinforced composites but inferior properties as compared to only glass fiber reinforced composites. A chemically treated jute fiber reinforced hybrid composite shows about 20% improvements in tensile strength as compared to untreated hybrid composite panel. Water absorption is found to be 22% improved for 4 glass – 9 jute – 4 glass fibers layering sequence than glass – jute fiber alternatively layered sequence.*

Keywords*: Hybrid Composites, Compression Molding, Chemical Treatment, Mechanical Properties, Water Absorption*

1. INTRODUCTION

Fiber reinforced polymer composites have been extensively utilized for many structural applications like automotive parts, airplanes interior parts, household appliances, and construction materials [1]. Synthetic fibers (carbon, glass, aramid) are generally utilized as reinforcing elements to fabricate composite materials for better mechanical and thermal properties. However, they are expensive and non-biodegradable. The environmental concerns have led to substantial attention in the development of new composite materials with addition of more than one reinforcement that is biodegradable resources, such as natural fibers (i.e., jute, kenaf, hemp, bamboo, wood, etc.) [2, 3]. Natural fiber reinforced composites exhibit lower mechanical properties than synthetic fiber reinforced polymer composites. However, natural fiber reinforced composites properties can be extended by hybridization with synthetic fibers and can provide a sustainable alternative to existing engineering materials in many structural applications. The hybrid fiber reinforced polymer composites can be manufactured by adopting various manufacturing techniques such as- hand lay-up, compression molding, injection molding, auto-clave, and vacuum assisted resin transfer molding (VARTM) process [4].

There are some studies reported on jute fiber reinforced hybrid composites [5-8]. Ramesh et al. [7] investigated the randomly oriented jute/glass fiber (GF) reinforced polyester composites fabricated with hand lay-up technique. Another research group studied on jute/GF reinforced-epoxy composites with 14% weight content jute fibers [9]. They utilized hand lay-up and compression molding techniques. Sabeel Ahmed et al. [10] explore the effects of hybridization of glass fiber on low velocity impact behavior and damage tolerance capability of woven jute fabric reinforced composite. The GF content increased the peak load and decreased the energy absorption. The deflection of the specimen was decreased with increasing the GF content. Shenoyet et al. [11] reported a remarkable improvement in the tensile and flexural properties of hybrid composites compared to the un-hybrid composites. It was also found that the hybrid composite offers better water absorption resistance. The layering sequence has larger effect on the flexural and inter-laminar shear properties than tensile properties. S.K. Saw and his research group [12] investigated on chemically modified jute–coir hybrid fiber reinforced epoxy composites. The Results show that the hybrid composites exhibit superior mechanical, dynamic mechanical and water absorption properties compared to the un-hybridized composites for different jute–coir combination. Experimental investigation carried out by Mishra et al. [13] depicts that addition of quite small amount of glass fiber to the pineapple leaf fiber and sisal fiber-reinforced polyester matrix improves the mechanical properties of the resulting composites. The study also reported that the water absorption tendency of composites decreased because of hybridization and treatment of bio-fibers. Most of the researchers utilized treated/untreated jute fiber and synthetic fiber (i.e. glass fiber, carbon fiber) to fabricate conventional hybrid composites.

In this study, bi-directional woven jute and glass fiber reinforced hybrid composite panels are fabricated through hand layout followed by compression molding technique.

Four different fiber layering sequences are used and analyzed the variation in tensile and water absorption properties of fabricated composite panels.

2. EXPERIMENTATION

In this present work, jute fiber and glass fiber woven mats were used as reinforcement and thermosetting polymer epoxy resin was used as matrix material. Curing reaction of epoxy resin took place at room temperature after mixing curing agent called hardener in a ratio of 3:1 to epoxy resin. The composites panels were manufactured by the hand lay-up followed by compression molding process. Fig. 1 shows the image of the compression molding machine which was used for composites panel fabrication.

Figure 1: Compression molding machine

To manufacture chemically treated jute fiber and glass reinforced hybrid composite panel, jute fibers were cleaned and immersed into 5% NaOH solution for 2 hours at room temperature. After that, the jute fibers were filtered and thoroughly washed with distilled water. Finally the NaOH treated fibers were dried in an oven at 100ºC for 2 hours.

During the fabrication process a releasing agent were sprayed onto mold surface. Then a layer of the bidirectional woven fiber was laid down, followed by a quantity of liquid epoxy resin poured onto it. The process was repeated until the required number of layers was built up. Finally these specimens were taken to the compression molding setup to apply force and remove air gap and excess resin. The panels were cured at pressurized condition at room temperature for 24 hours. Table 1 shows fabricated composite panels ID along with their fiber sequence and Fig. 2 shows images of the fabricated composite panels.

Table 1: Composite panels ID and their fiber layering sequence

Sample ID	Layering sequence
S1	Un-treated Jute (18 layers)
S2	Glass (18 layers)
S3	Un-treated Jute & Glass (17 layers**)** (glass-jute-glass-jute alternatively)
S4	Un-treated Jute & Glass (17 layers**)** (4 glass - 9 jute – 4 glass)
S5	Chemically treated Jute and Glass (17 layers) (glass-jute-glass-jute alternatively)

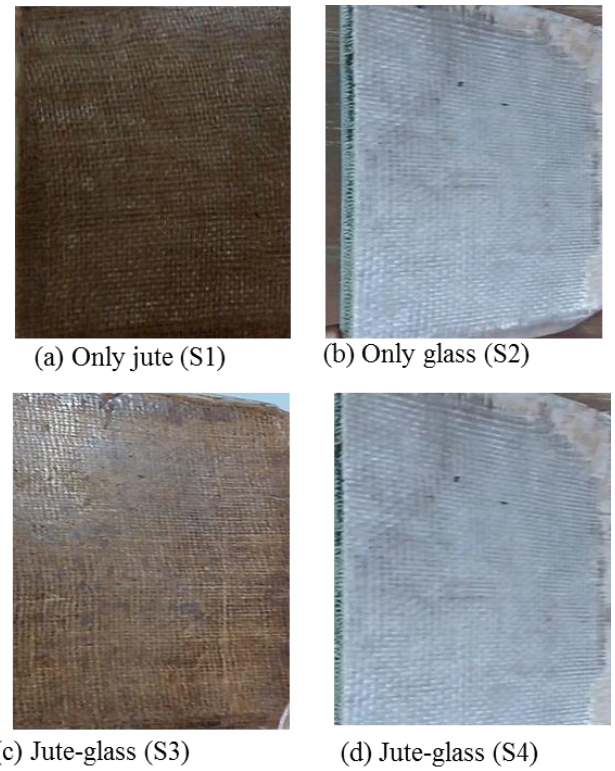

Figure 2: Images of fabricated composite panels

During composite panel fabrication, weight of jute fiber, glass fiber, and matrix were recorded. After fabrication, weight of each panel is also recorded for the calculation of fiber volume fraction. The fabricated composites were cut for mechanical testing as per the ASTM D3039 standard and for water absorption test as ASTM D790 standard.

3. RESULTS AND DISCUSSIONS

The fraction of fiber reinforcement is very important in determining the overall mechanical properties of fiber reinforced composites. A higher fiber volume fraction

typically results in better mechanical properties of the composite. The fiber volume fraction can be calculated using a combination of weights, densities and volume of the matrix and fibers. The fiber volume fraction can be calculated utilizing following three equations. The experimented data and calculated fiber volume fraction is shown in Table 2.

$$V_f = \frac{v_f}{v_c} \times 100\% \quad (1)$$

$$v_c = \frac{m_{Jf}}{\rho_{Jf}} + \frac{m_{Gf}}{\rho_{Gf}} + \frac{m_m}{\rho_m} \quad (2)$$

$$v_f = \frac{m_{Jf}}{\rho_{Jf}} + \frac{m_{Gf}}{\rho_{Gf}} \quad (3)$$

Where,

V_f = Fiber volume fraction

v_f = Volume of fiber

v_c = Volume of composite panel

m_{Jf}, m_{Gf}, m_m = Mass of jute fiber, glass fiber and matrix in the composite panel, respectively

$\rho_{Jf}, \rho_{Gf}, \rho_m$ = Density of jute fiber (1.3 g/cm³), E-glass fiber (2.62 g/cm³) and matrix (1.4 g/cm³) respectively.

Table 2: Data for mass of jute fiber, glass fiber and matrix and fiber volume fraction

Sample ID	Jute fiber mass (m_{Jf}), gm	Glass Fiber mass (m_{Gf}), gm	Matrix mass (m_m), gm	Fiber volume fraction (V_f)
S1	216	0	300	0.43
S2	0	482	150	0.63
S3	96	225	240	0.48
S4	108	200	266	0.45
S5	80	225	240	0.46

Only jute fiber reinforced composites had lowest fiber volume fraction (43%) whereas only glass fiber reinforced composite has highest fiber volume fraction (63%). In fabricated hybrid composite panels fiber volume fraction was varied from 45 to 48%.

For the tensile test, five specimens from each panel were tested on universal testing machine (UTM) at a cross head speed of 1.2 mm/min. Tensile stress strain curve of the fabricated composite samples are presented in Fig. 3. Only glass fiber reinforced epoxy composites showed average ultimate tensile strength (UTS) value of 391 MPa whereas only jute fiber reinforced composites showed average UTS value of 37 MPa. In case of hybridized composite, the average UTS values were 161 MPa and 168 MPa for two different combinations of jute and glass fiber. The average UTS values of four different samples are presented as bar graph in Fig. 4. The higher tensile strength values of the hybrid composite panels illustrate the potentiality of the use hybrid composite material in different structural applications.

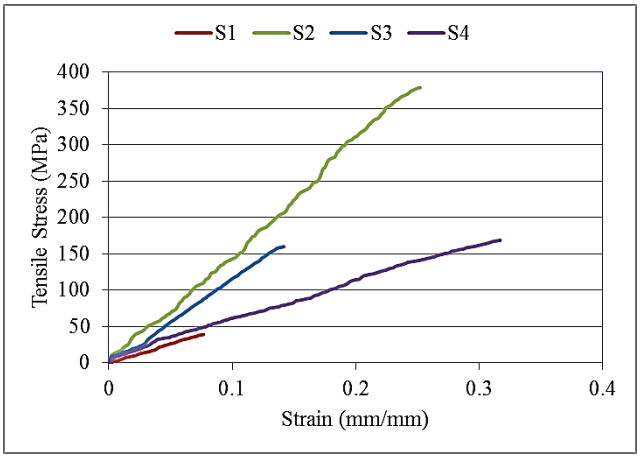

Figure 3: Tensile stress-strain curves of the fabricated composite panels

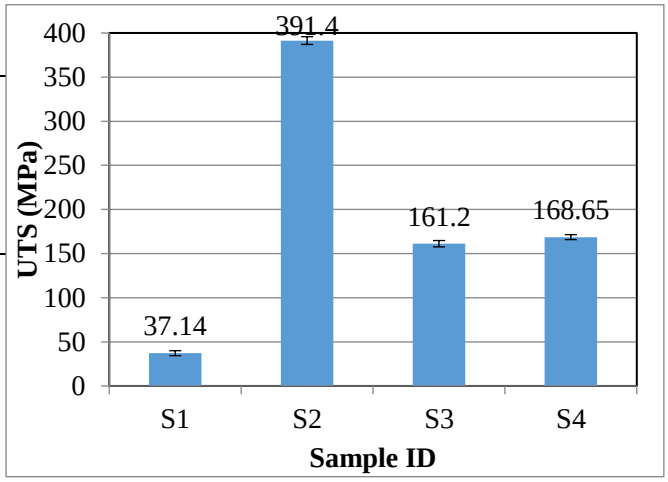

Figure 4: Average ultimate tensile strength (UTS) of fabricated composite panels

To analyze the effect of chemical treatment on jute fiber, tensile test was conducted for two hybrid composite panels having similar layering sequence. One panel contained treated jute fiber and another panel contained untreated jute fiber. Fig. 5 shows the tensile stress strain curves of untreated and treated jute fiber reinforced composite panels. Untreated jute fiber reinforced sample had average UTS value of 161 MPa whereas treated jute fiber reinforced sample had average UTS value of 192 MPa. The average result is also presented as bar graph in Fig. 6. About 20% increment in tensile strength was observed due to alkali treatment of jute fiber.

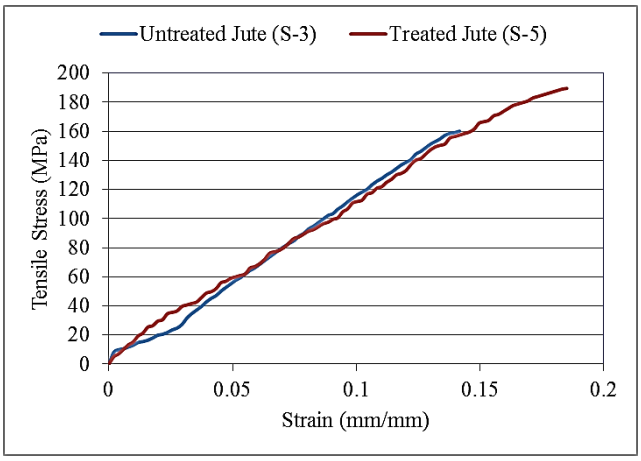

Figure 5: Tensile stress-strain curves of untreated and chemically treated jute fiber reinforced hybrid composite panels

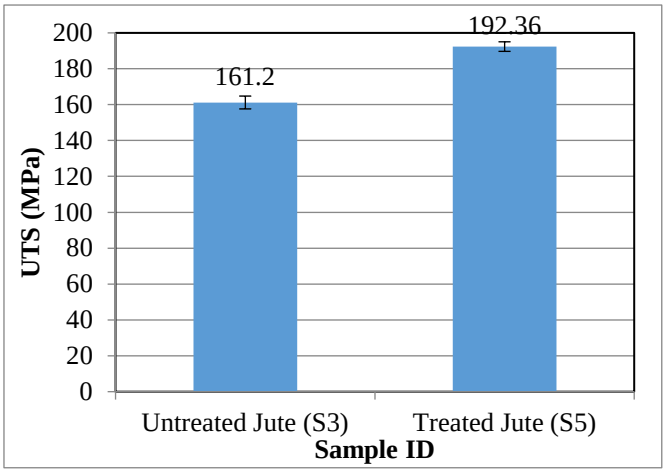

Figure 6: Average ultimate tensile strength (UTS) of un-treated and treated jute fiber reinforced hybrid composite panels

For the water absorption test, three specimens (150 mm×20mm×t) from each category were dried in an oven at 100°C temperature for 1 hour followed by cooling to room temperature in a desiccator. Immediately upon cooling the specimens were weighed (i.e. Dry weight,W_1). The weighted specimens were then emerged into distilled water at room temperature (25 °C) for 24 hours having saturation. Immersed specimens were removed, patted dry with a tissue paper and weighed (i.e. Wet weight, W_2). Water absorption is expressed as increase in weight percent.

$$Percentage\ of\ Water\ Absorption\ (\%) = [\frac{W_2 - W_1}{W_1}]\ x\ 100$$

Water absorption results are shown in Fig. 7. Sample 1(only jute epoxy) composites absorbs maximum water than any other hybrid combination of jute and glass fiber. Among the hybrid composites sample 4 (4glass+9jute+4glass) has the lowest water absorption capacity. This is due to the fact that core of S4 is protected by glass fiber on the surface.

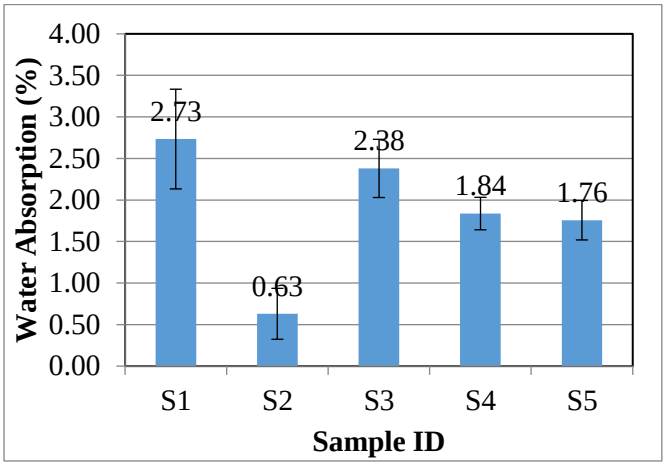

Figure 7: Average water absorption percentage of fabricated composite panels

4. CONCLUSIONS

This work is based on fabrications of hybrid composites with different combination of natural fiber (i.e. jute fiber) and synthetic fiber (i.e. e-glass fiber) as a reinforcement and epoxy resin as matrix utilizing compression molding method. The fabricated composite panels were analyzed by comparing different mechanical and physical properties. The summary of this study are as following:

- Hybridization of jute and glass fiber results in better tensile and water absorption properties as compared to only jute fiber reinforced composites.
- Tensile strength and water absorption properties of fabricated hybrid composite are varies with the variation of jute and glass fiber lamina layering seqence. The sample S3 (17 layers of glass-jute fiber alternatively arranged) resulted in highest tensile tensile propeties whereas sample S4 (4 layers glass -9 layers jute - 4 layers glass) resulted in lowest absortion properties.
- The tensile propeties of the hybrid composites can be further enhanced by chemical treatment of jute fiber.
- The fabriated light weight hybrid composite panles can be utilized in different structural application for the replacement traditional materials.

5. ACKNOWLEDGMENTS

The authors gratefully acknowledge the funding received from University Grant Commission (UGC), Bangladesh. The authors would also like to acknowledge Department of Mechanical Engineering, DUET, Gazipur for permitting to use their testing facilities.

6. REFERENCES

[1] Sathishkumar, T. P., Navaneethakrishnan, P., Shankar, S., Rajasekar, R., Rajini, N., 2013, "Characterization of natural fiber and composites – A review", Journal of Reinforced Plastics and Composites 32(19) 1457–1476.

[2] Shahzad, A., 2012, "Hemp fiber and its composites − a review", Journal of Composite Materials 46(8) 973-986.

[3] Hossain, M. K., Dewan, M. W., Hosur, M., Jeelani, S., 2011, "Mechanical performances of surface modified jute fiber reinforced biopol nanophased green composites", Composites Part B: Engineering 42(6) 1701-1707.

[4] Sathishkumar, T., Naveen, J., Satheeshkumar, S., 2014, "Hybrid fiber reinforced polymer composites – a review", Journal of Reinforced Plastics and Composites 33(5) 454-471.

[5] Jawaid, M., Khalil, H. A., 2011, "Cellulosic/synthetic fibre reinforced polymer hybrid composites: A review", Carbohydrate Polymers 86(1) 1-18.

[6] Aquino, E., Sarmento, L., Oliveira, W., Silva, R., 2007, "Moisture effect on degradation of jute/glass hybrid composites", Journal of Reinforced Plastics and Composites 26(2) 219-233.

[7] Ramesh, M., Palanikumar, K., Reddy, K. H., 2013, "Mechanical property evaluation of sisal–jute–glass fiber reinforced polyester composites", Composites Part B: Engineering 48 1-9.

[8] Akil, H. M., Santulli, C., Sarasini, F., Tirillò, J., Valente, T., 2014, "Environmental effects on the mechanical behaviour of pultruded jute/glass fibre-reinforced polyester hybrid composites, Composites Science and Technology 94 62-70.

[9] Ramesh, M., Palanikumar,K., Reddy, K. H., 2013, "Comparative evaluation on properties of hybrid glass fiber-sisal/jute reinforced epoxy composites", Procedia Engineering 51 745-750.

[10] Ahmed, K. S., Vijayarangan, S., Kumar, A., 2007, "Low Velocity Impact Damage Characterization of Woven Jute—Glass Fabric Reinforced Isothalic Polyester Hybrid Composites", Journal of reinforced plastics and composites 26(10) 959-976.

[11] Heckadka, S., Nayak, S., Prakash, A., Awasthi, A., Singh Kochhar, R., 2015, "Interlaminar shear and flexural properties of E-glass/jute reinforced polymer matrix Composites", Proceedings of International Conference on Mechanical Engineering and Industrial Automation, Dubai.

[12] Saw, S. K., Sarkhel, G., Choudhury, A., 2012, "Preparation and characterization of chemically modified Jute–Coir hybrid fiber reinforced epoxy novolac composites", Journal of Applied Polymer Science 125(4) 3038-3049.

[13] Mishra, S., Mohanty, A. K., Drzal, L. T., Misra, M., Parija, S., Nayak, S. k., Tripathy, S. S., 2003, "Studies on mechanical performance of biofibre/glass reinforced polyester hybrid composites", Composites Science and Technology 63(10) 1377-1385.

RECENT ADVANCES IN DROPLET DYNAMICS RESEARCH

N Ahmad[1], M R Rahman[2]*, M A R Sarkar[3], P R. Waghmare[4]

[1, 3]Department of Mechanical Engineering, Bangladesh University of Engineering and Technology, Dhaka

[2, 4]Interfacial Science and Surface Engineering Lab (iSSELab), Department of Mechanical Engineering, University of Alberta, Edmonton, Alberta T6G2G8, Canada.

*Corresponding E-mail: rishadrizwan71@gmail.com

Abstract: *Superior control of multi-phase micro-drops owns much of the future in micro-fluidic technology. Interfacial interaction of a droplet at a liquid-fluid interface dictates its successful generation and stability. The study of the fundamental physics of under liquid rolling dynamics is an extension of the successful generation technique. In contrast to the rigid body motion, dissipation inside and outside of a deformable drop always results in convoluted physics. While rolling on an incline, single-phase drops travel slower with increase in size. But a concealed direct dependency between the drop size and traveling velocity can be exposed by merely altering the medium resistance. Rolling motion of double emulsion droplets even affirms the presence of both of these dependencies and a control over the transition from one to the other is achievable. A threshold size limit for such a transition has been identified demonstrating that the dependency between drop size and its velocity is not unidirectional. Recent study reveals considerable advancement in understanding the dynamics that has been briefly discussed in this paper.*

Keywords*: Double emulsion drop, spreading, rolling, interface, liquid-fluid interface.*

1. INTRODUCTION

Multiphase microfluidics is a celebrated confluence in today's world. Here physics, chemistry, biology and engineering blend together [1]. It possesses enormous potential and promise in radicalizing numerous technologies and in ushering surprising simplicity in tackling problems that were otherwise believed to be complex and even impossible to deal with [2–13]. The study of multiphase droplets has been a burgeoning area of research due its wide range of applications [1, 14]. Interfacial characteristics at different phases dictate the successful generation of multiphase droplet in the miniaturize world. The complexity in identifying the role of different operating parameters for desired outcome relies on understanding of every interfacial activity. Very recently, some interesting aspects of such droplets have been investigated by Rahman and Waghmare [15, 16]. This paper briefly discusses the findings.

Generation of Double Emulsion Drop

While the potential of double emulsion drop technologies demonstrates unprecedented improvements in microfluidics, its complex multiphase nature also brings numerous barriers from application perspective. Based on the application where it is being used, the requirements of accuracy and precision vary. However, from the broader point of view, generation, control and attainment of stability with desired dispersion offer the greatest difficulties. Among different methods of double emulsion droplet generation, some of the prominent techniques can be listed based on their homogenizing principle [17] as: Stirrer technique [18], Low pressure technique [19], Stator technique [20,21], Ultrasound technique [22,23], Membrane emulsification technique [24], Micro channel technique [25], Edge based droplet generation technique [26], Spinning disk technique [27], Single and double stage high pressure technique [28–31].

The microfluidic technologies that can make improvements using the potential of double emulsion droplets, require precise volume and size control, desired dispersion and stability, and high encapsulation efficacy. However, each of the conventional methods listed in Table titled 'Drop generation techniques' fall short in full-filling one or the other of these requirements. Our research group has addressed these difficulties and limitations of double emulsion drop generation and developed a new simple technique to generate such complex drop system with precision and accuracy (manuscript under preparation). Also large number of such compound drop system can be generated in isolation from one another which increases the degree of freedom in their successful applications. This method, established in our group provides the opportunity to generate double emulsion droplets for experiments with precision and accuracy which are of prime importance in numerous applications as well as for fundamental research of such system.

In this article, we summarize two important physics of microdrops, namely spreading at the liquid-fluid interface and motion under viscous liquid. The generation of compound drop requires very good understanding of the physics at the interface which required to study the spreading parameters at the liquid-fluid interface. In order to give our readers a basic understanding of the experimental complexities, we will first discuss the spreading phenomenon. Then we will briefly discuss our findings of such rolling drops under viscous liquids. In all the experiments described in this study, single phase droplets were generated as presented in Waghmare et al. [32]. Generation of a double emulsion droplet requires designing of a customized device as depicted in Fig. 1.

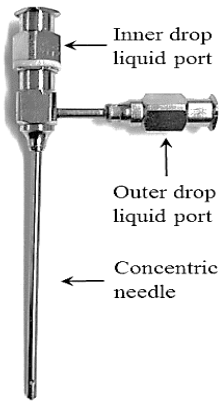

Figure 1: Generation of double emulsion drop using a concentric needle-pair (Custom coaxial needle, 100−10 coaxial, ramehart instrument co.)

This technique uses a concentric needle pair with two different inlets for pumping the fluids. With a smaller diameter (do = 0.5 mm), the inner needle is projected outside of the outer needle which has a larger diameter (do = 1.8mm). For a double emulsion drop, the inner needle was connected with the deposition unit of DSA 100E (KRUSS GmbH) while a secondary pump was connected with the inlet port of the outer needle. First, the outer phase liquid was pumped through the outer drop inlet port (port o) with precise volume and a drop was generated with the inner needle projected inside the drop. Then the inner drop deposition unit of DSA 100E pumped the inner drop liquid at desired flow rate and volume to generate an inner drop inside the already generated outer drop. The generated double-emulsion drop at the tip of the co-axial needle is further impacted on a liquid-fluid interface to get the successful detachment of the double emulsion drop form the needle.

2. INTERFACIAL DETACHMENT

Although the generation of such a controlled double emulsion drop is always challenging but possible with a high level customized device, more challenge lies in its successful detachment from the needle without distortion in shape and size. However, this detachment process is not simple for even single phase droplets. A non-intrusive needle less deposition method [32, 33] was deployed to achieve detachment without any shape distortion. Being substrate independent, this method enabled us to successfully deposit our single and double emulsion drop on the experimented substrates irrespective of their wettability. The detachment technique utilizes the difference of interfacial tensions of the associated fluids and imbalance of forces acting at the interface. As shown in Fig. 2, a drop is first generated inside a liquid bath in a cuvette (Step I). Then a thin liquid lens is formed by dispersing an appropriate lighter liquid at the interface. After this step, the needle with the drop contained at its tip is pulled through the interface (Step II). As the drop hits the interface, it creates imbalance of interfacial forces and results in similar scenario as drop impact on liquid repellent surface. This facilitates the detachment of the drop from the needle. Careful selection of interface for lens does not permit the drop to spread on the interface. The selection of denser liquid compared to the liquid in the cuvette allows us to observe the fall of the drop in liquid bath. This idea of single phase drop deposition also applies for a compound drop provided that all the liquids are carefully selected with appropriate interfacial tensions and densities. As stipulated earlier, the successful detachment, however, is not very much trivial to occur in any liquid-fluid-drop combinations, rather requires careful selection of the liquids. Also, it is important to note here, all liquid-drop combinations do not require a lens for detachment. Instead, a liquid-air interface appear to be sufficient to detach the drop from the needle for certain combinations which can be easily explained by the Neumann triangle concept [34, 35]. Being a complicated phenomenon, this needle less deposition or detachment at the interface requires attention, careful consideration of different parameters and understanding the interfacial physics. Unwanted spreading at the interface further complicates the situation. In order to investigate multiphase droplet dynamics experimentally, knowledge of spreading at the interface is an essential prerequisite for successful detachment. A comprehensive description of a detail experimental study on interfacial spreading has been reported by Rahman et al. [16]. With the required information, double emulsion drop detachment setup can be extended further to investigate further physical phenomena. A classical problem of drop rolling under viscous medium was studied by Rahman and Waghmare [15]. The authors further extended their single drop rolling study to double emulsion drop case [15].

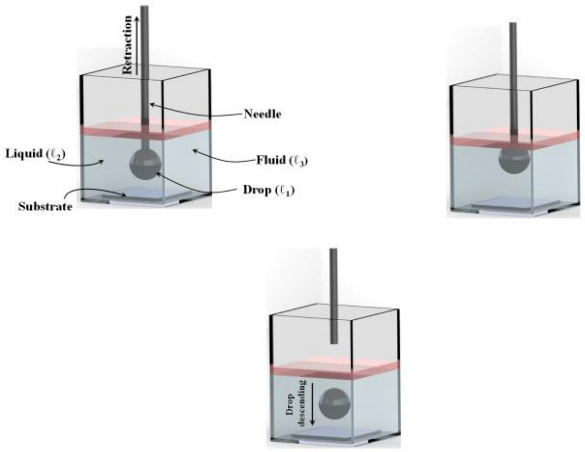

Figure 2: Needle less deposition of a single phase drop in a medium (a) first a drop is generated inside a liquid bath and a film is created at the interface (b) needle containing the drop at its tip is retracted through the film (c) as soon as the drop hits the liquid-film, it detaches and falls to the substrate underneath the bath (Adapted from Ref. [32] with permission of The Royal Society of Chemistry).

3. SPREADING AT THE INTERFACE

The dynamics of droplet spreading on solid substrates is a classical moving boundary problem in fluid mechanics that has long been studied for complete and partial wetting scenario [36–42]. The interfacial and viscous forces determine

the spreading rate of small viscous drops and this temporal evolution often follows Tanner's law [38, 43, 44]. In case of lower contact angle case, the spreading of the bulk drop is indeed preceded by the progression of a pre-cursor that justifies the universality of the Tanner's law [45–47]. However, a wide range of variation in the exponents for this law can be attributed to the liquid and solid properties [35, 48–51] and wetting scenario such as partial [52] and electro-wetting [53] Spreading starts immediately as the drop detaches from the needle at the interface. Within a few milliseconds contact angle reaches a minimum value and a precursor footing becomes visible. Unlike spreading on a rigid substrate, in case of spreading on a liquid fluid interface, the vertical interfacial force component on the three phase contact line assists the deformation of the underlying interface. At the same time, drop spreads along the horizontal direction. The competition between the horizontal and vertical force components results in the appearance of two angles, θc and θcap. These two angles as well as the drop height are schematically shown in Fig. 3(a). The short time dynamics of drop spreading on a liquid fluid interface exhibits similar behavior as that of the rigid wall case. This suggests the independent nature of the early spreading dynamics from the interface characteristics. A detailed discussion on this study can be found in Ref. [16].

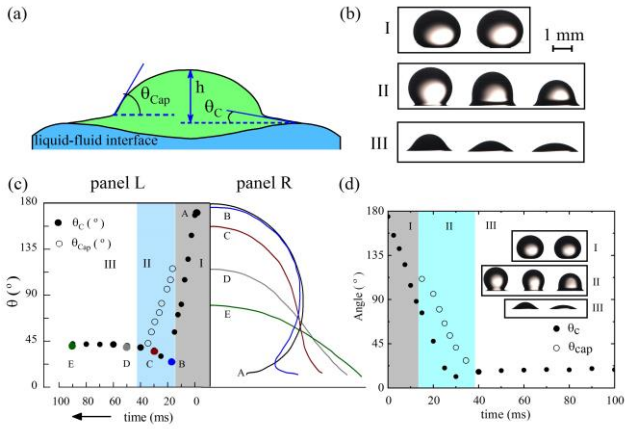

Figure 3: Transient spreading of a droplet on water-air interface: (a) Schematic diagram of the drop spreading with an underlying precursor footing which allows the definition of a two angles, cap angle θcap and contact angle θc (b) Different stages of silicon (S60) droplet spreading on the interface (c) Drop profiles (A−E) depict the shape evolution and corresponding transient variations in θc and θcap (d) temporal variation of θc and θcap for a more viscous drop (laser liquid). (Figure adapted from Rahman et al's published work [16])

4. DOUBLE EMULSION DROP ROLLING UNDER VISCOUS MEDIUM

For a soft body, i.e., liquid drop rolling under viscous medium, balancing the major contributing forces, one can obtain the expression for drop velocity as:

$$U \sim \frac{Bo\ \sigma sin\alpha}{\mu_d Bo^{\frac{3}{2}} + 6\pi\mu_m} \quad (1)$$

Here, σ is the interfacial tension of the drop in the considered medium and Bond number (Bo = gR2Δρ/σ). For a detail derivation of this equation, readers are referred to Rahman and Waghmare [15] In order to analyse double drop motion behaviour in a viscous medium, κR needs to be significantly larger. But achieving a drop of this radius is restricted by the spherical shape assumption. In this case, to retain a spherical shape, a drop radius must be smaller than ∼1.9 mm; larger drops undergo too much deformation. For highly viscous medium (i.e., μR ∼ 0.1) this size is too big to attain. Contrastingly, in a medium with low viscosity, (i.e., μR ∼ 104) the drop size is too small to avoid the sticking threshold. These limitations impose restrictions for performing the experimental analysis with the considered combinations of drop and medium. Therefore, we have carefully engineered the experiments to overcome this barrier so that we might still observe Regime II. If κR of the drop can be increased above κRcr without altering the drop size (so that its spherical shape is not deformed), exploration of Regime II becomes easier. The apparent dilemma between size and deformation can be easily solved by instilling a denser and immiscible liquid drop inside the rolling drop. This allows us to observe the rolling of a double emulsion drop consisting of both inner and outer drop phases. This not only facilitates the demonstration of the contrasting velocity behaviours, also it widens the degree of freedom for the selection of liquids for experimentation. We introduced denser inner droplets of varied radii into the outer drops in such a way that the overall drop radius remained constant.

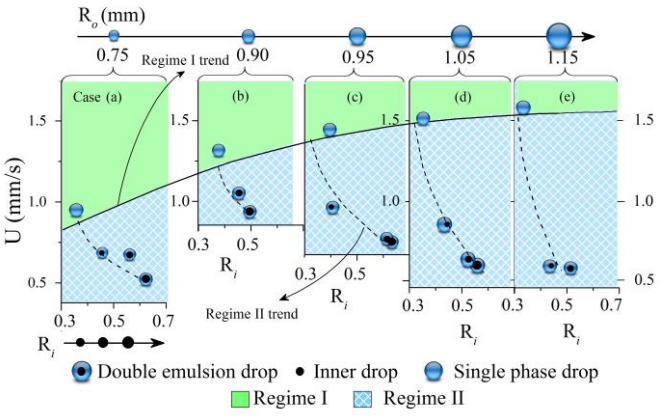

Figure 4: Occurrence of both regimes for drop descent with double-emulsion drop on a 3° incline. The increment in velocity with increase in size. As presented in the hatched areas of Cases (a)-(e), Regime II behavior (decrements in the velocity) is observed with an increment in the dissipation by inserting an inner drop for a fixed outer drop size. Symbols are experimental results while the dashed and solid lines denote the velocity trend observed from the experimental data. (Adapted from the Rahman et al's published work [15].)

We have termed the set of experiments with one fixed drop radius as one 'case' in Fig. 4. Thus cases (a) - (e) in Fig. 4 denote five different sets of experiments where the inner drop size is altered, maintaining a fixed overall double drop size for each particular case. For a fixed double drop size, introducing a denser inner drop increases κR of the droplet without altering the shape and the overall drop size. Thus the Stokes outer bulk dissipation remains the same for each case but the increment of κR causes further dissipation. For a constant overall drop size, the dominant dissipation, at the contact area, results in the decrease in velocity with the increase in κR as commonly observed. The dashed lines connecting the experimental data in Fig. 4 highlight the Regime II, while the solid line shows the increasing trend (Regime I) of the data points. It is worth considering the role of the newly introduced interface between the outer and inner drop. Relative motion between the inner and outer drop along this interface might invite an additional internal dissipation in addition to the dissipation that occurs in the vicinity of the contact area. The viscous dissipation near the contact area scales as the fourth exponent of the characteristic radius; similarly, the additional viscous dissipation due to the relative motion at the new interface, should also scale with the same exponent of the characteristic length scale such that it scales as $\sim Ri^4$. It is plausible that this dissipation also accounts for the decrements in velocity as the area of the interface is increased with increasing inner drop radius. The rational for scaling argument for this dissipation is from the understanding of viscous dissipation near the contact area of drop. Exact quantification of this dissipation requires further investigations in detail.

5. CONCLUSION

The first fundamental aspect studied here is spreading and Chapter 2 discusses the early time drop spreading on a liquid-fluid interface. Unlike spreading on solid substrate, a drop deforms at three phase contact line (TPCL) as it spreads on a liquid-fluid interface. Present observations strongly suggest the short time dynamics to be independent of the interface property. Quite interestingly, spreading shows a logarithmic response rather than the classical power law. With the understanding of the drop behavior at the interface and mastering the detachment technique, rolling dynamics is studied in detail, where scaling analysis with experimental evidences demonstrate that in creeping flow, medium viscosity significantly alters the descent speed of a drop and its dependency on drop size. In a viscous medium, while a descending drop that rolls on an incline, may travel with either increasing or decreasing velocities as its size increases. This has never been established before with a unified theory and experiments. Theoretical understandings of the role of medium viscosity allow us to establish the criteria to define these two contrasting behaviors. The transition from one to the other behavior strongly depends on the drop and medium viscosity. For a single phase drop, it is practically very difficult, if not impossible, to engineer such a drop that can demonstrate both the increasing and decreasing behaviors. The double emulsion drop provided a feasible solution due to its compound nature. Understanding the dynamics of such multiphase droplets allows superior control over the transformation from one to the other velocity behavior.

6. REFERENCES

[1] Misuk, V.; Mai, A.; Giannopoulos, K.; Alobaid, F.; Epple, B.; Loewe, H. Lab on a Chip 2013,13, 4542–4548.
[2] Sciambi, A.; Abate, A. R. Biomicrofluidics 2013, 7, 044112.
[3] Dolgin, E. Encapsulate this. 2014.
[4] Zhao, X.; Kim, J.; Cezar, C. A.; Huebsch, N.; Lee, K.; Bouhadir, K.; Mooney, D. J. Proceedings of the National Academy of Sciences 2011, 108, 67–72.
[5] Charve, J.; Reineccius, G. A. Journal of agricultural and food chemistry 2009, 57, 2486–2492.
[6] Kim, S.-H.; Kim, J. W.; Cho, J.-C.; Weitz, D. A. Lab on a Chip 2011, 11, 3162–3166.
[7] Song, H.; Tice, J. D.; Ismagilov, R. F. Angewandte Chemie International Edition 2003, 115,792–796.
[8] Okushima, S.; Nisisako, T.; Torii, T.; Higuchi, T. Langmuir 2004, 20, 9905–9908.
[9] Chang, C. B.; Wilking, J. N.; Kim, S.-H.; Shum, H. C.; Weitz, D. A. Small 2015, 11, 3954–3961.
[10] Ren, P.-W.; Ju, X.-J.; Xie, R.; Chu, L.-Y. Journal of Colloid and Interface Science 2010, 343,392–395.
[11] Zhang, H.; Tumarkin, E.; Peerani, R.; Nie, Z.; Sullan, R. M. A.; Walker, G. C.; Kumacheva, E.Journal of the American Chemical Society 2006, 128, 12205–12210.
[12] Wu, A.; Yu, L.; Li, Z.; Yang, H.; Wang, E. Analytical Biochemistry 2004, 325, 293–300.
[13] Dugas, V.; Broutin, J.; Souteyrand, E. Langmuir 2005, 21, 9130–9136.
[14] Iqbal, M.; Zafar, N.; Fessi, H.; Elaissari, A. International journal of pharmaceutics 2015,496, 173–190.
[15] Rahman, M. R.; Waghmare, P. R. Physical Review Fluids 2018, 3, 023601.
[16] Rahman, M. R.; Mullagura, H. N.; Kattemalalawadi, B.; Waghmare, P. R. Colloids and Surfaces A: Physicochemical and Engineering Aspects 2018, 553, 143–148.
[17] Muschiolik, G.; Dickinson, E. Comprehensive Reviews in Food Science and Food Safety 2017, 16, 532–555.
[18] Bernewitz, R.; Schmidt, U.; Schuchmann, H.; Guthausen, G. Colloids and Surfaces A: Physicochemical and Engineering Aspects 2014, 458, 10–18.
[19] Scherze, I.; Marzilger, K.; Muschiolik, G. Colloids and Surfaces B: Biointerfaces 1999, 12,213–221.
[20] Jiménez-Alvarado, R.; Beristain, C.; Medina-Torres, L.; Román-Guerrero, A.; Vernon-Carter, E. Food Hydrocolloids 2009, 23, 2425–2433.
[21] Li, B.; Jiang, Y.; Liu, F.; Chai, Z.; Li, Y.; Leng, X. International journal of food engineering 2011, 7.
[22] Tang, S. Y.; Sivakumar, M. Asia-Pacific Journal of Chemical Engineering 2012, 7.
[23] Aditya, N.; Aditya, S.; Yang, H.; Kim, H. W.; Park, S. O.; Ko, S. Food chemistry 2015, 173,7–13.
[24] Scherze, I.; Knöfel, R.; Muschiolik, G. Food Hydrocolloids 2005, 19, 617–624.
[25] Khalid, N.; Kobayashi, I.; Neves, M. A.; Uemura, K.; Nakajima, M.; Nabetani, H. Colloids and Surfaces A: Physicochemical and Engineering Aspects 2014, 458, 69–77.
[26] Schroën, K.; Bliznyuk, O.; Muijlwijk, K.; Sahin, S.; Berton-Carabin, C. C. Current Opinion in Food Science 2015, 3, 33–40.
[27] Akhtar, M.; Dickinson, E. Food Colloids: fundamentals

of formulation. Cambrige: The Royal Society of Chemistry 2001, 133–143.
[28] Burgaud, I.; Dickinson, E.; Nelson, P. International journal of food science & technology 1990, 25, 39–46.
[29] Hemar, Y.; Cheng, L. J.; Oliver, C. M.; Sanguansri, L.; Augustin, M. Food Biophysics 2010, 5, 120–127.
[30] Cofrades, S.; Antoniou, I.; Solas, M.; Herrero, A.; Jiménez-Colmenero, F. Food chemistry 2013, 141, 338–346.
[31] Xiang, J.; Liu, F.; Fan, R.; Gao, Y. Colloids and Surfaces A: Physicochemical and Engineering Aspects 2015, 487, 104–112.
[32] Waghmare, P. R.; Das, S.; Mitra, S. K. Soft Matter 2013, 9, 7437–7447.
[33] Waghmare, P. R.; Mitra, S.; Gunda, N. S. K.; Mitra, S. K. RSC Advances 2015, 5, 82374–82380.
[34] Neumann, F. E. Vorlesungen über mathematische Physik: Vorlesungen über die Theorie der Capillarität; BG Teubner, 1894; Vol. 7.
[35] De Gennes, P.-G.; Brochard-Wyart, F.; Quéré, D. Capillarity and wetting phenomena: drops, bubbles, pearls, waves; Springer Science & Business Media, 2013.
[36] Young, T. Philosophical Transactions of the Royal Society of London 1805, 95, 65–87.
[37] Brochard-Wyart, F.; De Gennes, P. Advances in colloid and interface science 1992, 39, 1–11.
[38] Tanner, L. Journal of Physics D: Applied Physics 1979, 12, 1473.
[39] Huppert, H. E. Journal of Fluid Mechanics 1982, 121, 43–58.
[40] De Ruijter, M. J.; De Coninck, J.; Oshanin, G. Langmuir 1999, 15, 2209–2216.
[41] Haley, P. J.; Miksis, M. J. Journal of Fluid Mechanics 1991, 223, 57–81.
[42] Leger, L.; Joanny, J. Reports on Progress in Physics 1992, 55, 431.
[43] Garnier, G.; Bertin, M.; Smrckova, M. Langmuir 1999, 15, 7863–7869.
[44] Milchev, A.; Binder, K. The Journal of chemical physics 2002, 116, 7691–7694.
[45] Cormier, S. L.; McGraw, J. D.; Salez, T.; Raphaël, E.; Dalnoki-Veress, K. Physical review letters 2012, 109, 154501.
[46] Leger, L.; Erman, M.; Guinet-Picard, A.; Ausserre, D.; Strazielle, C. Physical review letters1988, 60, 2390.
[47] Ausserré, D.; Picard, A.; Léger, L. Physical review letters 1986, 57, 2671.
[48] Gu, Y.; Li, D. Colloids and Surfaces A: Physicochemical and Engineering Aspects 1998, 142, 243–256.
[49] Bonn, D.; Eggers, J.; Indekeu, J.; Meunier, J.; Rolley, E. Reviews of modern physics 2009,81, 739.
[50] Ma, C.; Bai, S.; Peng, X.; Meng, Y. Applied Surface Science 2014, 311, 789–792.
[51] Savva, N.; Kalliadasis, S.; Pavliotis, G. A. Physical review letters 2010, 104, 084501.
[52] Bird, J. C.; Mandre, S.; Stone, H. A. Physical review letters 2008, 100, 234501.
[53] McHale, G.; Brown, C.; Sampara, N. Nature communications 2013, 4, 1605.

EFFECT OF SOUTH ASIAN ROAD TRUCKS ON ENERGY EFFICIENCY AND SAFETY

Firoz Alam[1], Harun Chowdhury[1,*], Anirban Basu[1], Rashid Sarkar[2], AkshoyRanjan Paul[3], Somnath Chattopadhyaya[4]

[1]School of Aerospace, Mechanical and Manufacturing Engineering, RMIT University, Melbourne, Australia
[2]Department of Mechanical Engineering, Bangladesh University of Engineering and Technology, Dhaka, Bangladesh
[3]Department of Applied Mechanics, Motilal Nehru National Institute of Technology (MNNIT) Allahabad, India
[4]Department of Mechanical Engineering, Indian Institute of Technology (IIT) Dhanbad, India
*Corresponding author's email: harun.chowdhury@rmit.edu.au

Abstract: *Road vehicles especially trucks play vital role in freight delivery and compete well with other surface transport. In South Asia, light and medium sized trucks are the backbone of road transport and typically box shape. These locally manufactured trucks have minimum or no consideration of aerodynamics, safety (crashworthiness) and environmental impact. Hence, the main purpose of this study is to analyse the aerodynamic aspect of light and medium sized trucks widely used in South Asia (India, Bangladesh and Pakistan). The study is to be conducted by computer modelling, manufacturing of physical prototype models and wind tunnel testing. Additionally, the study highlights the safety issues related to light and medium sized trucks whose bodies are built mainly by road side vehicle body builders. The major finding of this study indicates that minor modification to body design can reduce aerodynamic drag (resistance) of light and medium sized trucks nearly one-third. This reduction of drag will lower not only the consumption of fossil fuel but also the greenhouse gas emission.*

Key Words: *Aerodynamics, trucks, road-side builders, crashworthiness, greenhouse gas, road safety standards*

1. INTRODUCTION

Freight movement by commercial vehicle especially trucks is growing fast in South Asia surpassing the railways due to increased investment in road infrastructures and improved payload capacity. Moreover, trucks can deliver goods door to door and regions inaccessible by railways. The fuel consumption and escalating fuel price are progressively reducing the profit margin of truck operators. However, the fuel consumption is directly related to the aerodynamic efficiency of the truck's physical shape while the rolling resistance depends on the weight of the truck [1-8]. Additionally, with the increase of the speed, the aerodynamic resistance increases exponentially. Most aerodynamic resistance (drag) is generated by the frontal shape of the truck where the moving airflow hits the front faces of the cab and the trailer. It is estimated that almost 70% of the total drag is exerted on these forward faces, with the remainder 30% coming from the back and the sides due to the complex flow pattern (e.g., a combination of separation, reattachment and vortices) [3-9]. For a typical long-distance articulated truck at a steady head wind velocity of 80 km/h, nearly 50% of the consumed fuel is used to overcome aerodynamic drag. As velocity increases, the drag also increases. Drag (F_D) and power (P) required to overcome the aerodynamic drag and other resistances are shown in equations (1) & (2).

$$P = F_D.V + RR.V + Aux\ P \quad (1)$$

$$P = 0.5\ C_D.\rho.\ 3 + RR.V + Aux\ P \quad (2)$$

Equation (2) means: Power = aerodynamic power + rolling resistance power + auxiliary power.
Where, C_D, ρ, V, A, RR, Aux P are the drag coefficient, air density, velocity, projected frontal area of the truck, rolling resistance and auxiliary power respectively. A decisive factor is the aerodynamic quality of the vehicle shape, the drag coefficient, C_D. Unlike normal passenger car, commercial vehicles especially trucks are aerodynamically inefficient because of their un-streamlined body shape [1-9]. The average drag coefficient (a measure of aerodynamic efficiency, higher the drag coefficient, lower the aerodynamic efficiency and higher fuel consumption) and power required to overcome aerodynamic resistance, rolling resistance and auxiliary losses for typical road vehicles is shown in Fig. 1 and Fig. 2 [8-11].

When travelling on the highway with around 90 to 100 km/h speed, a 40-ton truck is estimated to consume around 40 litre of fuel. This amount of fuel is required four and half times more than a passenger car. Aerodynamic drag with a small and medium

sized truck typically accounts for about 75 - 80% of the total resistance to motion at 100 km/h [1, 10-13]. Therefore, reducing aerodynamic drag contributes significantly to the fuel economy as well as the reduction of greenhouse gas emissions (less CO_2 and other health hazard matters). Any extra add-ons such as front deflectors of the truck can increase the fuel consumption to a significant amount if it is not aerodynamically efficient [10-13].

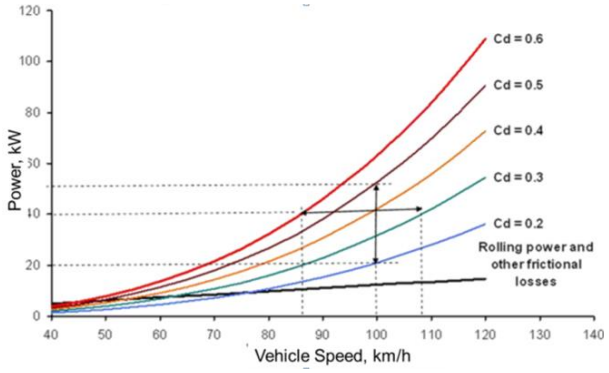

Figure 1: Power requirement as a function of vehicle speeds, adapted from [8-9]

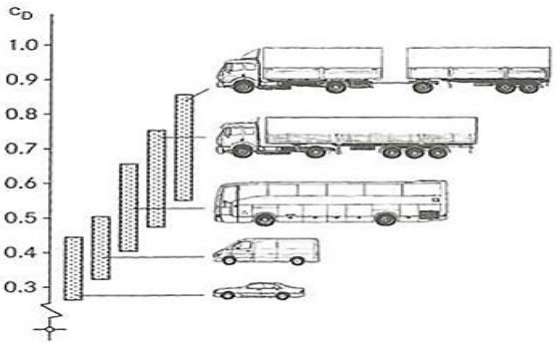

Figure 2: Drag coefficient of different vehicles type, adapted from [1]

In the Indian subcontinent, especially in Bangladesh, India and Pakistan, there is a significant number of light and medium sized trucks operational of which cabs and cargo bodies are made by the road side builders as a rigid structure (Fig. 3). It can be seen alongside the vast expand of Indian, Bangladesh and Pakistan highways, road side body building is the most proffered one to bring the commercial vehicle underplay. Due to lenient or no government regulations most commercial vehicle manufactures offer "cowl & chassis" combination, which means an incomplete vehicle, with the fitment of a front end structure with or without the windshield, that requires the building of the complete cab and the cargo carrying or load bearing components to perform its intended purpose. Manufactures like TATA Motors, Ashok Leyland, AMW and EicherMotors offer both cowl chassis and cab chassis combination as shown in Fig. 4.

Figure 3: Road side builders-made complete truck body-cabins in South Asia, adapted from [12]

Figure 4: Cowl and chassis (incomplete truck body), adapted from [23-25]

Most light and medium sized trucks in Bangladesh, India and Pakistan are built and modified according to the owner's and road side builder's wishes. Usually the ornament (add-on) attached to the truck shows some combination of epigraphic formulae, poetry, repetitive patterns and figural images [12]. Subsequently, more the ornaments attached to the truck will reflect the wealthier of the owner (general perception). The modified truck is also called "jingle truck" as it produces noise when travels due to the chain tassels that are hanging on the front bumper of the truck. This type of trucks is widely found on the highways of South Asia as shown in Fig. 3.

The main problem of this road side modified truck is not only unsafe (in case of crash) but also aerodynamically inefficient and greenhouse gas intensive. In addition to box shape cabin (frontal area), the attached ornaments also increase the aerodynamic drag, thereby increase further fuel consumption. Therefore, the reduction of the aerodynamic drag is so important that only few percent reduction will contribute to fuel saving and less greenhouse gas emission. At RMIT University, a series of experimental and computational study was undertaken to quantify the drag generated by representative truck body shapes made and operated

in developing countries especially in India, Bangladesh and Pakistan. In this paper, our focus is on aerodynamics as well as safety aspects of light and medium sized trucks commonly used in South Asia.

2. AERODYNAMICS STUDY

A one-tenth scale simplified model of a Bedford truck was used as a baseline truck to fit in the test section of RMIT Industrial Wind Tunnel. Two deflectors were also manufactured replicating the design of Indian/Bangladeshi and Pakistani trucks. Additionally, an aerodynamic shaped deflector was developed to minimise drag force while attached to the baseline truck model. All the model deflectors were made one-tenth of their full size to fit with the baseline truck model. Fig. 5 shows the baseline truck fitted with 3 different deflectors.

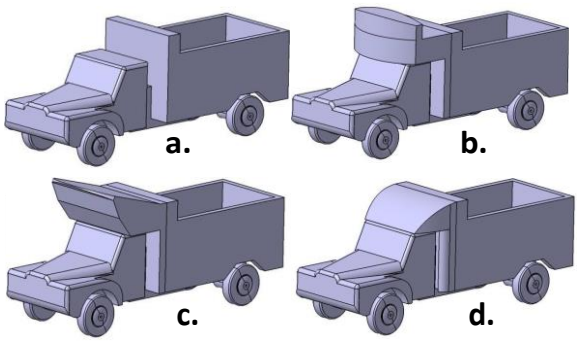

Figure 5: Baseline truck fitted with deflector: (a) Base model truck (b) India/Bangladesh model truck, (c) Pakistan model truck and (c) Aerodynamic model truck

The model trucks were investigated experimentally in RMIT Industrial Wind Tunnel. The tunnel is a closed return circuit with a turntable to simulate the cross-wind effects. The maximum speed of the tunnel is approximately 145 km/h. The rectangular test section dimensions are 3 meters wide, 2 meters high and 9 meters long, and the tunnel's cross-sectional area is 6 square meters. More details of this wind tunnel can be found in [12].

The truck model was mounted through a support with the JR3 multi-axis load sensor made by JR3, Inc., USA. The sensor was used to measure all three forces (drag, lift and side forces) and three moments (yaw, pitch and roll) simultaneously. Fig. 6 shows the schematic of the experimental setup. For baseline comparison, initially, the aerodynamic forces were measured for the baseline truck without any external attachment (i.e., deflector) under a range of wind speeds (40 to 100 km/h) at 0º yaw angle. Then the measurements were taken by mounting the truck models (b, c & d). Each set of data was recorded for 10 seconds time average with a frequency of 20 Hz ensuring electrical interference is minimal. Multiple data sets were collected at each speed tested and the results were averaged for minimising the further possible errors in the raw experimental data. Experimental models inside the RMIT Industrial Wind Tunnel are shown in Fig. 7.

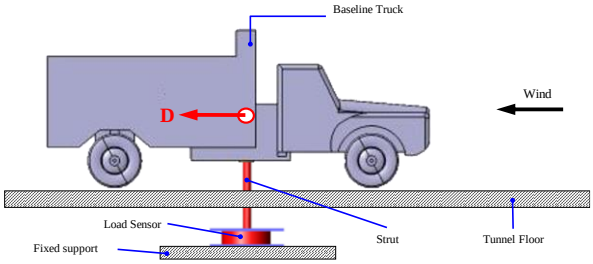

Figure 6: Schematic of the experimental setup

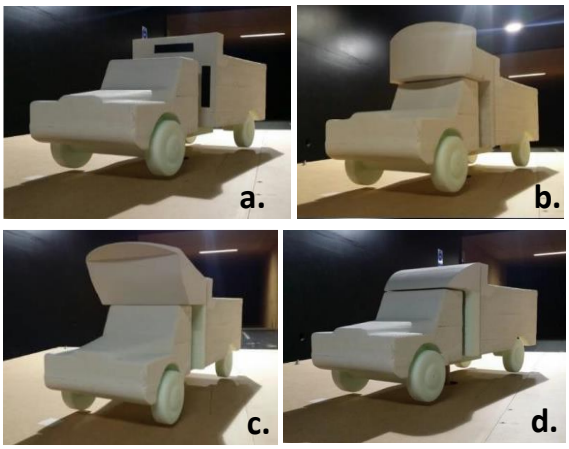

Figure 7: Experimental setup inside the RMIT Industrial Wind Tunnel test section. Baseline truck fitted with deflector: (a) Base model truck, (b) India/Bangladesh model truck, (c) Pakistan model truck, and (d) Aerodynamically modified model truck, adapted from [12]

The measured aerodynamic drag was converted to non-dimensional parameter drag coefficient C_D. The C_D values as a function of speed for various configurations of truck at 0º yaw angle are presented in Fig. 8. The result shows that the baseline truck has almost constant C_D value about 0.47. Similar results were found by Chowdhury at al. [11]. In this study, the C_D values of truck ranges between 0.41 and 0.51 depending on the aerodynamic design of the front deflector. The baseline truck with the aerodynamic deflector attached has the lowest C_D value among all other configurations tested.

In addition to experimental investigation, a Computational Fluid Dynamics (CFD) study was carried out to visualise the fluid flow structure around the models. Fig. 9 (a&b) illustrates velocity contours and velocity streamlines for the truck models with all configurations. It can be seen in the region closer to the rear section the vortices are very large and chaotic due to complex frontal shape. With vortices extending along the downstream, the

vortices gradually combine into a pair of vortices with contrary directional rotations and the intensity becomes weaker in the far downstream section.

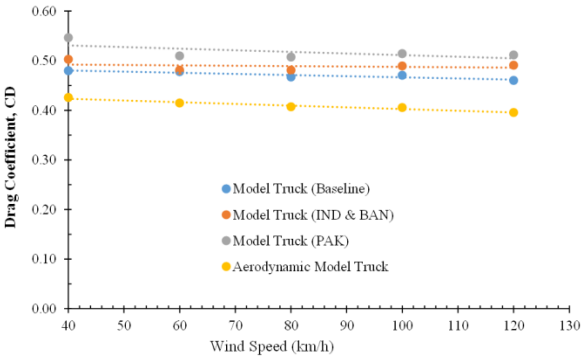

Figure 8: Drag coefficient (C_D) as a function of wind speed

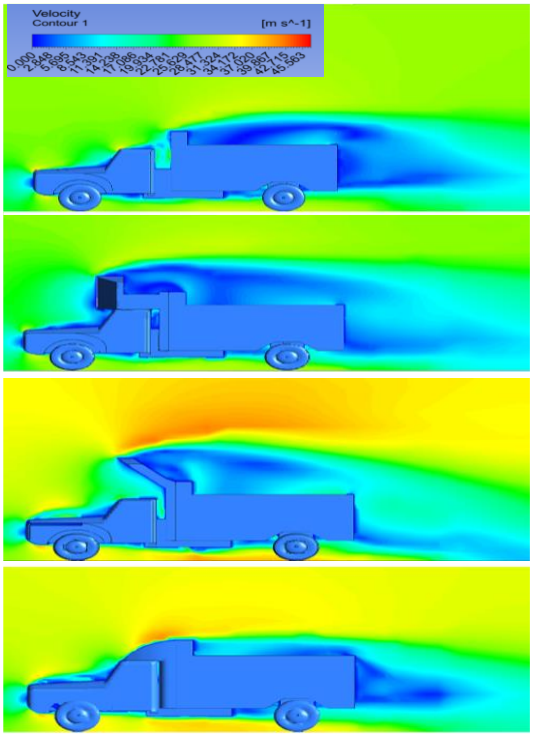

Figure 9(a): CFD post processing: velocity contour, adapted from [12]

A comparative aerodynamic drag increase and/or decrease (in percentage) with the base truck model is shown in Table 1. The Pakistan truck model has the highest aerodynamic drag followed by India/Bangladesh truck model. The aerodynamically modified model has the lowest drag compared to all model trucks including base model truck.

Table 1: Drag variation in percentage compared to baseline model 'a'

Configuration	Drag increase
Indian/Bangladesh Model	+14%
Pakistan Model	+22%
Slightly Streamlined Aerodynamic Model	-12%

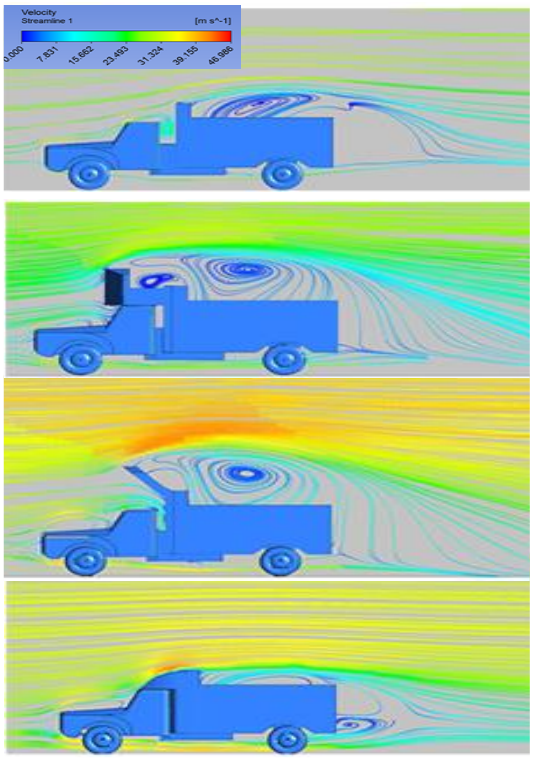

Figure 9(b): CFD post processing:velocity streamline, adapted from [12]

The increase of drag has direct impact on the fuel consumption. As the drag increases, the fuel consumption also increases [10-13]. Additionally, the non-aerodynamic design of trucks found in South Asia can also affect the directional stability as the vehicle's centre of gravity changes and the overall downforce is reduced due to the disturbance of the flow over the roof. Furthermore, the intricate external designs of the truck deflectors also contribute to wind noise and dirt deposition [12]. Because of increasing fuel consumption, the running cost will be higher and accelerated deterioration of air quality. Additionally, the increased fuel consumption creates extra pressure on national energy security. It may be noted that the world burnt over 1.3 trillion litres of petrol and diesel for powering hundreds of millions cars and trucks in 2009. The current figure will be much higher. Snyder [26] indicated that in the US if it was possible to reduce fuel consumption by as little as 1% (which typically equates to merely 0.1 litre/100 km for a standard car), the US$30 million could be saved annually. By reducing the aerodynamic drag, this figure can easily be achieved.

3. SAFETY ISSUE OF RIGID TRUCKS

As mentioned earlier, once owner gets the chassis with cowl it is delivered to the road side body builders to make the cabin and load body according to their needs/ wishes, where safety, driver's comfort, overall structural strength to absorb the crash energy and all around visibility are vastly neglected. However, local truck manufacturers (Tata,

Ashok Leyland, Eicher India) also offer complete cab and chassis combination, where load body is meant to be built with certain regulation and clearance as per some safety standards. The road side body builders are not often aware of those safety issues and standards. These gross negligence and incompliance of motor vehicle safety issues contribute serious fatal crashes and driver discomfort and fatigue. In Fig. 10, it is shown how truck bodies are made in South Asia without considering structural strength (crashworthiness), aerodynamics and ergonomic issues. Some fatal crashes in South Asia (Bangladesh, India and Pakistan) are shown in Fig. 11.

Figure 10: Road side truck body and cab building in India

Rigid body trucks manufactured by road side builders have poorly design driver cabins which have no or minimum vibration absorber from engine and road input. Prolong exposure to vibration, noise, thermal comfort (no air conditioning) and excessive working hour are the main causes to driver fatigue [16]. The combination of driver fatigue, poorly designed cab for visibility and faulty road design are believed to be the main reasons of fatal crash/accidents as shown in Fig. 11. The degree of fatality is expected to be higher if there is no room to absorb the energy when collision occurs.

Generally, automobiles including trucks should have a) vehicle structure to maintain its integrity and provide adequate protection in survivable crash, b) interiors for adequate space to comfortably accommodate its occupants, c) external shape to minimise aerodynamic drag, d) vehicle body with the suspension to minimise road vibrations and aerodynamic noise transfer. The vehicle must have crashworthiness - a measure of the ability of a structure and any of its components to protect the occupants in survivable crash. Crashworthiness indicates a measure of the vehicle's structural ability to plastically deform and yet maintain a sufficient survival space for its occupants in crashes involving reasonable deceleration loads.

Figure 11: Crashed truck cabins have no means to absorb impact (India, Bangladesh & Pakistan)

Restraint systems (active –seat belt and passive-airbag) and occupant packaging provide additional protection to reduce severe injuries and fatalities. Therefore, the main objectives of crashworthiness are: i) vehicle body structures include progressive crush zones to absorb part of the crash kinetic energy, ii) vehicles maintain integrity of the passenger/ driver compartment and simultaneously control the crash deceleration pulse, iii) vehicle crashworthiness must be evaluated in four distinct modes: frontal, side, rear and rollover crashes, and iv) accident reconstruction and analysis of vehicle crashes should provide information regarding the safety performance. Unfortunately, most road side truck body builders do not pay attention to these crashworthiness and other safety and aerodynamic issues while building truck bodies.

Major truck manufacturers including Indian subsidiary of Volvo, Bharat Benz (a subsidiary of Daimler India Commercial Vehicle and Daimler AG) offer fully built cabin and cab with integrated structure to enhance safety, reasonable comfort with better visibility to reduce fatigue stress of driver as well as severity of crashes as shown in Fig. 12. Aerodynamically efficient and ergonomic cab design with structural strength and crashworthiness can be possible in South Asia if all truck manufacturers/ road side truck body builders comply with the national motor vehicle safety standards. Unfortunately, the adoption and/ or implementation of motor vehicle safety regime is lenient in South Asia. The authorities in South Asia (India, Bangladesh, Pakistan should have banned cowl chassis truck option long time ago and only permit fully built cabin truck option equipped with all safety features.

Figure 12: Fully integrated cabin-cab safety compliant truck as offered by BharatBenz, adapted from [27]

Tables 2 & 3 show the number of fatal accidents, deaths and serious injuries in Bangladesh and India. By any measure these numbers are extremely high and such number of deaths in peace time is unacceptable. The economic, moral and social losses are colossal (nearly 2% to 3% of national GDP). The road accident data is not openly available for Pakistan. However, widely circulated newspapers such as Daily Dawn [21] and The Nation [22] reported that over 36,000 people in 2018 and 27,000 people in 2017 died in road accidents in Pakistan. Data shows that nearly one-third (33.33%) accidents occurred due to head on collisions between vehicles during illegal overtaking. As the number of vehicles is rising, the number of fatalities will grow rapidly unless vehicle safety standards are introduced.

A study undertaken by Singh [28] revealed that drivers' fault constitutes over 70% of all motor vehicle accidents in India in 2013. This data is representative for motor vehicle accidents occurred in Bangladesh and Pakistan. The overspeed, overload, overtime, alcohol/ illicit drag are considered to be the main reasons for driver's fault accident. However, the vehicle design faults, design fault led to driver fatigues and faulty road designs are mostly ignored in road vehicle accident investigations in South Asia. Unfortunately, most fatal accident investigations are generally undertaken without involving traffic collision technical experts. For example, in Australia, any motor vehicle accident involved fatality is investigated by major collision (vehicle forensic investigation) unit(s) generally consisting of engineers in police uniform. Apart from collecting medical and post-mortem reports, the major collision unit undertakes vehicle examinations, crash reconstructions, pharmacology, and driver's fatigue profiles. The Major Collision Unit also has highly specialised unit called Vehicle Investigation Unit (VIU). The VIU conducts investigation and examination of vehicles involved in serious or fatal crashes. The unit helps determine whether a vehicle's mechanical condition was a contributing factor in the cause of a fatal or serious crash. They also prepare and present expert evidence in court on their findings. The VIU prepares a full report on the vehicle's condition and highlights what may have contributed to the cause of the crash. If they find a pattern of crash (five or more) due to the same safety features of a similar model vehicle, can initiate vehicle recall (either voluntarily by the manufacturer/ dealers and /or forced recall if the manufacturer/ dealer did not act upon the VIU advice.

Table 2: Accident data for Bangladesh, adapted from [14-15,19-20]

Year	No. of Accidents	No. of Deaths	No. of Injured
2018	5,514	7,221	15,446
2017	4,979	7,397	16,193
2016	4,312	6,055	15,914
2015	6,581	8,642	21,855

Table 3: Accident data for India, adapted from [16-17]

Year	No. of Accidents	No. of Deaths	No. of Injured
2018	Data Not Available Yet	-	-
2017	464,910	147,913	1470,975
2016	480,652	150,785	494,624
2015	501,423	146,133	500,279

4. NATIONAL STANDARDS FOR MOTOR VEHICLE SAFETY

South Asian nations must adopt or develop National Standards for Motor Vehicle Safety and Emission Control. For safe vehicle manufacturing, registration, operations, repair and maintenance, the National Standards for Motor Vehicle Safety is vital. For example, Australia developed its national standards for motor vehicle safety immediately after the Second World War. The Australian Design Rules (ADRs) are national standards for vehicle safety, anti-theft and emissions which are administered by the Australian government under the Motor Vehicle Standards Act 1989. The current ADRs are the 3rd revision while the 2nd revision was effective from 1 January 1969 till 31 December 1988. The 1989 Act requires all road vehicles, whether they are newly manufactured in Australia or are imported as new or second hand vehicles, to comply with the relevant ADRs at the time of manufacture and supply to the Australian market. When a road vehicle (any motorised vehicle) is first used on Australian roads the relevant state or territory government's legislation requires that it continue to comply with the relevant ADRs as at the time of manufacture. The ADRs are performance based and cover issues such as occupant protection, structures, lighting, noise, engine exhaust emissions, braking (brake pads & brake lights), windscreen-tempered & scratch less, wiper, indicator lights, tyre thread, etc.). Any vehicles not comply

with ADRs are completely unfit to ply on Australian roads and they are banned to operate [18]. The similar standards are also effective in all developed nations including Canada, USA, UK, New Zealand, European Union, former Soviet Union (Russia and other 14 Republics), Japan, South Korea, Hong Kong, Taiwan, South Africa, and Singapore.

As mentioned earlier, a road vehicle can be registered for the first time in Australia only if it must meet the requirements of the Motor Vehicle Standards Act 1989, which applies to new and used imported vehicles and locally manufactured vehicles. When a new vehicle has been certified as meeting the ADRs it can be fitted with an identification plate. The fitment of an identification plate is mandatory under the Act, and it indicates to the registering authority that the vehicle meets all the required ADRs. Vehicle manufacturers and/or importers must have Vehicle Certification to obtain approval to fit an identification plate. The Vehicle Safety Standards (VSS) branch within the Department (Ministry) of Infrastructure, Regional Development and Cities administers certification in Australia, while State and Territory registering authorities administer the use of vehicles, roadworthiness and approval of modifications for vehicles in service [18].

The certification system for new vehicles is based on type approval, wherein a vehicle design representing a make-model (the "type" of vehicle) undergoes tests to demonstrate compliance with the applicable ADRs (Australian Design Rules). If the test vehicle(s) complies then all others of the same design, or type, will also comply, provided the production processes are properly controlled. The VSS does not test vehicles for certification purposes. The manufacturer is responsible for ensuring compliance with the ADRs. The Australian certification process allows the vehicle manufacturer ('the Licensee') to conduct the various ADR tests. The tests may be conducted in a place convenient to the manufacturer provided they are done correctly. In order to demonstrate compliance with all the applicable ADRs, several test vehicles may be required, particularly for passenger cars and light commercial vehicles. Once the tests are successfully completed, the manufacturer may seek approval to fit identification plates to the vehicles by submitting an application for approval. The manufacturer must support its application with a summary of the evidence to show that all tests were done correctly and that the vehicle complies with the applicable ADRs. For some vehicle categories, a sample of each of the model variants must be made available for inspection. This inspection also satisfies the registration inspection requirements of the States and Territory registration authorities for new vehicles and is called a Single Uniform Type Inspection or SUTI [18]. When VSS is satisfied that the vehicle complies, the Administrator of Vehicle Standards issues a document known as an Identification Plate Approval. This is the authority for the manufacturer to fit identification plates to vehicles of the approved make-model and supply the vehicles to the market. The information provided by the manufacturer is subject to checking using quality assurance audits of the manufacturing facilities and inspection of the test facilities. Together these ensure the vehicles (or parts of vehicles) were built to the approved design and that all tests were done correctly. Manufacturers that supply limited numbers of vehicles may be able to use the Low Volume Scheme for new vehicles, which caters for manufacturers that supply less than 25 or 100 vehicles per year, depending on the category. The Registered Automotive Workshop Scheme applies to used-imported vehicles. Vehicles imported into Australia by individuals, or for racing, etc. may be able to use the Imported Vehicles scheme. Individually constructed vehicles are not required to be certified. However, they must meet the requirements of the State and Territory registering authorities [18].

5. CONCLUSIONS AND RECOMMENDATIONS

In this study, we highlighted aerodynamics, vehicle safety and motor vehicle design standards. Following conclusions and recommendations are made from the work presented here:

Aerodynamics: Most light and medium sized trucks are manufactured in South Asia without any consideration of trucks' aerodynamic aspect. Hence, these vehicles have high aerodynamic drag and fuel consumption resulting in higher greenhouse gas emission. Moreover, many cosmetic add-ons are attached to trucks that also create additional drag and fuel consumption. Our study indicates that a small modification with negligible cost to existing frontal shape of light and medium sized trucks can reduce aerodynamic drag over one-third (33%). This reduction will not only save fuel consumption but also reduce significant amount of greenhouse gas emission and increase operation-profit margin.

National Standards for Motor Vehicle Safety: South Asian countries must have national standards for motor vehicle safety (design rules). All established truck manufacturers and road side truck body

encourage truck manufacturers to sell complete factory-made trucks instead of cowl chassis trucks. In the long run, it will benefit all stakeholders including the truck owners/ operators both economically, environmentally and technically.

Technical Training/Education for Road Side Vehicle/ Truck Body Builders: In India, Bangladesh and Pakistan, there are several hundred thousand road side truck body builders employing many more people. Most of these people generally do not have formal technical education apart from apprentice knowledge. Upskilling these people through technical training programs (technical short courses, industrial placement at truck manufacturing/assembly plants, technical workshops, etc.) will have enormous impact on their quality of work, truck body building, design rules, and aerodynamics aspects.

Accident Investigation: Most accidents are occurred due to drivers' fault in Indian subcontinent (South Asia). Although overspeed, overtime, alcohol and drugs are the main causes of drivers' fault, we strongly urge the authorities to investigate vehicle mechanical design and road design standards compliance in fatal accidents/crashes. This type of investigations must be undertaken by technical expert specializing in vehicle forensic investigation as per the practices in all developed nations and many developing countries.

6. ACKNOWLEDGMENTS

The authors are highly grateful to Dr Bavin Raj Loganathan, Mr Raymond Juwono, Mr Mohamed Zaid and Mr Rezaul Islam, School of Aerospace, Mechanical and Manufacturing Engineering, RMIT University, Melbourne, Australia for their assistance with the wind tunnel data acquisition and computational modeling. The technical assistance provided by Mr Gil Atkins, School of Aerospace, Mechanical and Manufacturing Engineering, RMIT University is also gratefully acknowledged.

7. REFERENCES

[1] Hucho, W. H., 1998, Aerodynamics of Road Vehicles, 4th edition, Society of Automotive Engineers (SAE), ISBN 0-7680-0029-7, Warrendale, USA.

[2] Cooper, K. R., 2004, Pickup Truck Aerodynamics-Keep Your Tailgate Up, SAE Paper No. 2004-01-1146, SAE World Congress, and also in SP-1874 (Vehicle Aerodynamics 2004), ISBN 0-7680-1410-7, Detroit, USA.

[3] Saunders, J. W., Watkins, S., Hoffmann, P. H. and Buckley, F. T., 1986, Comparison of On-Road and Wind Tunnel Tests for Tractor-Trailer Aerodynamic Devices and Fuel Savings Predictions, SAE Paper No. 850286, Detroit, USA

[4] Watkins, S. and Hoffmann, P. H., 1985, Truck Aerodynamics: A Code of Good Aerodynamic Practices for Drivers, Owners and Operators", prepared for the Department of Resources and Energy, the Federal Government of Australia in conjunction with the Royal Melbourne Institute of Technology (RMIT University).

[5] Watkins, S., Kumar, H. B. and Saunders, J. W., 1991, Truck Fuel Saving Aerodynamic Devices-Investigation of Cabin Loads", SAE Paper No. 912528, 1991, PP 657-663, Detroit, USA.

[6] Watkins, S., Saunders, J. W. and Hoffmann, P. H., 1993, Comparison of Road and Wind Tunnel Drag Reductions for Commercial Vehicles, Journal of Wind Engineering and Industrial Aerodynamics, Vol. 49: 411-420.

[7] Alam, F. and Watkins, S., 2004, Aerodynamics of Trucks and Drag Reducing Devices, Journal of Mechanical Engineering, Vol. 8 (1), Khulna University of Engineering and Technology, Khulna, Bangladesh.

[8] Watkins, S. and Alam, F., 2012, Future vehicle thermal cooling and aerodynamic drag savings: where will they come from? Proceedings of 2012 International Conference on Advanced Vehicle Technologies and Integration, China Machine Press, pp. 775-782, 17-20 July, Changchun, China

[9] Alam, F. and Watkins, S., 2013, Implication of vehicle aerodynamics on fuel savings and the environment, Proceedings of the International Conference on Mechanical, Industrial and Materials Engineering (ICMIME2013), 1-3 November, RUET, Rajshahi, Bangladesh, pp 071-082, ISBN: 978-984-33-7879-8.

[10] Paul, A.R., Jain, A. and Alam, F., 2019, Drag reduction of a passenger car using flow control techniques, International Journal of Automotive Technology, Vol. 20 (2): 397-410.

[11] Chowdhury, H., Moria, H., Ali, A., Khan, I., Alam, F. and Watkins, S., 2013, A Study on Aerodynamic Drag of a Semi-trailer Truck, Procedia Engineering, Vol. 56: 201-205, Elsevier

[12] Chowdhury, H., Juwono, R., Islam, R., Zaid, M., Loganathan, B. and Alam, F., 2019, An experimental study on of the effect of various deflectors used for light trucks in Indian subcontinent, Energy Procedia, Vol. 160: 34-39, Elsevier.

[13] Chowdhury, H., Islam, R., Hussein, M., Zaid, M., Loganathan, B. and Alam, F., 2019, Design of an energy efficient car by biomimicry of a boxfish, Energy Procedia, Vol. 160: 40-44, Elsevier.

[14] National Road Traffic Accident Report prepared by Bangladesh Road Transport Authority Road Safety Cell, 2001, Ministry of Communication, Government of the people's Republic of Bangladesh, Dhaka

[15] Annual Report by Bangladesh Road Transport Authority (BRTA), 2018, Ministry of Road Transport and Bridges, pp. 1-77, Dhaka, http://www.brta.gov.bd/

[16] Raghuram, G., 2015, An Overview of the Trucking Sector in India: Significance and Structure, Indian Institute of Management (IIM) Ahmedabad, W.P. No. 2015-12-02, p.1-16.
[17] Road Accidents in India, 2016, Transport Research wing, Ministry of Road Transport & Highways, Government of India, New Delhi, pp.1-106.
[18] Australian Design Rules (ADRs), Department (Ministry) of Infrastructures, Regional Development and Cities, Canberra, https://infrastructure.gov.au/vehicles/design/
[19] Reports by Bangladesh Passengers Welfare Association (BPWA), 2017 & 2018, 2 Bangabandhu Avenue (6th Floor), Dhaka 1000, Bangladesh. https://www.facebook.com/Passenger-Welfare-Association-of-Bangladesh-1524530641169648/
[20] Accident Research Institute (ARI), Bangladesh University of Engineering and Technology, Dhaka, http://ari.buet.ac.bd/
[21] Daily Dawn, 2019, 13 February, https://www.dawn.com/news/1463472
[22] The Nation, 2018, 10 July, https://nation.com.pk/10-Jul-2018/over-15000-people-die-in-pakistan-annually-due-to-traffic-accidents
[23] Tata Motors India, https://tatatrucks.tatamotors.com/tata-trucks/trucks/tata-lpt-3718/overview.aspx
[24] Motor Bazee, http://www.motorbazee.com/new-ashok-leyland+truck
[25] Eicher Motors (India) Ltd, https://www.eichertrucksandbuses.com/
[26] Snyder, R.H., 1997, Tire Rolling Losses and Fuel Economy, SAE Special Publication, SAE Paper No.74, Detroit, USA.
[27] BharatBenz, https://www.bharatbenz.com/
[28] Singh, S.K., 2016, Road Traffic Accidents in India: Issues and Challenges, Transportation Research Procedia, Vol. 25: 4708–4719

NUMERICAL MODELLING OF FIRE AND EVACUATION IN TYPICAL SHOPPING MALL FIRE IN BANGLADESH

M. A. Hoque[1], T. I. Joy[1], R. H. Mridha[1], M. R. Mia[1], S. K. Saha[1], A. A. Khan[1], F. M. Haque[1], M. A. R. Sarkar[2], M. A. Rahman[3]

[1] Student, Department of Mechanical Engineering, Bangladesh University of Engineering and Technology

[2] Professor, Department of Mechanical Engineering, Bangladesh University of Engineering and Technology

[3] Associate Professor, Department of Mechanical Engineering, Bangladesh University of Engineering and Technology

Corresponding E-mail: ashiqurrahman@me.buet.ac.bd

Abstract: *The findings of a numerical study for a range of fire spread and evacuation scenarios for fire incident in a popular shopping mall in the capital Dhaka, Bangladesh where a severe fire incident took place in 2017, are reported. The effect of fire incident for the actual geometry of the two-storied market at the peak shopping time is analyzed and is further extended for a four-storied market maintaining the same geometrical aspects and fuel loads. The fire modelling is carried out using a computational fluid dynamics (CFD) tool PyroSim, and the evacuation scenario during the fire incidents is analyzed using Pathfinder. The fire growth and occupant evacuation are reported for two different fuels, polyester and polyurethane, each representing the major fuel item in the two most common types of stores, clothing store and furniture store, respectively, in the market under consideration. It is found that for the cases considered in the present study, the occupants can safely evacuate the mall without being trapped which is due to the open egress routes and sufficient number of exits in this market. Pre-evacuation time, resulting from to the absence of regular fire drills of the occupants, is also found to increase the required evacuation time significantly. This study can be helpful in assessing the fire risks for markets and shopping complexes in Bangladesh, especially considering the recent fire tragedies.*

Keywords*: Fire safety, Fire modelling, Evacuation, Shopping mall, PyroSim, Pathfinder, FDS.*

1. INTRODUCTION

Among different commercial occupancies, fire in a market represents a challenging and significant fire hazard due to the presence of large amount of volatile and flammable materials which include polyester, nylon, plastic, particle board and many more, high density of occupants and so on. Despite being a major concern, the scope for experimental validation for fire and smoke propagation is constrained because of the destructive nature of the fire and the risks associated with it. Proper understanding of the nature of the fuel, combustion chemistry and computer simulations are necessary in order to analyze fire and safety performances because various changes in the environment works as a stimulant for evoking fire. Performance-based fire growth and smoke propagation models can be helpful in the evaluation of fire safety performance of a building when coupled with evacuation models based on occupant reactions.

Computational tools based on Large Eddy Simulation (LES) and Computational Fluid Dynamics (CDF) have been used to model fire growth and smoke spread with sufficient accuracy. PyroSim is a CFD tool based on fire dynamics simulator (FDS), working on the basis of optimization of speed and thermally driven flow.

Different fire and smoke propagation scenarios for a variety of occupancies, such as fire in a cinema hall and multistoried dormitory building have been modeled using PyroSim by different researchers [1, 2]. Fire risk assessment for underground mining was reported by Adjiski *et al.* [3], where a systematic analysis was performed to assess the riskiest places for fire occurrence by simulating fire and smoke propagation using computer modelling software. The smoke propagation indicated the possible passages for safe evacuation of the employees based on the fire characteristics such as heat release rate, burning rate of material, generated toxic gases, smoke *etc.*

Considerable studies have been carried out on the effect of different parameters such as type of fire, occupant characteristics, building geometry etc. on the evacuation behavior in different types of occupancies. The relationship between the number of evacuees and emergency exit for safe evacuation has been perused [4]. Adequate facilities to prevent smoke intrusion into the layers of space should be ensured for better protection of the personnel [5]. Since carbon monoxide (CO) is a major toxic product of the smoke which leads to more fatality than the actual fire itself, the concentration of CO and fire induced smoke spread was analysed both vertically and horizontally for an 88m long channel using FDS and LES [6].

Pathfinder is an evacuation modeling software which allows varying psychological aspect of human behavior during evacuation in order to determine the safest egress route for minimum damage and maximum safety. It has two models to simulate evacuation process which include Society of Fire Protection Engineers (SFPE) model and Steering model, while different evacuation characteristics vary between the two models. A highly germane study was reported by Wang *et al.* which involved the reconstruction of a fatal fire that occurred in an indoor shooting range in Korea in 2009 where 15 occupants were killed, and one survived among all the 16 occupants present [7]. In addition, one previous work could be found on the modeling of fire and smoke in a commercial

market that included use of both PyroSim and Pathfinder in order to determine the egress time along with the safe evacuation condition of the market [8].

This study addresses the fire risk of a shopping mall in Bangladesh and examines the building performance in terms of safe evacuation of a market during peak time when occupant density remains high. The building was modelled to resemble the original geometry of the market where the devastating fire incident took place including features such as size and location of the shops, hallway, stairway, number of shops etc. Fire and smoke propagation as well as subsequent evacuation of the occupants have been modeled for the same building having the same geometrical dimensions and number of shops. The characterization of the fuel properties and fire dynamics have been carried out according to the Society of Fire Protection Engineers (SFPE) handbook. Fire scenarios have been considered for the original two-storied building and for a hypothetical four-storied building of the same geometrical structure and fuel load (polyester as fuel) in order to compare and analyze the effects of fire and smoke on occupant evacuation for the same building with more stories and more occupants. Further, the four-storied hypothetical building has been subjected to a different fuel load (polyurethane) to determine the effects of varying fuel of different heat release rates on the occupant evacuation and egress route. All these have been considered at the peak time of the day.

2. BUILDING GEOMETRY AND SIMULATION METHODOLOGY

A two-storied commercial market building of Dhaka North City Corporation Dhaka was considered to analyze the fire hazard and consequences. Polyester and polyurethane, these two fuels were considered for simulating fire in two types of stores i.e. clothing and furniture stores, respectively, available in this market. Since many shopping malls in the country with similar traditional geometric and architectural features comprise of three or more stories, simulations for a four-storied building structure was carried out in addition to the original market building design of two-stories, The third and fourth stories had the same shop, hallway, and exit arrangment as that of the 1st floor of the original structure. This was done to examine what the fire-smoke propagation and evacuation scenario would be if the building had more stories. Furthermore, fire and evacuation scenario for a second fuel polyurethane, commonly used as a material for upholstery and available in the furniture stores, is considered in order to determine the effects of different fuel sources on the safety performance of such market buildings. Simultaneously, an evacuation model was developed observing the human behavior for these cases. The corresponding heat release rate and reaction for polyurethane and polyester were determined from the SFPE handbook. The t-square fire growth model was used to determine the ramp-up time for the fuels.

The shopping mall in the present study was designed in Pyrosim (Fig. 1(a)), according to the original approved drawing of the shopping mall under consideration.

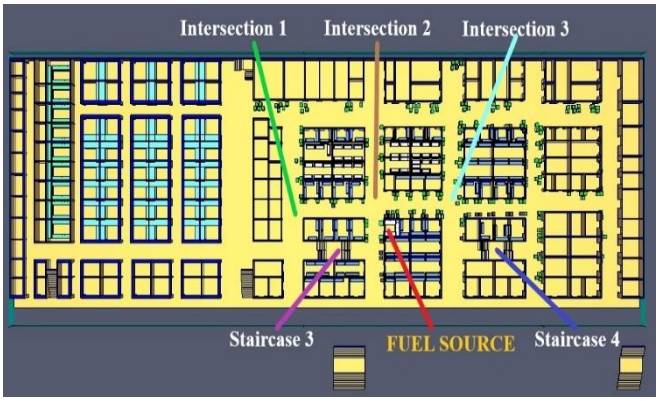

(a)

(b)

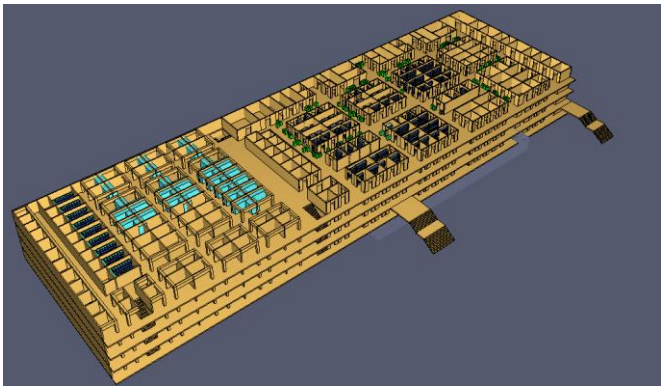

(c)

Figure 1: (a) 3D view of the 2-storied commercial market where the fire incident took place, (b) Layout of the fire floor where the fire initiated, fuel source and the location of corridors and staircases, (c) 3D view of the 4-storied commercial market having the same geometric and architectural characteristics as the actual shopping mall considered in this study.

The two storied building had total number of 291 shops (188 at ground floor and 103 at 1st floor) and each floor had an area of 5658.75 m^2. The fire is considered to originate at the peak time of the day on the ground floor, in a clothing store located near Intersection-2 as labelled in Fig. 1(a). Some of the salient

characteristics of the market, material properties and fire incident are provided in Table 1.

Table 1: Salient geometric features of the two-storied market building and fuel parameters that were considered for simulating the fire-incident in the present study

Features	Quantity
Total Number of Floors	2
Area of Each Floor	5658.75 m^2 (60910.28 ft^2)
Number of Shops in Each Floor	188(Ground Floor), 103(2^{nd} Floor)
Location of Fire Source	A clothing store near the Intersection-2, closest staircase being Staircase-3
Fuel Source	Polyurethane, Polyester
Peak Heat Release Rate of Polyester	685 KW/m^2
Peak Heat Release Rate of Polyurethane	Pyrosim In-Built Library

For evacuation modeling, the occupant density was decided keeping in mind of the rush hour of the market as determined from field survey. The total number of occupant was considered 1310 for the two-storied structure and 2250 for the four-storied structure. The total occupants were categorized into some groups. The allocation is given in Table 2.

Different types of shops in each floor of the market determined the population distribution which was validated in the base of age group distribution data from the work of Khan and Chowdhury [9]. The occupant density in the 1st floor was 0.222 person/m^2 and in the ground 0.242 person/m^2 which is within the range of the literature value found from [10]. The occupants on the second and third floor were considered to be a 75% of the occupants on the first floor. The occupant allocation is tabulated in Table 2 based on practical data and assumptions.

In case of fire emergency, gender, physical characteristics like height, shoulder width, walking speed plays a significant role on evacuating. The occupant allocation is done based on the age distribution data collected from literature [11]. It should be noted that for the simulation of the evacuation process, it was decided that 20% of the shopkeepers would assist other occupants during evacuation in case of a fire in a shopping complex.

Anthropometry data reported from [12] have been used in this study, added in the Table 3, for height, breadth and standard deviations for both male and female occupants. The data for adult male and female is kept same as of the data for workers of RMG building for an earlier work [13].

One of the prime factors of evacuation, the varying walking speed depending on age, gender and physical fitness as demonstrated through the experimental data of [14] was selected as it resembles the demographic of the market occupants closely. The speed of the children and elderly people is obviously different from adult male and female, child speed was taken from [15] and elderly people from SFPE handbook [16] added in Table 4. Instead of following a specific evacuation route, the occupants were free to choose any route for safe egress as they are considered not to be familiar with the location of nearest exits in the building.

Another key factor is the 'pre-evacuation time', which indicates the additional time taken due to the lack of immediate reaction to fire. The pre-evacuation time for shopkeepers is likely to be higher than other customers for prioritizing reduction of material damage along with the fact that it has been assumed that about 20% of the shopkeepers will assist other occupants for evacuation.

Table 2: Allocation of the occupants for the market building

Category	Ground floor (Number of occupants)	First floor (Number of occupants)	Second Floor (Number of occupants)	Third Floor (Number of occupants)
Male	52	-	-	-
Male who will assist other	70	87	66	66
Female	84	159	120	120
Female who needs assistance	75	125	94	94
Female who will assist other	5	5	4	4
Shopkeepers	371	201	151	151
Elderly male	10	10	8	8
Elderly Female	5	5	4	4
Child	12	34	26	26
Total Occupants on each floor	684	626	470	470
Total number of occupants in the building	2250			

Table 3: Detail of the body dimension considered for Bangladeshi male and female as per the data reported in [12]

Gender	Dimension	Minimum (in)	Maximum (in)	Mean (in)	Standard Variation
Male	Shoulder Breadth	13.685	19.307	16.496	0.937
	Height	59.82	72.22	66.02	2.067
Female	Shoulder Breadth	14.382	20.1	16.925	1.5
	Height	57.3	64.7	60.32	1.2

Table 4: Detail of walking speed in emergency considered for Bangladeshi young male and female, child and elderly [15, 16]

Category	Distribution Type	Speed (m/s)			
		Min	Max	Mean	Standard Deviation
Adult Male	Normal	2.36	3.4	2.944	0.41
Adult Female	Normal	2.336	2.52	2.432	0.09
Elderly Male	Constant	1.05			
Elderly Female	Constant	1.04			
Child	Uniform	1.14	2.23	--	--

Therefore, considering these factors, the pre-evacuation time ranges from 23 seconds to 152 seconds with an average of 74 seconds. This data is derived from the SFPE handbook for business occupancy. For other occupants who will not be assisted, pre-evacuation time is set with a mean of 40s within a range of 20s to 50s. For the occupants who require assistance, pre-evacuation time will depend on the occupants who will assist them.

In order to ensure safe evacuation of the occupants, certain parameters such as smoke concentration, visibility, temperature, CO concentration have to be under the tenability limit. These parameters were determined by installing corresponding measuring devices set on each floor near staircases and intersections. From the SFPE handbook the critical value of CO concentration was taken as 3000 ppm, threshold temperature was taken as 60°C and for untrained evacuees, the visibility limit was taken as 13 meters. These are the limiting values of these parameters. Any route where the fire and smoke properties go beyond these limiting values, becomes untenable for evacuation as per the standard of SFPE.

3. RESULT AND DISCUSSION

There are significant limitations while working with fire dynamics in general and especially in fire scene construction since experimental manifestation of the actual fire cannot be performed due to the risks associated with it. Since science-based fire scenario is not practiced in Bangladesh, the official report on the fire incident does not include many scientific details. Therefore, the knowledge of scientific principle and fire dynamics, detailed analysis of possible fire scenarios have been used in this study to carry out the analysis of the fire incident for the worst case fire scenario and the occupant safety issues coupled with it.

A devastating fire incident took place in a shopping mall in Dhaka, Bangladesh, in 2017 and caused collapse of one side of the market building. According to the official report by the Bangladesh Fire Service and Civil Defense (BFSCD) on this fire incident, the fire accident originated from an electric spark in a general store situated on the south-east corner of the ground floor (Fig. 1(b)) inside the market. According to the eyewitness, fire was initiated approximately in between 01:30 a.m. to 01:40 a.m. and smoke came out from the east corner of the market at around 01:56 a.m. of 3rd January. The fire service was informed of the fire at 02:30 a.m. and one side of the market was collapsed in 2-3 minutes after the fire service department reached the place. The generation of excess heat due to the fire incident and infrastructural error were reported as the main reasons for the collapsing of the one side of the market. Fortunately since this devastating incident occurred late at night, no lives were lost despite the collateral damage endured. The amount of loss due to this fire incident was approximately 300 crore BDT. The general store in question housed combustibles such as plastics, paper and particleboards to generate such a tragedy.

The present study was undertaken by being motivated to examine the consequence of such a fire during the peak shopping time when a large number of shoppers are present. A number of different scenarios were considered with a variation in the fuel, location of fire origin, number of floors of the shopping mall, and number of occupants in the building [Table 5].

Table 5: Various Fire Scenario Considered

Scenario Designation	Characteristics
A	Polyester fuel source, burning surface area of 958.75 ft^2, two-storied original design of the market, peak time of the day
B	Polyester fuel source, burning surface area of 958.75 ft^2, four-storied similar design of the market, peak time of the day
C	Polyurethane fuel source, four-storied similar design of the market, peak time of the day

Scenario A: Fire and Smoke Propagation for the Peak Time of a Day for the Two-Storied Market (Fuel: Polyester):

The first scenario considered for analyzing the fire growth and smoke propagation was for the two-storied original market building with polyester as a fuel source. The source of the fire was a clothing store located on the ground floor of the market. Polyester was selected as a fuel source since there was a large number of clothing stores in the market. The total burning surface area of the polyester was 958.75 ft^2 having a peak heat release rate of 685 KW/m^2. The amount and distribution of the fuel within the fire source-store were taken following the typical pattern commonly practiced in such stores in Bangladesh. Different devices were placed on the fire floor as well as the upper floor of the building to measure temperature, visibility, CO concentration, CO_2 concentration. The devices were placed at 4 different heights of 0.45 m, 0.9 m, 1.45 m, 1.55 m. These heights were taken because 0.45 m, 1.45 m, 1.55 m are the crawling height, female eye height and male eye height respectively. Distances between the devices were maintained to be 5m in the corridors. A number of devices were also set on the base and landing of each staircase. Intersections 1, 2 and 3 were selected between different corridors. These intersections and the nearest staircases from the fire location were taken into consideration for analyzing the temperature, visibility, and CO concentration.

Fig. 2 shows the propagation of smoke at different points of time as the fire grew and spread. It is evident from the figure that the fire-smoke completely spreads through the intersections and corridors by 600 seconds.

Temporal variation of different tenability parameters at different locations for this particular fire scenario have been displayed in Fig. 3. It can be seen that the staircase-3 was the most affected in this case as this staircase was the nearest from the fire source. The maximum temperature was found at staircase 3 (63°C) while the temperature in other staircases and intersections remained below the tenability limit as these staircases were at a certain distance from the fire source. The visibility dropped under the tenability limit (13 meter for untrained occupants) for intersection-1 and staircase-3 at 250s and intersection-2 after 300s (Fig. 3(b)). As the simulation was performed considering the peak shopping hour of the day, all the shops inside the market was open. So the corridors at a distance from the fire source were not that much affected. The CO concentration curves show that all the staircases and intersection remain under the tenability limit of 3000 ppm up to 400 seconds.

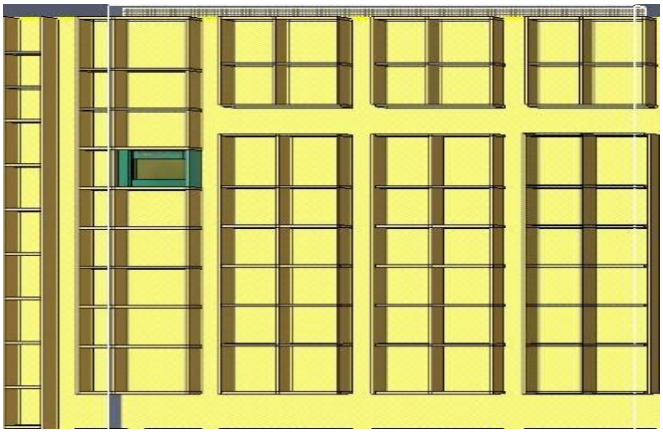

t=120s

t=300s

t=600s

Figure 2: The spread of fire and smoke throughout the market after the initiation of fire for scenario A

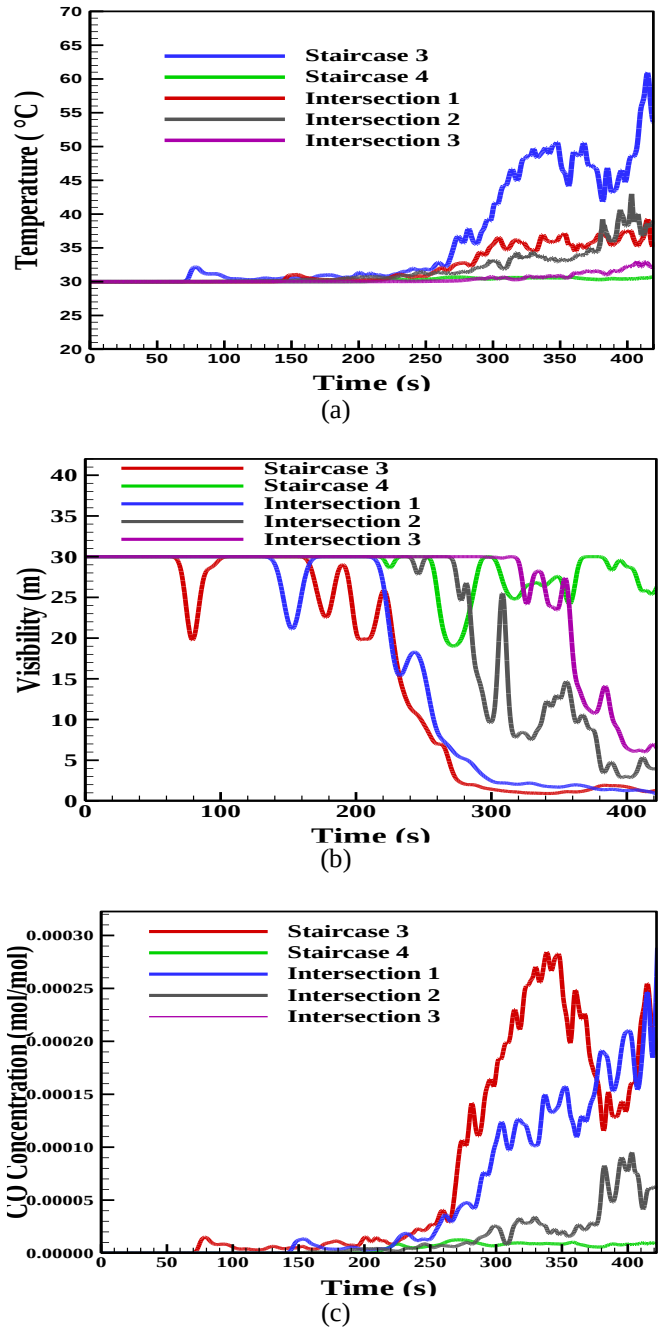

Figure 3: The variation of (a) temperature (b) visibility (c) CO concentration with time for different staircases and Intersections between the corridors on the fire floor for fuel load of Polyester.

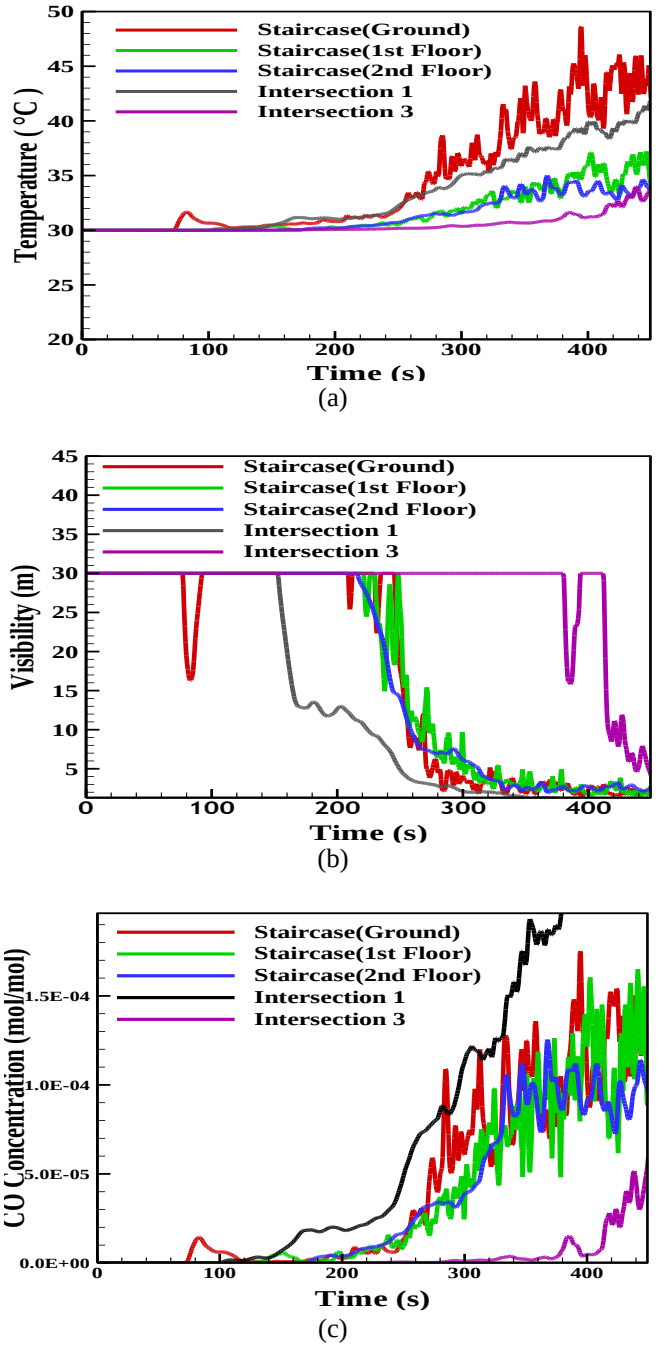

Figure 4: The variation of (a) temperature (b) visibility (c) CO concentration with time for different staircases and intersections between the corridors for fire scenario B.

Scenario B: Fire and Smoke Propagation for the Peak Time of a Day for a Four-Storied Market (Fuel: Polyester):

Being motivated by the devastating fire incident that took place in the two storied shopping mall in Dhaka, as discussed above, further analysis was conducted for a four storied market maintaining the same geometrical aspects.

Since many such typical shopping malls in the city comprise of four or more floors which possess a more significant risk in terms of the determination of the safety egress routes and safe evacuation time for the occupants of the market, the effects of fire and smoke propagation for a multi-storied complex were brought under consideration. Therefore, a building of the same geometry as the market where the fire incident occurred, comprising of four-stories instead of two as the original structure, was subjected to simulation to analyze the effects

(Fig. 1(c)). For reasons mentioned before, polyester having a burning surface area of 958.75 ft^2 and a peak heat release rate of 685 KW/m^2 was taken as the fuel source during peak time of the day. The devices on the upper floors were set at similar positions as those in the ground floor. The source of the fire was selected to be the same clothing store located on the ground floor.

It can be seen from Fig. 4 that in this case, the maximum temperature (48°C) was found in the ground level staircase since it was near the fire source. But all the staircases and intersections remain under the tenability limit up to 450 seconds. In case of visibility, while all the staircases of ground, 1st floor and 2nd floor went under tenability limit within 5 minutes, intersection-1 loses tenability after 150 seconds. Only intersection-3 remains under tenability limit up to 370 seconds. The CO concentration was found maximum at the intersection-1 but remained under 3000 ppm.

Scenario C: Fire and Smoke Propagation for the Peak Time of a Day for a Four-Storied Market (Fuel: Polyurethane):

For this scenario, fire and smoke propagation was considered for the same four-storied market as before during peak time, but instead of taking polyester as a fuel source, polyurethane was considered as the main fuel source to resemble fire in a furniture store of the market.

The staircases and the intersections were observed to be almost unaffected in this scenario as auto ignition temperature of polyurethane is very high. Since the simulation time was up to seven minutes due to computational limitations, the fire was not seen to propagate to the other furniture of the shop.

However, Intersection 2 was found to be under the tenability limit in case of visibility after 150 seconds (Fig. 5). CO concentration remained significantly below the tenable limit to cause any serious fatality.

For the same fuel load of polyester, it was observed that temperature exceeds the tenability limit after 400 seconds for the two storied building while remaining tenable for a four-storied building. Since maximum occupants are untrained in fire drills, staircase-3 becomes untenable rapidly due to its position of being the closest exit route from the fire source. The visibility limit drops below the tenability limit within 150 seconds for a fuel source of polyurethane as well. CO concentration remains within limit for all the three cases.

Analysis of Occupant Evacuation

Depending on the fire scenarios and pre-evacuation time and exit route, five distinct cases for evacuation of the occupants have been brought under consideration for polyester as the fuel source:

Case 1: Evacuation from Original Two-Storied Building Considering Pre-Evacuation Time

From the Pathfinder simulation, the evacuation time required by each occupant are obtained and plotted in Fig. 6. The minimum evacuation time by an occupant is about 25 seconds whereas maximum time requirement is 230 seconds (Fig. 6). This evacuation time represents the expected behavior of untrained people during an emergency such as fire. This case represents the behavior of people in cases when they are not trained with regular fire drills.

During a fire, the shopkeepers, instead of evacuating as fast as possible, try to protect their properties or try to suppress the fire which is supposed to be done by firefighters. This causes higher pre-movement time which ultimately increase total evacuation time.

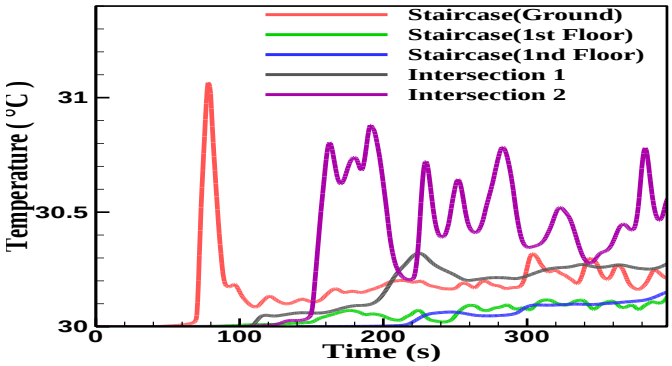

(a)

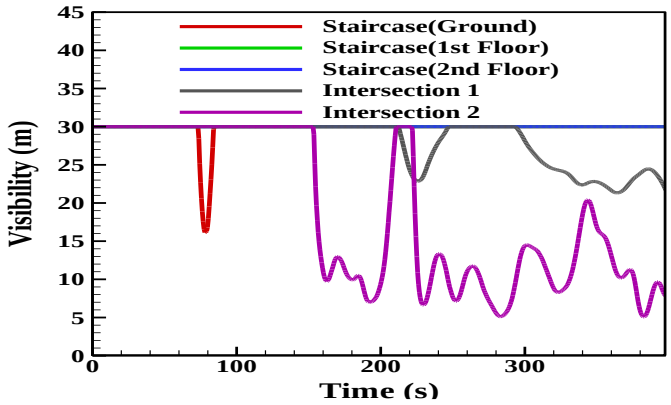

(b)

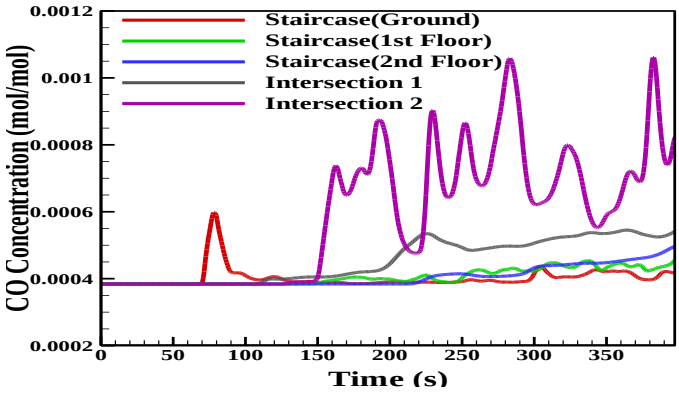

(c)

Figure 5: The variation of (a) temperature (b) visibility (c) CO concentration with time for different staircases and intersections between the corridors for fire scenario C.

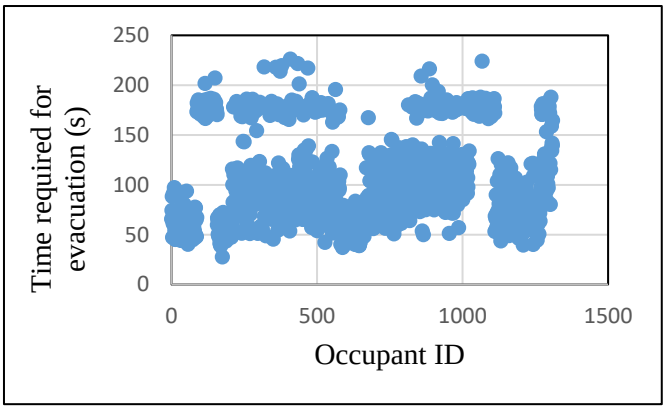

Figure 6: The evacuation time required by each occupant from the market for original geometry and considering pre-evacuation time.

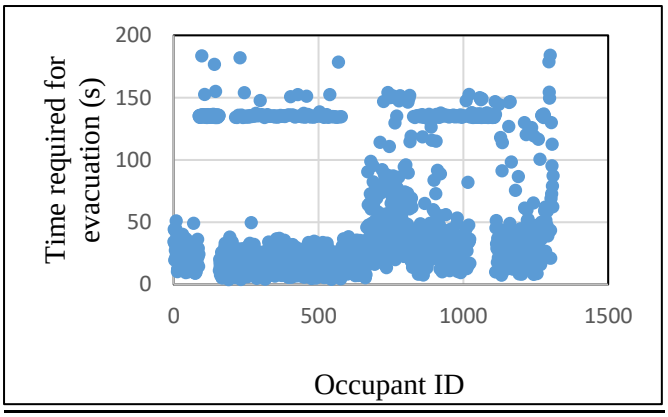

Figure 7: The evacuation time required by each occupant from the market for original geometry without considering pre evacuation time.

Secondly, the market is always crowded with occupants of different age group starting from child to elderly people. In the simulations, it was considered that during the event of fire, the children and elderly people would need assisted evacuation, *i.e.*, they would need to be accompanied by other adult male or female occupants. This scenario causes a reduction of moving speed for both assisted and assisting occupant and results in higher evacuation time.

Thirdly, the results from fire dynamics shows that the smoke spreads quickly through the staircase-3 which is the closest to the fire source on the ground floor. The staircase is found to be untenable to use due to low visibility at around 200 seconds of fire ignition. The occupants had to change their route to avoid smoky staircases and travel a longer distance causing the evacuation time to be higher.

Case 2: Evacuation from Original Two-Storied Building without Considering Pre-Evacuation Time

For Case 2, where pre-evacuation time is not considered and the occupants promptly begins the evacuation procedure, both the minimum and maximum evacuation time are reduced considerably (Fig. 7). The minimum and maximum evacuation time required in this case is 5 seconds and 180 seconds, respectively. Therefore, the maximum time required for the last occupant to evacuate is lower if pre evacuation time is not considered.

For further analysis, the original design was extended up to four floors while keeping the design of the 2rd and 3rd floors similar to the 1st floor with minor modifications. Keeping the occupant density within reasonable range, the population was reduced by a factor of 0.75 compared to the population of the 1st floor, for the possible reluctance of the shoppers to go to the upper floors. The total number of occupants was determined to be 2250 for the four-storied shopping complex by maintaining these criteria. The anthropometric data and speed of the occupants were kept same as before.

Case 3: Evacuation from Four-Storied Building Considering Pre-Evacuation Time:

For a geometry of identical structure as the two-storied shopping complex, simulations were carried out for the four storied building considering pre-evacuation time. Here the maximum time requirement is increased to 443 seconds as pre-evacuation time was considered (Fig. 8).

Case 4: Evacuation from Four-Storied Building without Considering Pre-Evacuation Time

For the same geometry and structure of the four-storied shopping complex, the time requirement for the evacuation process ranges from 5 seconds to a maximum value of 411 seconds for the last person to evacuate (Fig. 9). The maximum evacuation time reduces about 32 seconds if pre-evacuation time is not considered.

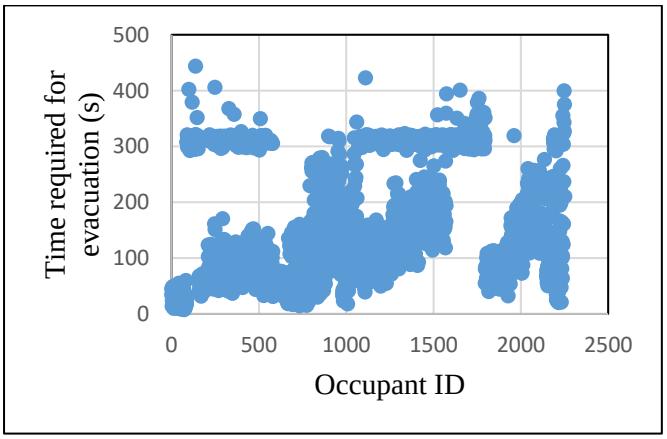

Figure 8: The evacuation time required by each occupant from the market for four-storied market geometry and considering pre evacuation time.

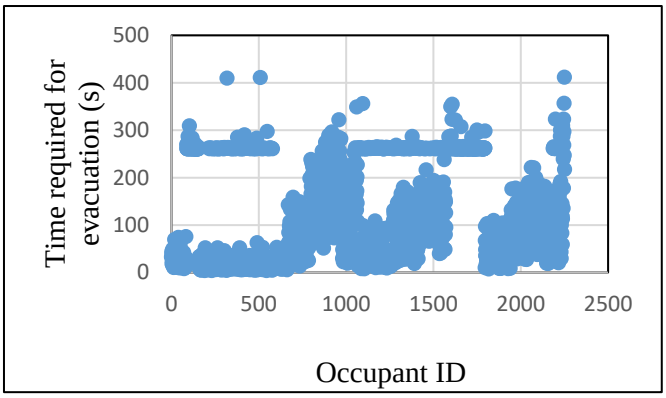

Figure 9: The evacuation time required by each occupant from the market for four-storied market geometry without considering pre evacuation time.

Case 5: Evacuation from Four-Storied Building with Occupants Choosing a Different Path

In order to gain a more realistic insight of the possible evacuation scenario and to analyze the safety performance of the four-storied shopping complex, another evacuation case was examined where the smoke affected exit was intentionally closed in order to divert the occupants towards a different evacuation route. By manually blocking the fire zone in terms of evacuation, the occupants were simulated to follow a different escape route. In this case, the maximum time requirement for evacuation was found to be 460 seconds as shown in Fig. 10.

Visibility reduction acts as the limiting parameter for tenability. The reduction of visibility due the smoke generated from the burning of fuel used in this study was considerably slow. On top of that since the floor height is about 3 meters, it takes a significant amount of time for the smoke to reach the eye level since smoke goes upwards. So the effect of smoke does not significantly affect the evacuation process. But the common tendency of untrained people who are not exposed to regular fire drills, is to avoid the path of smoke or fire despite the path being well under the tenability limit, provided they have an alternate route for evacuation.

The maximum time required for the last person to evacuate safely without being trapped for the abovementioned five evacuation cases have been summarized in Table 6. It is evident that even though no occupants were trapped in these cases, pre-evacuation time adds to the risk of fatality due to the additional time that is required. Further, evacuating occupants from a two-storied building is undoubtedly easier and requires about 48% of the time that is required to evacuate occupants from a four-storied building. Both fuels under consideration in this study show similar results for evacuation within tolerance.

Table 6: Maximum time required for the last person to evacuate for the 5 evacuation cases considered

Evacuation Scenario Designation	Required Maximum Evacuation Time (s)	No. of Occupants Trapped
Case 1	230	0
Case 2	180	0
Case 3	443	0
Case 4	411	0
Case 5	460	0

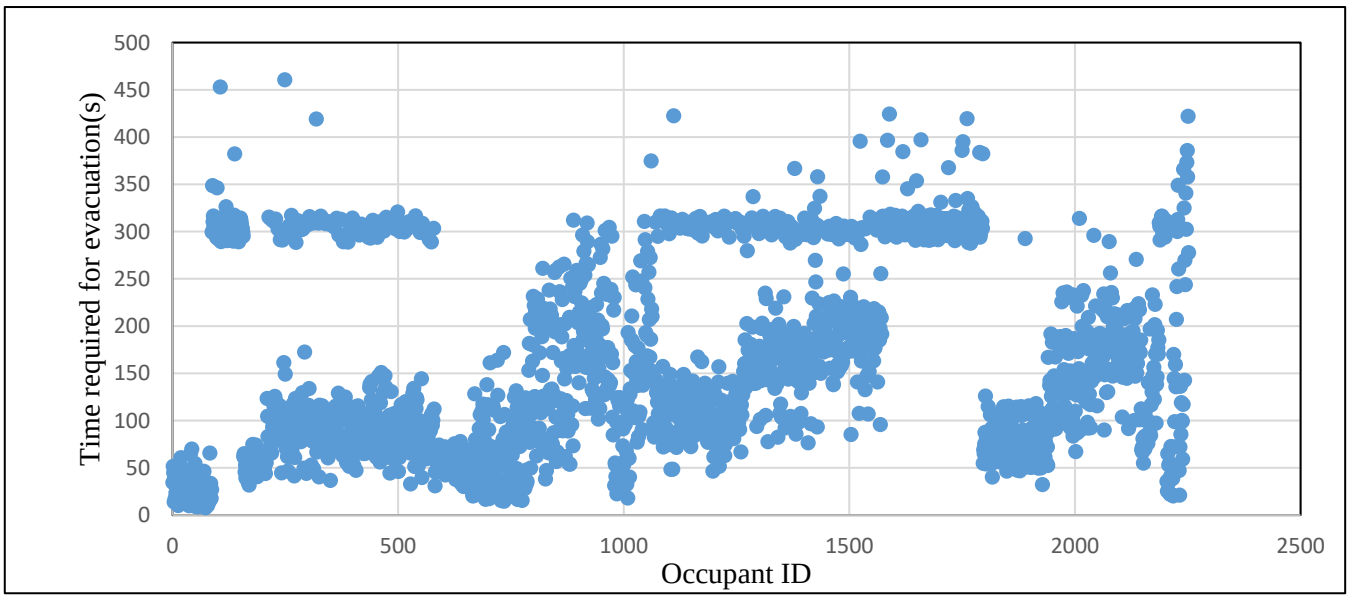

Figure 10: The evacuation time required by each occupant from the market for four-storied market geometry where occupants choose a different exit route

4. CONCLUSION:

A CFD modelling study for fire growth and smoke propagation, coupled with evacuation modelling of the occupants, was conducted to evaluate the fire safety performance of a multistoried complex in Dhaka, Bangladesh. The effect of building structure, fuel sources and egress routes on the evacuation process and occupant safety was analyzed. For a fuel load similar to an actual clothing store, it was observed that the nearest staircases and corridors were mostly affected by high temperature, visibility reduction and high carbon monoxide concentration. For both the two-storied and four-storied market simulation, the temperature and CO concentrations remain under tenability limit up to a certain time but the visibility drops rapidly and since the occupants are untrained, visibility becomes the main determining factor for safe evacuation. For the fire scenarios considered in this study it was found that no occupant was trapped within the building. This could be attributed to the building having open egress routes and sufficient number of exits. But it is evident that evacuation time increases by 48% for the four-storied complex compared to the two-storied original market building of the same structure. Pre-evacuation time also increases the maximum time required for evacuation by approximately 21%. However, if the goods of the shops are distributed in a uniform pattern and obstructions by different objects both inside and outside each shop were minimized, the required safety egress time, the time for the last individual to exit the building could have been slightly lower. Considering the large number of shopping mall fires and subsequent life and property damage that take place in Bangladesh every year, the present study presents a useful and necessary step by performing the fire safety assessment of multi-storied shopping complex for a range of fire scenarios.

5. ACKNOWLEDGEMENT

The authors would also like to express their sincerest gratitude to Bangladesh Fire Service and Civil Defense (BFSCD) authority for their support.

6. REFERENCES

[1] Glasa, J., Valasek, L., Weisenpacher, P. and Halada, L., 2012, “Use of PyroSim for simulation of cinema fire”, Int. J. on Recent Trends in Engineering and Technology, 7(2), pp.51-56.

[2] Long, X., Zhang, X. and Lou, B., 2017, “Numerical simulation of dormitory building fire and personnel escape based on Pyrosim and Pathfinder”, Journal of the Chinese Institute of Engineers, 40(3), pp.257-266.

[3] Adjiski, V., Despodov, Z., Mirakovski, D., & Mijalkovski, S., 2015, "Fire Risk Assessment and Computer Simulation of Fire Scenario in Underground Mines", Studies in Engineering and Technology, 2(1), 54.

[4] Chen, H.N. and Mao, Z.L., 2018, “Study on the Failure Probability of Occupant Evacuation with the Method of Monte Carlo Sampling”, Procedia engineering, 211, pp.55-62

[5] Li, M.X., Zhu, S.B., Wang, J.H. and Zhou, Z., 2018, “Research on Fire Safety Evacuation in a University Library in Nanjing”, Procedia engineering, 211, pp.372-378.

[6] L. H. Hu, N. K. Fong, L. Z. Yang, W. K. Chow, Y. Z. Li, and R. Huo, 2007, “Modeling fire-induced smoke spread and carbon monoxide transportation in a long channel: Fire Dynamics Simulator comparisons with measured data,” J. Hazard. Mater, vol. 140, no. 1–2, pp. 293–298.

[7] Wang, Z., Jia, F., Galea, E.R. and Choi, J.H., 2017, “A forensic analysis of a fatal fire in an indoor shooting range using coupled fire and evacuation modelling tools”, Fire Safety Journal, 91, pp.892-900.

[8] Dong, S., Li, M. and Lin, Y., 2014, “Study on Numerical Simulation of Fire and Evacuation for a Supermarket”, Applied Mechanics & Materials.

[9] Khan, M.M.H. and Choudhury, A., 2016, “Impacts Of Shopping Mall Attributes And Environment On Customer Buying Attitudes: An Analysis On Dhaka City”.

[10] Chen, J.J., Fang, Z., Sun, J.Y. and Wang, J.H., 2014, “Research of occupant density in the wholesale and retail market”, Procedia engineering, 71, pp.265-270.

[11] Khan, M. H., Choudhury, A., 2014, "Impacts of shopping mall attributes and environment on customer buying attitudes: an analysis on Dhaka city”, D.U. Journal of Marketing, 17, pp. 25-48.

[12] Khadem, M.M. and Islam, M.A., 2014, “Development of anthropometric data for Bangladeshi male population”, International Journal of Industrial Ergonomics, 44(3), pp.407-412.

[13] F. M. Haque, M. A. R. Khandoker, M. Wasi, R. M. Khan, S. A. Mahmud, and M. A. Rahman, 2018 “Computer Modelling Of Fire Safety Performance Of A Ready- Made Garments Building In Bangladesh,” *Proc., Safety in The Ready-made Garments (RMG) Sector of Bangladesh: An Assessment of The Existing Scenario, 30 April 2018, Dhaka, Bangladesh.*

[14] Wong, L.T. and Cheung, T.F., 2006, “Evaluating probable risk of evacuees in institutional buildings”, Safety science, 44(2), pp.169-181.

[15] Larusdottir, A.R. and Dederichs, A.S., 2012, “Evacuation of children: Movement on Stairs and on Horizontal plane”, Fire technology, 48(1), pp.43-53.

[16] Hurley, M.J., Gottuk, D.T., Hall Jr, J.R., Harada, K., Kuligowski, E.D., Puchovsky, M., Watts Jr, J.M. and Wieczorek, C.J., 2015, “SFPE handbook of fire protection engineering”, Springer.

IMPLEMENTATION OF RESPONSE SURFACE METHODOLOGY AND GENETIC ALGORITHM IN OPTIMIZATION OF PARAMETERS IN MACHINING HARDENED STEEL (HRC 65) USING CERAMIC TOOL

Md. Tanvir Ahmed[1], Niaz Quader[2], Mahmudur Rahman[3], AKM Nurul Amin[4]*

[1, 2, 3] Department of Mechanical and Production Engineering, Ahsanullah University of Science and Technology (AUST), Dhaka-1208, Bangladesh 1, 2, 3

[4] Department of Industrial and Production Engineering, Military Institute of Science & Technology (MIST), Mirpur Cantonment, Dhaka -1216, Bangladesh 4

*Corresponding E-mail: akmnurulamin1954@gmail.com

Abstract: *The present study focuses on turning of hardened alloy steel (HRC 65) using mixed uncoated ceramic inserts (Al_2O_3 + TiC) in dry condition. The main objective of the work was to achieve minimum surface roughness by optimizing the cutting parameters (cutting speed, feed rate and depth of cut) using different optimizing techniques. The design of experiment was conducted applying Response Surface Technique (RSM) using Design Expert software version 11. Central composite design (CCD) was chosen as the design option for developing appropriate regression models. The impact of each cutting parameter was obtained from statistical analysis of variance (ANOVA), which revealed that cutting speed followed by feed rate have dominating impact on surface roughness. Empirical model of surface roughness was developed in terms of the cutting parameters. This model was used for optimizing the machining parameter for minimizing attainable surface roughness using desirability function of RSM and Genetic Algorithm (GA). From the validation tests on both the models for actual versus predicted scenario, GA was found to be more accurate in predicting surface roughness compared to RSM.*

Keywords*: ceramic tool, hard turning, central composite design, genetic algorithm, response surface method*

1. INTRODUCTION

As a result of the increased hardness of the hardened steels (45-65) HRC, it has become a challenging to machine these materials at room temperature. Machining these steel at elevated temperatures is one of the approaches. However, in thermally assisted machining the process of heating and maintaining a uniform temperature distribution within the workpiece is difficult to control. Furthermore, the original microstructure of the job may be altered [1], thus adversely affecting job properties. Manufacturing costs would be also high due to the heating cost. In order to facilitate increasingly demand of hardened steel, machining these materials using ceramic tools could be a rational option. This is related to the fact that, ceramic tool capabilities have expanded in recent years, they are capable to withstanding extreme temperatures and stresses imposed on them during rough and finish cutting of hardened ferrous machining components. But the ceramic tends to premature tool failure due to thermal shock which creates serious detrimental effects on the quality of the machined part as well as on the efficiency and economics of the overall machining operation [1, 2]. So, in order to have a satisfactory performance from the ceramic tool, the machining parameters need to be optimized to achieve desired surface quality in dry machining condition.

Surface finish not only defines the dimensional accuracy of machined parts but it is also a reflection of the material properties of the machined parts, especially fatigue strength. Whereas surface finish describes the geometric features, surface integrity relates to properties such as fatigue life and corrosion resistance. These are strongly influenced by the type of surface being produced while manufacturing. The factors that influence surface integrity are: (a) temperatures produced during machining, (b) residual stresses generated on the surface, (c) metallurgical transformations and (d) plastic deformation such as tearing and cracking developed in the surface of the work material. Ceramic and diamond tools generally produce a better surface finish than other tools, largely because of their much lower tendency to form Build Up Edge (BUE) [3].

Ceramic tool provides good surface quality until the chipping occurs at the tool edge due rubbing of the chipped tool over the machined surface. Rubbing in machining also generates frictional heat and can induce surface residual stresses, which in turn, may cause surface damage such as tearing and cracking. When the cutting tool edge is still intact the surface profile of the workpiece is predominantly affected by the feed [4-8]. However, when the cutting edge has chipped the surface of the workpiece is not only affected by the tool nose and the feed but also by many other factors. After the tool chipping the peak-to-valley heights of the surface roughness profile changes irregularly and fluctuate significantly. This is because when the cutting tool has chipped its effects on the cutting force variation can cause severe vibration between the tool and the workpiece during machining [3, 8-9]. Ceramic tool provides high abrasion resistance and hot hardness [2, 7-8]. Chemically they are more stable than HSS and Carbides; as a result they don't adhere to metals during machining thus giving a satisfactory performance during machining of hardened steel.

PCBN is a great alternative for hard turning but a costly alternative. Whereas tools such as Carbide is not recommended for such hard turning but could be done so through the means of addition of high-pressure coolant jet or cryogenic process. [3, 10]

However, Ceramic tool lacks in toughness, therefore during machining might be subjected to premature tool failure via chipping or gross fracture. If the tool condition is not properly monitored, the whole production might inhibit low productivity and increased production lead time. In response to these problems, the current study investigates surface roughness of the hardened steel by optimizing the process parameter in machining hardened steel.

The present study focuses on investigating the influence of cutting parameters on surface roughness while machining hardened steel using ceramic tool and finding the optimum machining parameters for achieving minimum average surface roughness using RSM and GA.

2. EXPERIMENTAL CONDITION

The experiments were conducted on a hardened steel shaft of diameter 65 mm using mixed uncoated ceramic cutting tool with varying cutting speed, feed rate and depth of cut. The length of the cylindrical shaft was 310 mm with an average hardness of 65.12 throughout the workpiece. The chemical analysis in Table 1 reveals the dominant chemical composition in Weight percentage.

Table 1: Chemical analysis of hardened steel shaft

C	**Si**	**Mn**	**P**	**S**
Wt.%	Wt.%	Wt.%	Wt.%	Wt.%
0.17	0.17	0.87	0.011	0.013

To perform the straight turning operation over the hardened steel shaft a CC 650 graded mixed ceramic tool (Al_2O_3 + TiC) of ISO insert geometry code of TNGN 16 04 16T01020 from Sandvik Coromant was used. Experimental conditions are briefly provided in Table 2.

Table 2: Experimental Conditions

Machine tool	Engine Lathe machine, Model: CS6266B
Work material	Hardened alloy steel
Material hardness	65 HRC
Cutting tool	TNGN 16 04 16T01020; Sandvik Coromant
Insert coating	Uncoated mixed ceramic tool (Al_2O_3 + TiC)
Tool holder	CTJNR 2020K16; ZCC.CT
Profilometer	Phase II SRG- 4500
Process parameters	
Cutting speed	98, 129.5, 161 m/min
Feed rate	0.1, 0.12, 0.14 mm/rev
Depth of cut	0.2, 0.3, 0.4 mm
Environment	Dry

Due to the lower thermal conductivity of Ceramic material no coolant or lubricant was used during machining. The limit of the DOE was taken on the basis of parameter upon which machining of the ceramic tool is suggested according to the manufacturing guideline and the dimension of the work material.

Surface roughness is one of the characteristics of surface finish which is a very important measure of machined surface quality. So, the quantification of surface roughness is necessary because the magnitude of the irregularities in the surface has a huge impact on the quality and performance of the surface. The surface roughness of the work material was quantified through the vertical deviations of a real surface from its ideal form which is measured as RMS value of microscopic peak and valleys. High surface roughness value is mostly undesirable but it's difficult to control because of the cost. Surface roughness was measured by the Contact type method using Phase II SRG- 4500 Profilometer for an accurate reading.

There are enormous amount of factors which could be considered as the machining parameters in turning operation. Nevertheless, depth of cut (d, mm), cutting speed (v, m/min) and feed rate (f, mm/rev) are considered the most significant input parameters. In this study, the experiment was designed using central composite design. After carrying the experiment Response Surface Methodology (RSM) was used to predict the empirical equation between the input variables (cutting speed, feed rate and depth of cut) and the output variable (surface roughness). RSM enables a stepwise investigation to predict the empirical equation. Due to its enormous ability to develop model and analysis of problems many researchers have used RSM in their research work 3,4. Design Expert software was used to perform RSM in this experiment. A two-level Full factorial central composite design was generated in the Response Surface Design which provides a model of 20 runs in which the design had 8 Cube point, 6 Center points and 6 axial points in the cube. The Design was created of 1 (Single) block consisting 6 Center Points in total but none of the center points were at Cube or at Axial position. Value of alpha was taken as Face Centered 1.682 (Default). The model is based on a single replication model. Experimental results of cutting Surface roughness along with the design space of 20 runs are shown in Table 3 Response surface design was analyzed with a 95 percent confidence level for all intervals.

The optimization tool in the MATLAB was used to select the optimized cutting condition using Genetic algorithm. Final equation generated from the design expert was taken as the function for the genetic algorithm.

The solution space was designed using the double vector population type with a population size of a 100. Creation function was taken as constraint dependent. A rank form of fitness scaling was implemented where the selection of each generation's population was based on roulette. A heuristic crossover function with a ratio of 1.2 (default) was taken. MATLAB limit for the genetic algorithm search space was considered from the Lower limit of [98, 0.1, 0.2] and Upper limit of [161, 0.14, 0.4]. Results from Genetic Algorithm was compared with those predicted by of Response Surface Methodology to determine the suitable optimization method considering surface roughness.

Table 3: Experimental results of Surface roughness

Run	A (m/min)	B (mm/rev)	C (mm)	Surface Roughness (μm)
1	161	0.14	0.4	0.487
2	129.5	0.12	0.3	0.57
3	129.5	0.12	0.3	0.623
4	129.5	0.12	0.4	0.4525
5	98	0.1	0.2	0.51
6	129.5	0.14	0.3	0.6985
7	129.5	0.12	0.3	0.558
8	129.5	0.12	0.2	0.4915
9	98	0.14	0.2	0.597
10	161	0.12	0.3	0.428
11	98	0.1	0.4	0.497
12	98	0.14	0.4	0.575
13	98	0.12	0.3	0.77
14	129.5	0.12	0.3	0.641
15	129.5	0.12	0.3	0.546
16	161	0.14	0.2	0.434
17	161	0.1	0.4	0.301
18	129.5	0.12	0.3	0.565
19	129.5	0.1	0.3	0.4105
20	161	0.1	0.2	0.31

3. EXPERIMENTAL RESULTS

Response surface methodology (RSM) is a great mathematical and statistical technique using which useful modelling and analysis of problems could be resolved through the response of several influential variables. RSM attempts to analyse the influence of the independent variables on specific or multiple dependent variables (response). The intention of developing mathematical models relating the machining responses and their factors is to facilitate the optimization of the machining process. The mathematical model for the machining response as function of Y is expressed as follows:

$$Y = \psi (v, d, f) + \varepsilon$$

Where, v, d, f are respectively cutting speed, depth of cut and feed rate and ε is the error which is normally distributed about the observed machining response Y.
Let,

$$\psi (v, d, f) = \eta$$

Where the surface represented using 'η' symbolizes response surface. Second order polynomial Model (Quadratic model) is used in this experiment in order to predict the response, surface roughness.

$$Y=\beta_0 + \sum_{j=1}^{k} \beta_j X_j + \sum_{i<j}^{k} \beta_{ij} x_i x_j + \sum_{j=1}^{k} \beta_{jj} x_j^2 + \varepsilon$$

Where, Y is proposed expected response on higher-order polynomial and $\beta's$ are process variables such as cutting speed, depth of cut and feed rate respectively, and are regression coefficients can be calculated by linear multiple regression analysis.
The experimental data were analysed through Design-Expert software considering CCD. The results of the analysis of variance (ANOVA) are shown in Table 4.

Table 4: Surface roughness analysis

Source	Sum of Squares	DF	Mean Square	F Value	p-value
Model	0.2288	9	0.0254	7.65	0.0019
A-Cutting Speed	0.0978	1	0.0978	29.44	0.0003
B-Feed Rate	0.0582	1	0.0582	17.52	0.0019
C-Depth of Cut	0.0001	1	0.0001	0.0271	0.8726
AB	0.0026	1	0.0026	0.7909	0.3947
AC	0.0008	1	0.0008	0.2348	0.6384
BC	0.0004	1	0.0004	0.1057	0.7518
A^2	0.0008	1	0.0008	0.2495	0.6282
B^2	0.0020	1	0.0020	0.6094	0.4531
C^2	0.0331	1	0.0331	9.95	0.0103
Residual	0.0332	10	0.0033		
Lack of Fit	0.0258	5	0.0052	3.46	0.0996
Pure Error	0.0074	5	0.0015		
Cor Total	0.2620	19			
Std. Dev.	0.0576			R^2	0.8732
Mean	0.5232			Adjusted R^2	0.7590
C.V. %	11.02			Predicted R^2	0.1623
				Adeq Precision	10.5311

Results of analysis of variance (ANOVA) reveal that the model to be significant as its F value is 7.65. It may be noted that the model terms with P values greater than 0.1000 are not significant and any value yielding a P value greater than 0.0500 were exterminated in the iteration to develop a better

model. In addition, it can also be seen from Table 4 that cutting speed (A), feed rate (B), the quadratic value of depth of cut (C2) all have a significant effect on the Surface Roughness; while the depth of cut (C), the quadratic value of cutting speed (A2), the quadratic value of feed rate (C2), and none of the interaction shows significant effect in the model. From Table 4 It is clear that the "Pred. R-Squared" of 0.1623 is in reasonable agreement with the "Adj. R-Squared" of 0.7590. "Adeq. Precision" quantifies the signal to noise ratio. A ratio greater than 4 is desirable and the resulted ratio is 10.5311 indicates the signal to be satisfactory. This model can be used to navigate the design space. The "Lack of Fit F-value" of 3.46 implies that it is not significant relative to the pure error. There is a probability of 9.96% that "Lack of Fit F-value" could occur due to noise. Non-significant lack of fit is good because it is desired that the model should fit the data. The equation of Surface roughness in terms of the coded factor was derived as:

Surface roughness = + 0.5830 - 0.0989 * A + 0.0763 * B - 0.0030 * C + 0.0181 * AB + 0.0099 * AC + 0.0066 * BC + 0.0174 * A ^ 2 - 0.0271 * B ^ 2 - 0.196 * C ^ 2 …. (1)

While the equation of the Surface Roughness in terms of actual factors is given by the following equation:

Surface roughness = -0.44 - 0.0121 * Cutting velocity + 15.4 * Feed rate + 5.74 depth of cut + 0.000017 Cutting velocity * Cutting velocity - 67.8 Feed rate * Feed rate - 10.96 depth of cut * depth of cut + 0.0288 Cutting velocity * Feed rate + 0.00313 Cutting velocity * depth of cut + 3.3 feed rate * depth of cut …. (2)

The initial model may be improved by removing insignificant model terms from it. For this purpose, the backward elimination procedure was employed to automatically reduce the terms that are not significant. The resulting ANOVA table for the reduced quadratic model is shown in Table 5.

Table 5: Surface roughness analysis after reduced quadratic model

Source	**Sum of Squares**	**DF**	**Mean Square**	**F Value**	**p-value**
Model	0.2228	4	0.0557	21.33	< 0.0001
A-Cutting Speed	0.0978	1	0.0978	37.45	< 0.0001
B-Feed Rate	0.0582	1	0.0582	22.29	0.0003
C-Depth of Cut	0.0001	1	0.0001	0.0345	0.8552
C^2	0.0667	1	0.0667	25.54	0.0001
Residual	0.0392	15	0.0026		
Lack of Fit	0.0317	10	0.0032	2.13	0.2089
Pure Error	0.0074	5	0.0015		
Cor Total	0.2620	19			
Std. Dev.	0.0511			R^2	0.8505
Mean	0.5232			Adjusted R^2	0.8106
C.V. %	9.77			Predicted R^2	0.7320
Std. Dev.				Adeq Precision	15.3641

The Model F-value of 21.33 implies that the model is significant. In addition, the parameters A, B, C and C2 are also found to be significant (as their P value were < 0.0500 (except the C which is a continuous factor linear model interaction)). Factor C has been included in the model in order to maintain the hierarchy. The "Lack of Fit F-value" of 2.13 implies the Lack of Fit is not significant relative to the pure error. There is a 20.8% chance that a "Lack of Fit F-value" this large could occur due to noise. The final equation of Surface Roughness in terms of the coded factor is given:

Surface roughness = + 0.5810 - 0.0989 * a + 0.0763 *b - 0.0030 * c - 0.1155 * c ^ 2 ….. (3)

While the final equation of Surface Roughness in terms of the actual factor is given below:

Surface roughness = - 0.500711 - 0.003140 * Cutting Speed + 3.81500 * Feed Rate + 6.90000 * depth of cut - 11.55000 * depth of cut ^ 2 …. (4)

Table 6: RSM optimized result

Cutting Speed	Feed rate	Depth of Cut	Surface Roughness	Desirability
161	0.1	0.2	0.293	1
161	0.1	0.4	0.287	1

Experimental data relations obtained from DOE are provided in Fig. 1.

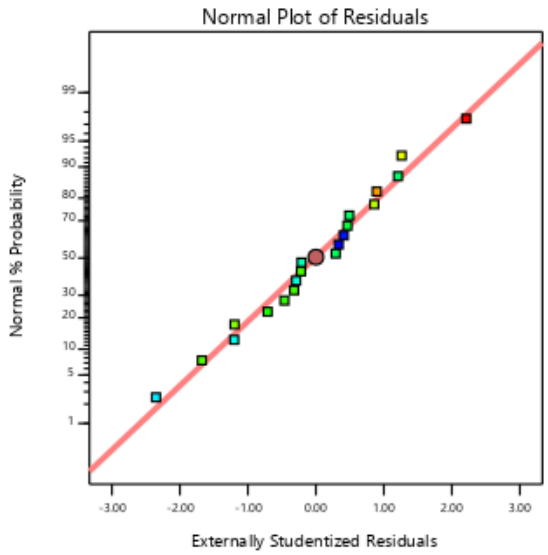

(a) Normal residual plot

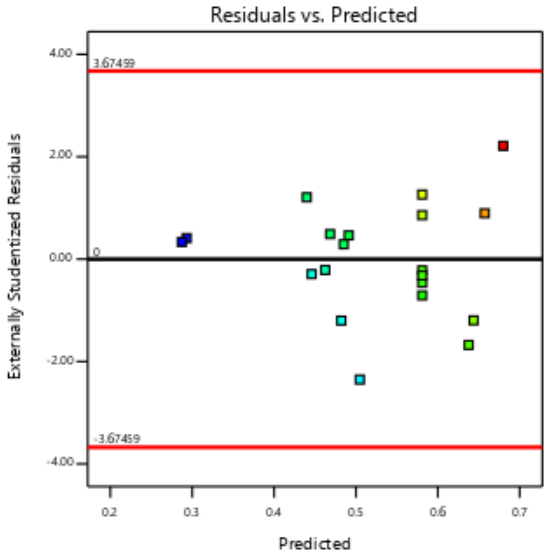

(b) Residual vs predicted

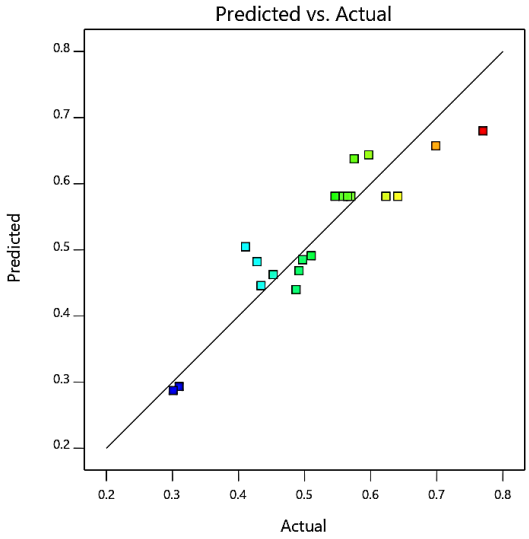

(c) Predicted vs actual

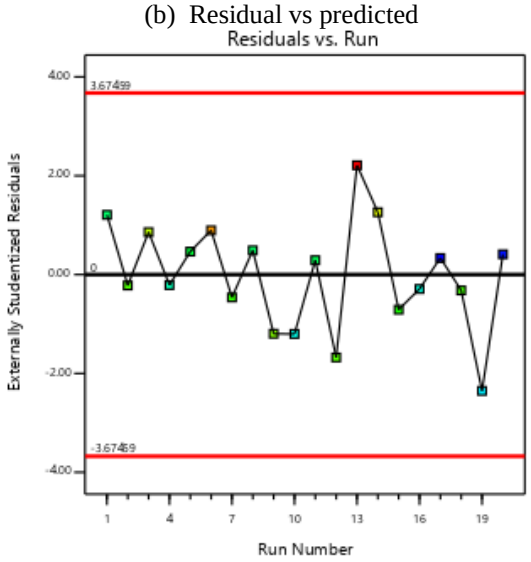

(d) Residuals vs run

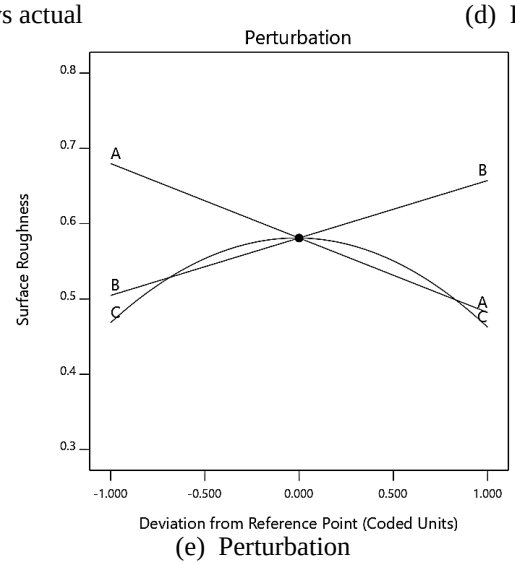

(e) Perturbation

Figure 1: (a) Normal residual plot, (b) residual vs predicted, (c) predicted vs actual, (d) residuals vs run and (e) perturbation of RSM of surface roughness in optimization

In the graph in Fig. 1 (a) represents normal plot of probability of the residuals for Surface Roughness. This is associated. It also illustrates that all values of Surface roughness are within limit. From Fig. 1(b) no pattern was depicted from residuals. The predicted values of Surface Roughness from Equation 4 are compared with the corresponding experimental values which are portrayed in Fig. 1 (c). The run was random without any sequence of pattern according to Fig. 1(d). A plot of perturbation was obtained from RSM comparing the effect of all machining parameters. The perturbation plot in Fig. 1 (e) which reveals the following outcome: (i) the Surface Roughness decreases substantially with an increase in the cutting speed (A), (ii) the Surface Roughness increases significantly with an reveals that the residuals that fall on a straight line are distributed normally with minimum amount of error increase in the feed rate (B) and (iii) surface roughness decreases parabolic nature for the depth of cut. Fig. 2 illustrates the main effects of the two major factors cutting speed (A) and feed rate (B) on Surface Roughness for constant of depth of cut at 0.3 mm. From this figure, it can be observed that higher cutting speed and lower feed rate results in lower Surface Roughness. The influence of the two factors cutting speed (A) and depth of cut (C) on Surface Roughness while keeping the feed rate constant level at 0.12 m/rev is depicted in Fig. 3. From this figure, it is observed that higher cutting speed and both in term of highest and lowest depth of cut results in lower Surface Roughness

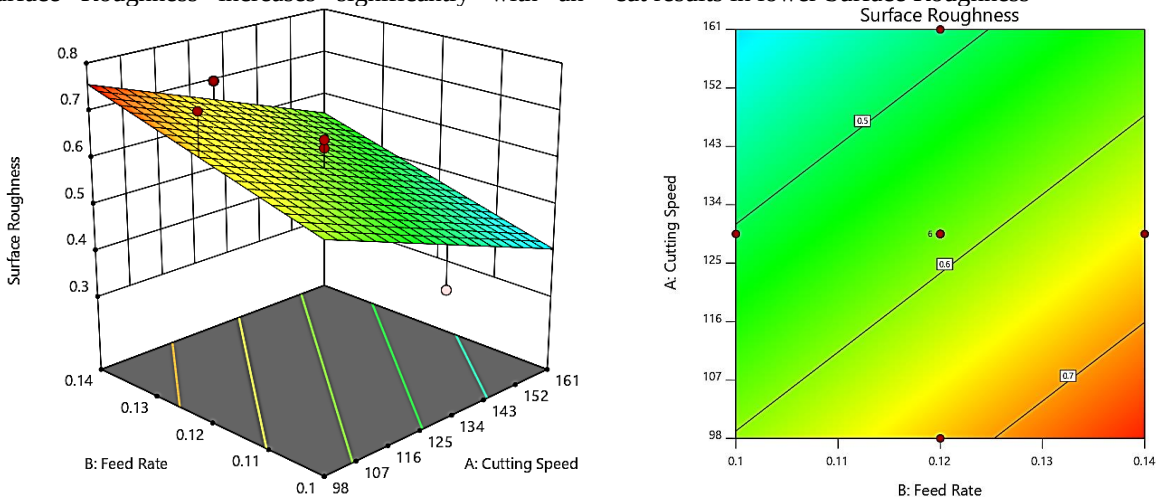

(a) Surface plot of cutting speed vs feed rate (b) Contour plot of cutting speed vs feed rate

Figure 2: (a) Surface plot of cutting speed vs feed rate and (b) Contour plot of cutting speed vs feed rate considering surface roughness

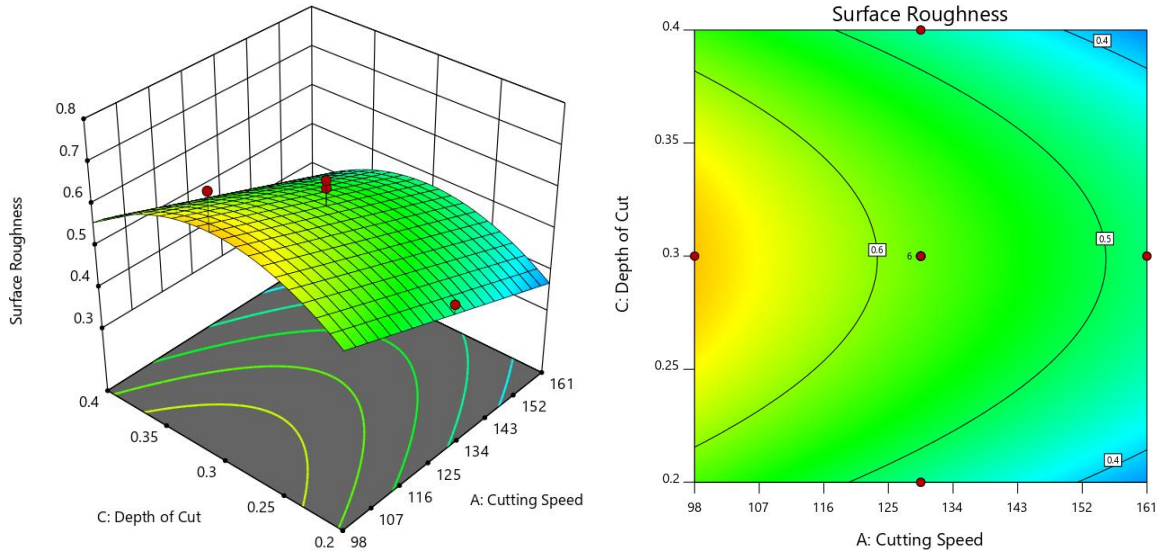

(a) Surface plot of cutting speed vs depth of cut (b) Contour plot of cutting speed vs depth of cut

Figure 3: (a) Surface plot of cutting speed vs depth of cut and (b) Contour plot of cutting speed vs depth of cut considering surface roughness

The genetic algorithm optimization method selected the fittest generation using the process of the natural selection process of evolution. The final function of surface roughness in Term of Actual Factor provided the global minimum of the function of Y for the genetic algorithm which represents the surface roughness. Where Y=GA(X) was taken as the function of the surface roughness. Y = - 0.500711 - (0.003140 * X (1)) + (3.815 * X (2)) + (6.90 * X (3)) - (11.55 * X (3) * X (3));

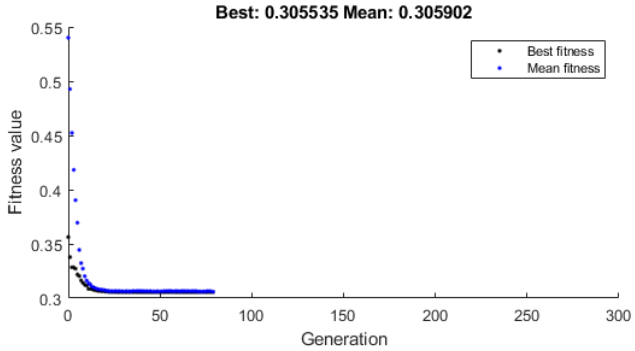

(a) Fitness value vs Generation

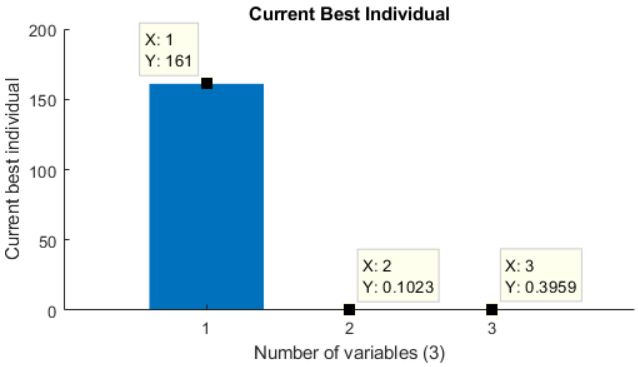

(b) Current best individual vs no. of variables

Figure 4: (a) Fitness value vs Generation, (b) Current best individual vs number of variables for average surface roughness 0.305535 µm

Fig. 4 represents the number of generation for which it achieved the global minimum of the fitness function. Where the achieved the best result of surface roughness value is 0.305535 µm. The optimized value of the process parameters was found for cutting velocity of 161 m/min, feed rate 0.1023 mm/rev and depth of cut of 0.3959 mm.

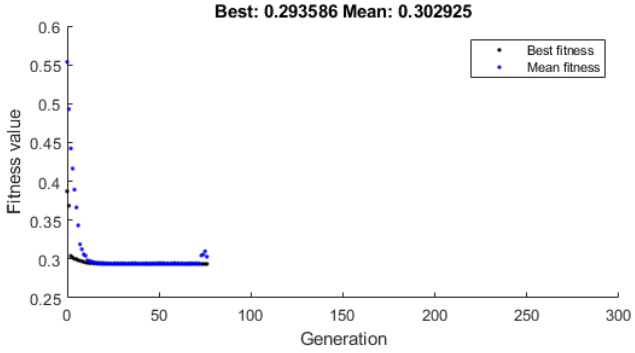

(a) Fitness value vs Generation

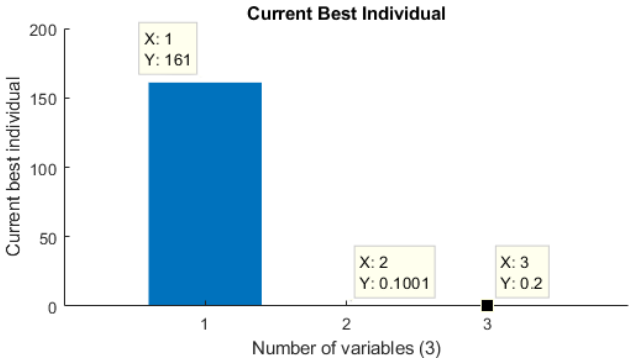

(b) Current best individual vs no. of variables

Figure 5: (a) Fitness value vs Generation, (b) Current best individual vs number of variables for average surface roughness 0.293586 µm

Fig. 5 represents the best result for surface roughness value, which is 0.2935 µm. The value of the process parameters in this case of optimized condition for cutting velocity of 161 m/min, feed rate 0.1001 mm/rev and depth of cut of 0.2 mm. The optimized values of the parameters with predicted surface roughness are provided in table 7.

Table 7: Optimized value of the parameters with predicted surface roughness

Cutting Speed (m/min)	Feed rate (mm/rev)	Depth of cut (mm)	Surface Roughness (µm)
161	0.1023	0.3959	0.305
161	0.1001	0.2	0.294

4. DISCUSSION ON EXPERIMENTAL RESULTS

Optimization models of RSM and GA both gave predicted Average Surface Roughness. The Surface Roughness was cross-checked with an actual average surface roughness obtained for the same parameter. Amount of percentage of error was calculated to identify which model was better at predicting from the mathematical model at: (i) Cutting Speed: 161 m/min, Feed rate: 0.1 mm/rev & Depth of cut: 0.4 mm and (ii) Cutting Speed: 161 m/min, Feed rate: 0.1 mm/rev & Depth of cut: 0.2 mm.

Table 8: Predicted vs Actual RA value for depth of cut 0.4 mm and 0.2 mm

Method	Depth of Cut (mm)	Predicted RA (µm)	Actual RA (µm)	Error %
RSM	0.4	0.287	0.301	4.878
GA		0.305	0.301	**1.639**
RSM	0.2	0.293	0.31	5.802
GA		0.294	0.31	**5.442**

So, the genetic algorithm was found to be more accurate in terms of predicting the surface roughness for the optimum conditions.

5. CONCLUSION

The objective of this optimization study was to find cutting parameters within the cutting speed range of 98 m/min to 161 m/min; the feed rate range 0.1 mm/rev to 0.14 mm/rev, and a depth of cut range from 0.2 mm to 0.4 mm and to determine the best suited optimization method for predicting surface roughness with least percentage of error. From the analysis, it was found that, the Ceramic inserts have performed well with an optimal operating condition at two global optimization points; (a) Cutting Speed: 161 m/min, Feed rate: 0.1 mm/rev & Depth of cut: 0.4 mm and (b) Cutting Speed: 161 m/min, Feed rate: 0.1 mm/rev & Depth of cut: 0.2 mm.

Based on the results of the study, following specific conclusions were drawn:

(i) For prediction of roughness parameters within the selected experimental domain, the quadratic models were taken as the objective function for optimization.

(ii) The effect of various factors on the model of the surface roughness shows that surface roughness decreases with the increase in cutting speed and increases with the increase of feed rate. The depth of cut has minimal effect as evident from ANOVA results. No interactions are significant, as per ANOVA results.

(iii) From the results of the optimization process it was depicted that Genetic Algorithm was able to predict the optimized cutting parameters more precisely than RSM.

(iv) The optimal surface roughness values 0.294μm and 0.305 μm were found in the following set of machining parameters: cutting speed within the range (98 m/min - 161.00 m/min), feed rate within the range (0.1 mm/rev - 0.14 mm/rev) and depth of cut within the range (0.20 mm - 0.4 mm) for combination of cutting speed 161.00 m/min, feed 0.1 mm/rev and depth of cut 0.20 mm with an prediction error of 5.16% and for combination of cutting speed 161.00 m/min, feed 0.1 mm/rev and depth of cut 0.40 mm with an prediction error of 1.639% with the help of GA. The desirability of this optimized condition was about 100% and the Rsq was 85.05% accurate.

6. ACKNOWLEDGEMENT

Authors would like to acknowledge BRTC; MME from BUET for providing the Material Hardness and Chemical Analysis test. The authors are indebted to AUST as the research was conducted in machine shop of AUST, Bangladesh.

7. REFERANCE

[1] Cui, X., Guo, J., and Zheng, J., 2016, "Optimization of Geometry Parameters for Ceramic Cutting Tools in intermittent Turning of Hardened Steel," J. Materials & Design, vol. 92, pp. 424–437.

[2] Godoy, V. A. A. De, and Diniz, A. E., 2011, "Turning of Interrupted and Continuous Hardened Steel Surfaces using Ceramic and CBN cutting Tools," J. Materials Processing Tech., vol. 211, pp. 1014–1025.

[3] Mir, M. J., and Wani, M. F., 2017, "Performance Evaluation of PCBN, Coated Carbide and Mixed Ceramic Inserts in Finish-turning of AISI D2 Steel," J. Tribologi, vol. 14, pp. 10–31.

[4] Rao, C. J., Rao, D. N., and Srihari, P., 2013, "Influence of Cutting Parameters on Cutting Force and Surface Finish in Turning Operation," *Proceedings of International Conference on design and manufacturing, ICONDM 2013*, vol. 64, pp. 1405–1415.

[5] Varma, K. R., and Kaladhar, M., 2015, "Multiple Performance Characteristics Optimization of Hard Turning Operations using Utility Based-Taguchi Approach," J. Mechanical Engineering, Vol. ME 45, No. 2, pp. 73–80.

[6] Bensouilah, H., Aouici, H., Meddour, I., Yallese, M. A., Mabrouki, T. and Girardin, F., 2016, "Performance of Coated and Uncoated Mixed Ceramic Tools in Hard Turning Process," J. Measurement, vol. 82, pp. 1–18.

[7] Bekir Yalçın, T., 2015, "Surface Roughness and Cutting Forces in Turning of Tool Steel with Mixed Ceramic and Cubic Boron Nitride Cutting Tools," Transactions-Canadian Society for Mechanical Engineering, Vol. 39, Pp. 323–336.

[8] Hessainia, Z., Belbah, A., Athmane, M., Mabrouki, T., and Rigal, J., 2013, "On the Prediction of Surface Roughness in the Hard Turning Based on Cutting Parameters and Tool Vibrations," J. Measurement, vol. 46, pp. 1671–1681.

[9] Aleksandrovich, R. V., and Siamak, G., 2014, "The Effect of Tool Construction and Cutting Parameters on Surface Roughness and Vibration in Turning of AISI 1045 Steel using Taguchi Method," J., Modern Mechanical Engineering vol. 2014, pp. 8–18.

[10] Mia, M., and Dhar, N. R., "Effect of High Pressure Coolant Jet on Cutting Temperature , Tool Wear and Surface Finish in Turning Hardened (HRC 48) steel," J. Mechanical Engineering, Vol. ME 45, No. 1, pp. 1–6.